TECHNISCHE UNIVERSITÄT MÜNCHEN
Fakultät für Chemie
Lehrstuhl für Bauchemie

Biomineralization: Nanocasting of Plant Cell Walls

Somruedee Kuhlmann

Vollständiger Abdruck der von der Fakultät für Chemie der Technischen Universität München zur Erlangung des akademischen Grades eines

Doktors der Naturwissenschaften (Dr. rer. nat.)

genehmigten Dissertation.

Vorsitzender:	Univ.-Prof. Dr. Klaus Köhler
Prüfer der Dissertation:	1. Univ.-Prof. Dr. Johann P. Plank
	2. Univ.-Prof. Dr. Cordt Zollfrank

Die Dissertation wurde am 17.01.2019 bei der Technischen Universität München eingereicht und durch die Fakultät für Chemie am 29.04.2019 angenommen.

Acknowledgement

The research work presented in this thesis was performed in the time period from April 2012 to September 2017 at the Chair for Construction Chemistry, Technische Universität München. Hereby, I would like to thank all those who have contributed to the success of my PhD project.

First, I would like to express my deep gratitude to my doctor father **Prof. Dr. Johann Plank** for providing this challenging and interesting research subject, his interest and contribution to the success of my PhD project. Looking back as I was in my master study in Thailand and had attended his lecture on nanomaterials. His project and teaching style fascinated me and I am always thankful that he had given me this opportunity to pursue my PhD at his chair in Germany.

My heartfelt thanks also go to my SPP 1420 project partners, especially **Prof. Dr. Cordt Zollfrank** and **Dr. Daniel Van Opdenbosch** for being such a great colleagues and co-authors on my publications. Their enthusiasm and support contributed much to the completion of this work.

Special thank go to **Dr. Tobias Kornprobst** for being my great supervisor, who picked me up at 6 AM at the airport on my first day, suggested and supported me at the beginning of this project, and always being a good friend.

I would like to thank **Dr. Oksana Storcheva** and **Dr. Ahmad Habbaba** for all their help and support.

I also would like to thank our nice secretary of the Chair **Jingnü Liu, Anke Kloiber** and **Tim Dannemann** for their help in all administrative and organizational tasks. **Dagmar Lettrich** and **Richard Beiderbeck**, I want to thank you very much for your competent assistance and support concerning the accomplishment of chemical analysis and experiments.

Dr. Elina Dubina, I profoundly thank you for your help and encouragement during the time at the chair, and especially in a Praktikum in your laboratory at MC-Bauchemie.

I also thank my colleagues **Dr. Geok Bee Serina Ng, Thomas Pavlitschek, Maike Müller, Dr. Julia Pickelmann, Dr. Markus Meier, Dr. Johanna de Reese, Michael Glanzer-Heinrich,**

Dr. Vipasri Kanchanason, Dr. Nan Zou, **Dr. Salami Taye**, **Dr. Constantin Tiemeyer**, **Dr. Alex Lange, Dr. Daniel Bülichen**, **Dr. Stefan Baueregger, Dr. Lei Lei, Timon Echt**, **Dr. Thomas Hurnaus**, **Manuel Ilg, Mouala Moumin, Markus Schönlein, Johannes Stecher, Stefanie Gruber, My Linh Vo, Teepakorn Napharatsamee, Dr. Teresa Piqué, Zhihui Zhang, Dr. Mei Zhang-Preße, Huiqun Li, Alexander Rinkenburger, Dr. Tsuyoshi Hirata, Bin Yang and Fan Yang** for all their help and the collegial atmosphere.

I also would like to thank my colleagues at Evonik Nutrition & Care GmbH, Essen and Evonik Performance Materials, Marl, for all your encouragement during the time that I had been writing this thesis.

Thousand thanks go to my family who always support me, especially during some difficult times in my PhD. I deeply thank my parents **Sukum Klaithong** and **Sompong Klaithong** for all their love that always supports me in all steps of my life. My heartfelt thanks also go to my husband **Henning Kuhlmann**, who is always besides me, encourages me, and always believes in me.

Finally, I profoundly thank my grandfather **Boonthai Jityoi** for all his love and encouragement. “You are the person, who wanted to see the most that I have finished this degree. I am really sorry that I could not finish this PhD before you passed away on 16th July 2016. But I know that you can see my success from over there.”

Somruedee, December 2018

List of Publications

The following scientific manuscripts were published as a result of this research project. The thesis includes the papers #1-2.

Peer reviewed SCI(E) journal papers:

1) **Preparation of $CaCO_3$ and CaO Replicas Retaining the Hierarchical Structure of Spruce Wood**

   Somruedee Klaithong, Daniel Van Opdenbosch, Cordt Zollfrank, and Johann Plank

   Zeitschrift für Naturforschung B 68b (2013) 533 – 538 / DOI: 10.5560/ZNB.2013-3062

2) **Preparation of Magnesium Oxide and Magnesium Silicate Replicas Retaining the Hierarchical Structure of Pine Wood**

   Somruedee Klaithong, Daniel Van Opdenbosch, Cordt Zollfrank, and Johann Plank

   Zeitschrift für Naturforschung B 72(5)b (2017) 341–349/ DOI 10.1515/znb-2016-0241

List of Abbreviations

ATR = Attenuated total reflection

BET = Brunauer-Emmett-Teller

C_2S = Dicalcium silicate, belite

C_3S = Tricalcium silicate, alite

CML = Compound middle lamella

C-S-H = Calcium silicate hydrate

DLS = Dynamic light scattering

EDX = Energy dispersive X-ray spectroscopy

IR = Infrared spectroscopy

MAS = Magic angle spin

$MeOMgOCO_2Me$ = Methoxy magnesium methyl carbonate

ML = Middle lamella

NMR = Nuclear magnetic resonance

P = Primary wall

PCS = Photon correlation spectroscopy

QLS = Quasi-elastic light scattering

S = Secondary wall

SAXS = Small-angle X-ray scattering

SEM = Scanning electron microscopy

TEM = Transmission electron microscope

TEOS = Tetraethoxysilane

TGA = Thermogravimetric analysis

TGA-MS = Thermogravimetric analysis equipped with mass spectroscopy

TMOS = Tetramethoxysilane

XRD = X-ray diffraction

Abstract

The characteristic structures of softwoods (spruce or pine wood) were replicated on various levels of hierarchy from the macroscopic to the submicron scale. These positive replicas were successfully obtained by infiltrating the wood template with an alkaline earth metal carbonate precursor and subsequent drying and calcination.

Firstly, a calcium di(methylcarbonate) ($Ca(OCOOCH_3)_2$) precursor solution was used to produce calcium carbonate ($CaCO_3$) and calcium oxide (CaO) replicas. After infiltrating the spruce wood templates with the precursor, their cellulose matrix and other organic compounds were removed by calcination at temperatures varying between 350 and 900 °C. The motivation to vary calcination temperature and calcination time was to study their effect on the type of $CaCO_3$ polymorph formed, on the $CaCO_3$ particle size, the quality of replication, and the mechanical stability of the replica. Calcination of the pre-treated wood sample at 350 °C over a period of 48 h with one infiltration step decomposes the wood template very slowly and yields the meta-stable $CaCO_3$ polymorph vaterite. Calcination at higher temperature provides replicas with the $CaCO_3$ polymorph calcite. A way to improve the mechanical stability of the replica is multiple infiltration steps. Mechanical stability of the replica is optimized when the specimen is infiltrated for 5 times and calcined at 900 °C. At this high temperature, $CaCO_3$ is transformed into a more robust CaO replica representing an almost monolithic wood replica with reasonable mechanical stability.

Secondly, for infiltration a methanolic methoxy magnesium methyl carbonate ($MeOMgOCO_2Me$) solution was used as a precursor which then hydrolyzed into $MgCO_3$ nanoparticles. Subsequent calcination at temperatures ranging from 500 to 1450 ºC yielded porous monolithic replicas on the levels of hierarchy from the macroscopic to the submicron scale. They were composed of annealed MgO nanoparticles. Calcination at 1450 ºC yields replicas with improved mechanical stability, but it leads to considerable shrinkage (Δ_{ax} = 56%). The combined treatment with Mg and Si precursors (infiltrating the pine template first with $MeOMgOCO_2Me$, followed by a second infiltration step with ethanolic tetraethyl orthosilicate (TEOS) solution and subsequent calcination at 1350 °C) results in a replica constituted of an

MgO framework overgrown with Mg_2SiO_4 (forsterite). This replica exhibits a compression strength of 31 ± 8 MPa.

In the third project, calcium silicate hydrate (C-S-H) phases were formed on the surface of silica replicas. This silica replica was synthesized by infiltrating a pine wood template with an ethanolic tetraethyl orthosilicate (TEOS) solution and subsequent calcination at 500 °C. Then the replica's surface became negatively charged by partial ionization of the surface Si-OH groups to SiO^- anionic sites when immersed into a basic solution. Subsequent immersion in $Ca(OH)_2$ or $CaCl_2$ solution for a long period of time (72 h) leads to the formation a thin layer of foil-like C-S-H on the silica replica. Extending the immersion time to 24 h and with 3 cycles of immersion (whereby each time the solution was replaced with a fresh solution in each cycle) leads to C-S-H of fibrillar morphology and a high Ca/Si ratio.

Table of Contents

1 Introduction

Porous materials are useful in many applications such as supporters for catalysts or drugs, building materials, *etc.* [1]. A hierarchically structured material offers even more special advantages such as higher chance to trap particles with different diameters *e.g.* in fibrous membranes for air filtration [2]. Another example is batteries such as lithium-ion types, in which the nanostructured morphology accelerates lithium ion intercalation/deintercalation and electron diffusion, and enlarges the electrode-electrolyte interphase area, while the micron-sized assemblies provide high volumetric density, easy processability, and electrode integrity [3].

It is impossible to synthesize hierarchical structures via the normal synthesises. The pores obtained by cross-linking of polymer chains, aggregation or agglomeration of small particles, or selective removal of elements of a solid (e.g. by etching or pyrolysis) usually exhibit an irregular pore structure [4]. Therefore, in many studies different templates such as wood or bones are used to introduce hierarchical porous structures which can be transformed into materials of controlled properties.

Wood is a highly porous material because it has to bring water and nutrient from the root to the top of the tree. The wood structure constitutes several levels of hierarchy. At the macroscopic level, soft wood such as spruce and pine wood consist of hollow parallel tube-like wood cells called tracheid fibers which exhibit a diameter in the range of 10 to 40 microns, as is shown in **Figure 1 (left)**. These fibers arrange parallel to each other and form a honeycomb structure. Inside the wood cell walls, cellulose fibrils are embedded in polyoses which again are embedded in a lignin matrix. The cellulose fibrils are partly crystalline and exhibit a diameter of around 2.5 nm. They spiral the lumen at the characteristic microfibril angle [5-7]. The pit-hole structure is characteristic for wood, as is shown in **Figure 1 (right)**. Retaining this structure is considered as the indicator of whether the replication of the wood structure has been successful.

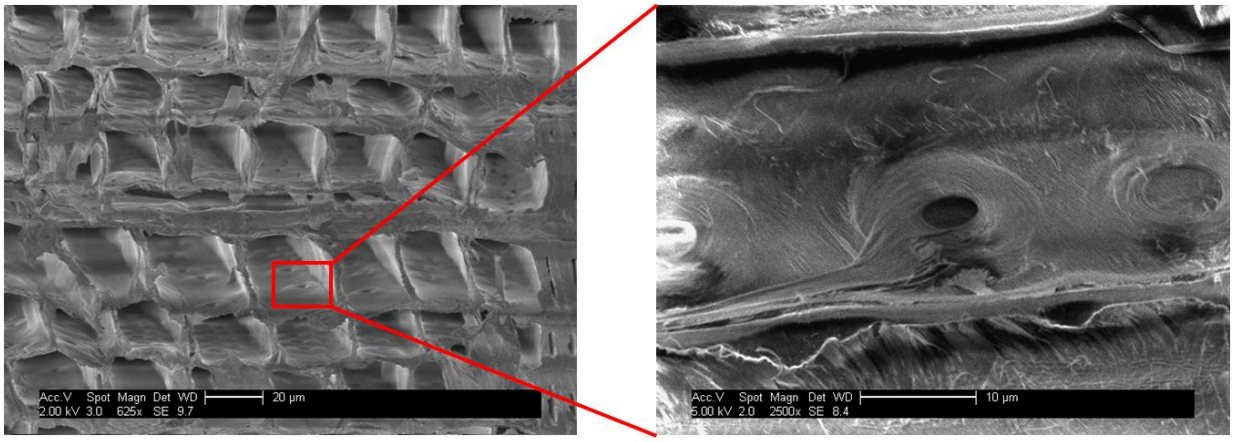

Figure 1. SEM images of delignified pine wood showing the honeycomb structure of hollow parallel tube-like wood cells (tracheids) (left) and pit-holes which are on the tracheid fibers (right).

The synthesis of hierarchically structured materials of alkaline earth compounds has inspired many previous works. The main method so far is the replication of cellulose fibrils using TEOS solution [8]. Replication by infiltrating the template with a precursor solution that can form covalent bonds within the template provides a particularly strong and stable replica, however it is a big challenge to obtain replicas exhibiting only via ionic or Van der Waals bonds between the primary particles.

In construction applications, oxides of alkaline earth metals are interesting because of their compatibility with the cement matrix.

In this doctoral study, firstly hierarchically structured $CaCO_3$ was synthesized by using calcium di(methylcarbonate) as calcium precursor and subsequent hydrolysis into a $CaCO_3$ sol. After infiltrating spruce wood templates with the precursor, their cellulose matrix was removed by calcination at temperatures varying between 350 and 900 °C. Calcination temperature and duration was varied in order to study their effect on the type of $CaCO_3$ polymorph formed, on the $CaCO_3$ particle size, the quality of replication, and the mechanical stability of the replica.

Due to the poor mechanical stability of $CaCO_3$ replicas which limits their use, *e.g.* for construction applications, the next part was devoted to fabricating hierarchically structured MgO replicas. It was hoped that the MgO replicas would exhibit higher mechanical stability. The

wood template was infiltrated with $MeOMgOCO_2Me$ as a magnesium precursor and subsequently hydrolysed into a $MgCO_3$ sol inside the wood cell walls. After infiltration, the cellulose matrix was removed by calcination at temperatures ranging from 500 to 1450 °C, yielding porous monoliths composed of MgO nanoparticles. The calcination temperature was varied in order to study its effect on the MgO particle size, the quality of replication and the mechanical stability of the replicas. Additionally, magnesium silicate replicas exhibiting high compressive strength were synthesized by infiltrating the MgO replica with an alkoxysilane precursor and subsequent calcination at 1350 °C. For this system, the temperature dependent formation of different magnesium silicates was studied.

Finally, calcium silicate hydrate replicas were synthesized in order to produce wood replicas with high mechanical stability. Calcium silicate hydrates are interesting materials because they are the main binding phases in hydrated Portland cement. Firstly, the silica replica was produced by infiltrating the wood template with TEOS solution and subsequent calcination at 500 °C. The surface Si-OH groups of the silica replica were partially ionized in basic solution to generate negatively charged of SiO^- anionic sites. Subsequently, immersion in a calcium hydroxide or calcium chloride solution under various conditions was performed in order to form calcium silicate hydrate on the surface of the silica replica.

2 Scope of the work

Within the framework of the DFG funded priority program SPP 1420 on materials produced by biomimetic processes the group of *Prof. Zollfrank* had successfully replicated the soft wood structure by using silica. It was our challenge to extend their general process to produce replicas by using alkaline earth metal-based precursors. More essentially, the main goals of this work were as follow:

- Use suitable earth alkali metal precursors such as methyl carbonate, calcium di(methylcarbonate) and methoxy magnesium methyl carbonate

- Replicate the wood structure precisely

- Study the infiltration mechanism of the organometallic precursor into the wood cell walls

- Investigate the morphology and structure of the replicas obtained from different preparation conditions such as different precursors, solid content of precursor solution, infiltration steps and calcination temperatures

- Improve the mechanical stability of the replicas, for example by infiltrating the wood template with low solid content precursor solution by applying several infiltration steps, increasing calcination temperature or adding a silicate layer onto the surface, and synthesize mechanically stable forsterite replicas.

At first, a facile synthesis process for alkaline earth metal carbonates such as $CaCO_3$ via hydrolysis from calcium di(methylcarbonate) ($Ca(OCOOCH_3)_2$) was developed. This precursor was synthesized by directly bubbling gaseous CO_2 through calcium dimethylate ($Ca(OCH_3)_2$) solution, which again was prepared by reacting calcium metal with methanol. These reactions are presented in **Equations (1) – (3)**.

The $CaCO_3$ sol obtained in the final reaction spontaneously (within an hour after the reaction) transforms into a gel. This synthesis route which was developed in previous works of our group demonstrated that alkaline earth metal carbonate nanoparticles, sols, gels and aerogels can be synthesized through simple one-pot processes from inexpensive and abundant starting

materials which makes for a very cost- and time-effective process. Moreover, because of the generally small molecules of the organometal precursors, the use of these precursors for the infiltration process approved to be most promising.

Synthesis of calcium dimethylate

$$Ca + 2\,CH_3OH \rightarrow Ca(OCH_3)_2 + H_2O\uparrow$$ **Equation (1)**

Synthesis of calcium di(methylcarbonate)

$$Ca(OCH_3)_2 + 2\,CO_2 \rightarrow Ca(OCOOCH_3)_2$$ **Equation (2)**

Formation of a calcium carbonate sol/gel

$$Ca(OCOOCH_3)_2 + H_2O \rightarrow CaCO_3 + 2\,CH_3OH + CO_2\uparrow$$ **Equation (3)**

These reaction steps were expected to lead to an understanding which precursors and synthesis conditions provide the most precise replicas with high mechanical stability at the same time. Apart from $CaCO_3$ replicas, the other promising target compounds were magnesium carbonate ($MgCO_3$) replicas. $MgCO_3$ can be synthesized following the same synthesis steps as in $CaCO_3$ preparation. Moreover, metal silicates such as magnesium silicate were also studied as replica materials, especially because of their high toughness. The forsterite replica was obtained by firstly infiltrating the wood template with methoxy magnesium methyl carbonate ($Mg(OCOOCH_3)(OCH_3)$) and subsequent immersion in tetraethyl orthosilicate (TEOS) solution. Lastly, it was attempted to synthesize a replica consisting of calcium silicate hydrate which constitutes the main phase in hardened cement. The silica replica was synthesized following the synthesis steps from the group of *Prof. Zollfrank*. After the surface OH groups of the silica replica had been partially ionized in basic solution, they were subsequently immersed in calcium hydroxide or calcium chloride solution to yield C-S-H.

3 Theoretical background and state of the art

Terms such as “bionics”, “biomimetic” and “biomineralization” are used to describe the approach of using natural structures and processes as inspiration for developing new materials. It is one of the main driving forces in studying biological materials from the viewpoint of Materials Science [9]. One possibility to combine the hierarchical structure of natural materials with a broad range of available materials is biotemplating. For example, biological materials are used as scaffolds or casting molds in order to synthesize ceramics, semiconductors, metals, polymers or composites of these materials [10]. Moreover, anisotropic ceramic materials with a hierarchical pore structure ranging from the nanometer to the millimeter scale are interesting for applications as filter, catalyst support or micro reactor device structures [11].

A number of hierarchically structured inorganic materials have been synthesized recently by using biological templates originating from plants (*e.g.* wood, seed, reed, bamboo) or animals (*e.g.* shell, nacre, tooth, bone) [9]. Some of them are mineralized by forming organic/inorganic nanocomposites typically constituting a fibrous matrix reinforced with crystalline or amorphous nanoparticles, for example bone, teeth and antler which consist of a fibrous protein matrix (mainly collagen) reinforced with crystalline calcium phosphate nanoparticles [9, 12-14]. In contrast, wood cell walls usually do not contain substantial amounts of minerals, being polymer/polymer composites of crystalline cellulose nanofibrils in an amorphous matrix of hemicelluloses and lignin [5, 9]. The structures of these templates were replicated by infiltrating the biotemplates with inorganic precursors and subsequent removal of the organic matrix *via* chemical or thermal treatment [7]. Recently, the design of novel ceramic materials with specific functional properties and structures by mimicking the hierarchical cellular structure of wood has attained particular interest [15-17].

3.1 Wood

3.1.1 Structure and Ultrastructure

Wood exhibits a perfect combination of high strength, stiffness and toughness at low density. These properties derive from its cellular anatomy and the complex composite structure of the cell wall which is reinforced by cellulose fibers [18]. The reason that wood

provides both low density and high stiffness is owed to the main function of the tree trunk that has to serve as a conduit for water and nutrients, and at the same time to support the weight of the branches and leaves [7].

Different kinds of woods exist and can be observed without optical instruments. There are softwoods and hardwoods this with differences between various species, and even within the same sample, such as sapwood and heartwood, growth rings, earlywood and latewood, etc. exist. The ratio of cell-wall thickness to the cell diameter is directly related to the apparent density of the wood which is an important parameter for the performance of light weight structures [9].

Softwoods such as coniferous trees possess a simple structure. The softwood contains 90 – 95% of tracheids which appear as square or slightly rectangular cells [19]. These cells pile up in radial axes. The cross-section of these cells shows a honeycomb structure, as is presented in **Figure. 2**. In the earlywood, the tracheid cells exhibit large diameters with thin walls. Opposite to this, in latewood the tracheid cells possess small diameters and thick walls (**Figure. 3)**. Generally, the stiffness and strength of wood is much higher along the direction of the long axis of the cells than in the perpendicular direction to the axis [9].

In wood, pores occur at very different scales; in the millimeter scale for the growth ring and vessel pores; in the micrometer scale for the longitudinal tracheid, fiber and transverse ray parenchyma; and in the nanometer scale for *e.g.* cellulose fibrils in the cell wall [18].

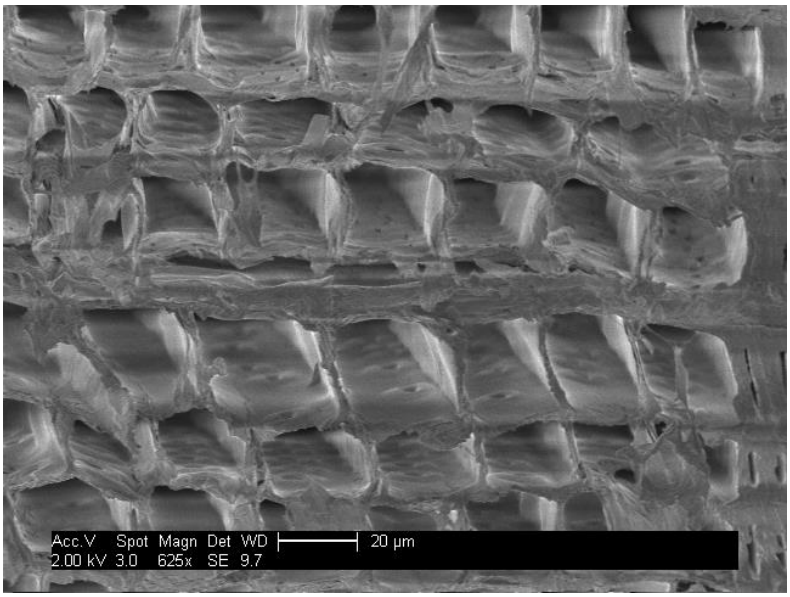

Figure 2. SEM image of pine wood exhibiting a honeycomb structure.

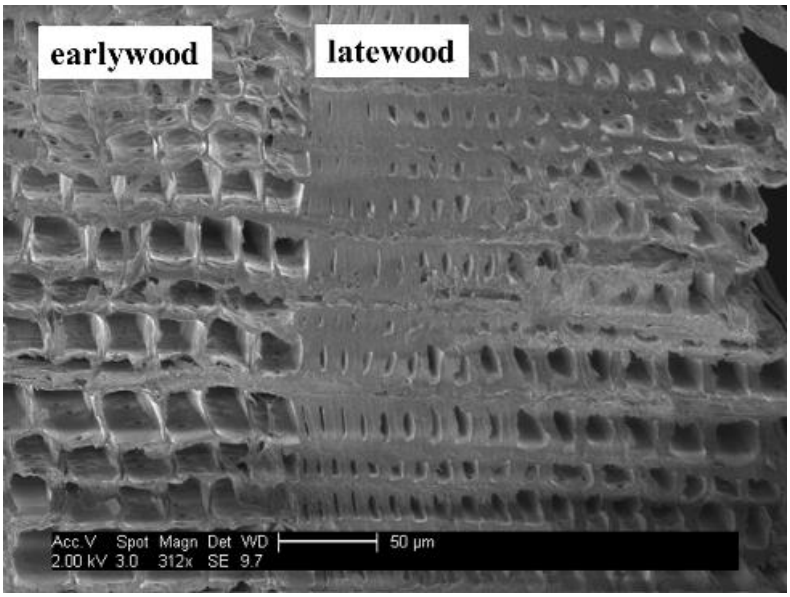

Figure 3. SEM images of earlywood and latewood sections in a pine wood sample.

3.1.2 Cell walls

The inner part of a cell wall consists of three main regions: the middle lamella (ML), the primary wall (P), and the secondary wall (S). Each region contains three major components: cellulose microfibrils, polyoses (or hemicelluloses), and a matrix or encrusting material, typically pectin in primary walls and lignin in secondary walls [5, 19]. The cell wall structure is illustrated in **Figure 4**.

Wood cells are adjacent to many other plant cells (**Figure 5**) [20] which hold aggregates of more than thousand cells to form an organ. Each individual cell adheres to another via the middle lamella [19]. Next to the middle lamella is the primary wall (S_1) which is a thin wall and generally indistinguishable from the middle lamella. The thickest layer is by far the secondary cell wall (S_2). Inside the S_2 layer is the relatively thin S_3 layer [19].

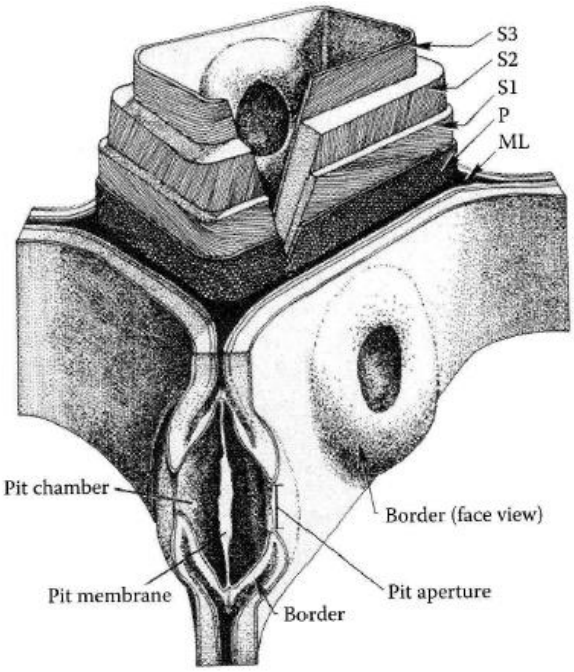

Figure 4. Schematic drawing of the cell wall illustrating the structural details of a pit and the various layers of the cell wall; middle lamella (ML), primary wall (P), and the secondary wall exhibiting the three layers S1, S2, and S3 (from [19]).

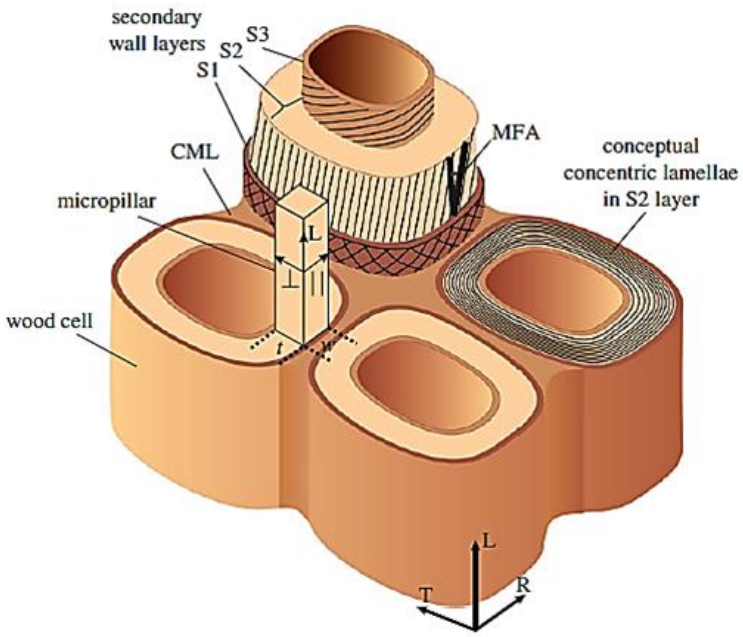

Figure 5. Schematic of cell wall layers within the cellular structure of wood. The concept of concentric lamellae in the S2 layer is schematically shown for one cell (from [20]).

The cell wall constitutes a fiber composite made of cellulose microfibrils embedded into a matrix of hemicelluloses and lignin [5, 19]. These cellulose microfibrils wind around the tracheids (tube-like wood cells) at an angle (right-handed helix) called the microfibril angle [7, 19], as is illustrated in **Figure 6**. Consequently, this structure is hierarchical at the nanometer level as was proven by small-angle X-ray scattering analysis (SAXS) [12, 21]. The cellulose microfibrils run at almost 90 ° to the cell axis in the S_1 layer and at around 0 - 45 ° in the S_2 layer [9]. The cellulose microfibrils are partly crystalline (**Figure 7**) and in spruce wood have a thickness of about 2.5 nm [6]. There are ionizable groups on cellulosic fibers including carboxylic acid groups, sulfonic acid groups, catecholic acid groups, and hydroxyl groups [22]. The general structure of cellulose is shown in **Figure 8**. Hemicelluloses are closely associated with cellulose and usually consist of more than one type of sugar unit, for example galactoglucomanan, arabinoglucuronoxylan, arabinogalactan, glucuronoxylan, glucomannan, etc., while lignins constitute highly complex and mainly aromatic polymers holding phenylpropane units [19].

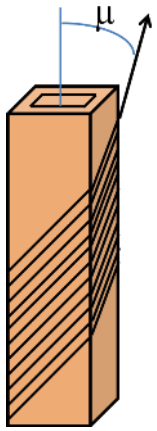

Figure 6. Schematic drawing of a wood cell (tracheid) illustrating the microfibril angle between the spiraling cellulose fibrils and the tracheid axis (adapted from [9]).

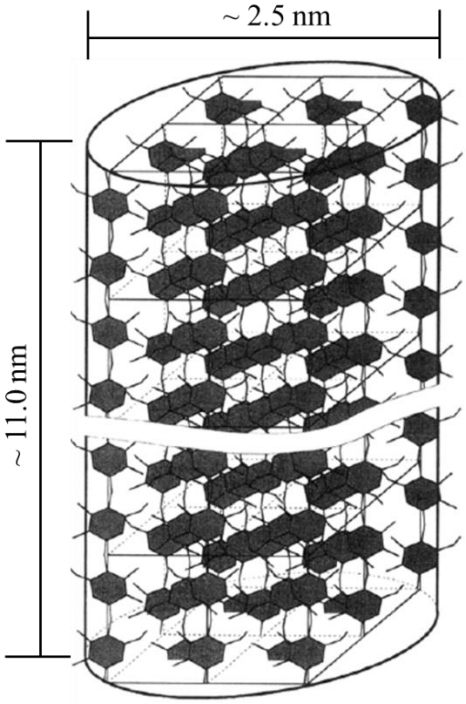

Figure 7. Model of the average crystalline regions occurring in an elementary cellulose fibril, as derived from SAXS and WAXS measurements [6].

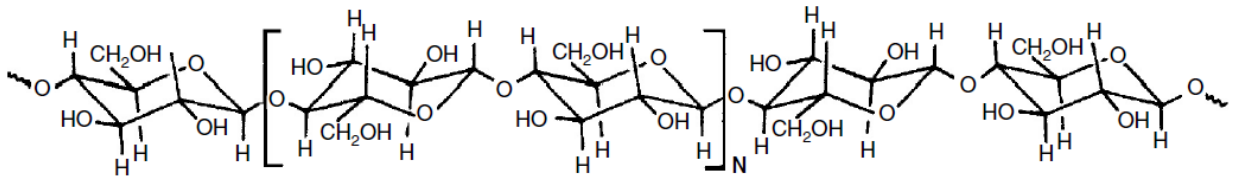

Figure 8. General structure of cellulose [19].

3.2 Wood template treatment

Extraction and delignification:

Before the infiltration process, the wood templates should be washed in order to remove any inorganic impurities [23]. Washing with a mixture of 2:1 by weight of toluene and ethanol is a promising method [8, 18]. An additional useful template treatment is delignification by using a mixture of sodium chlorite and acetic acid in water at 70 °C in order to partially remove lignin from the cell walls to open up the pores, to remove inorganic impurities and to increase the accessibility during the infiltration process [8, 23-25]. Wood maceration (delignification) prior to nanoparticle impregnation and the use of never-dried tissue present the key steps in the synthesis process, because they allow the replacement of the hemicellulose/lignin matrix by a nanoparticle sol and eventually make high-precision nanocasting with slow tissue drying and calcination possible [26].

3.3 Infiltration methods

3.3.1 Infiltration using concentration gradients

Inspired by our previous publication (paper #1 of this thesis), *V. Merk et. al.* [27] used dimethyl carbonate precursors to produce hybrid wood materials with improved fire retardance. The liquid phase holding the dissolved precursors enters the cell lumen and is imbibed by the nano- and submicron pores via capillary forces. Amorphous calcium carbonate forms by alkaline hydrolysis of dimethyl carbonate precursors in the presence of calcium ions

inside the cell wall structure. Concentration gradients across the bulk sample as well as rapid mineral precipitation in the wood lumina are induced by a pH shift causing *in situ* development of CO_2 gas. The process is illustrated in **Figure 9**.

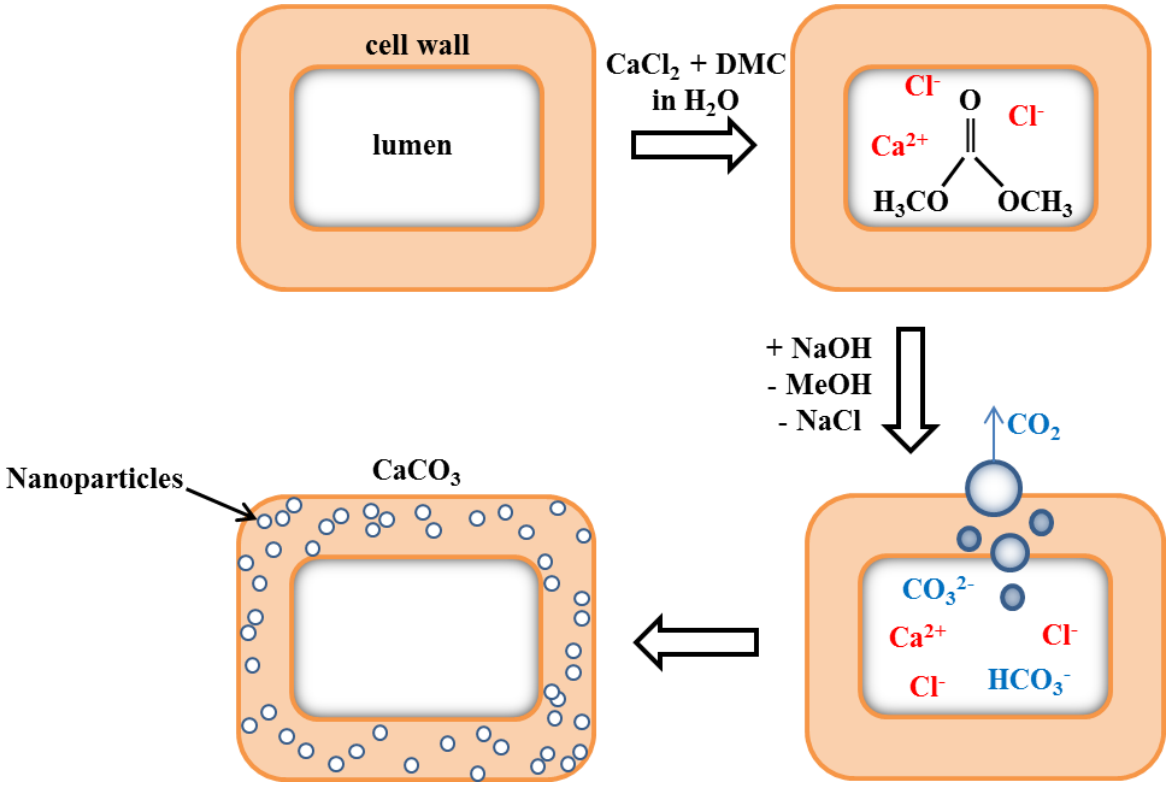

Figure 9. Schematic drawing of the mineralization of wood by alkaline hydrolysis of initially formed dimethyl carbonate in the presence of calcium ions in the wood matrix (adapted from [27]).

3.3.2 Sol-gel process

The sol-gel method presents an effective bottom-up approach to produce the desired material. In this process, firstly a sol which is a stable suspension of colloidal particles (nanoparticles) in a liquid is formed. Generally, the sol particles can be amorphous or crystalline, and may have a dense, porous or polymeric substructure. Moreover, subcolloidal chemical units can aggregate [4].

A gel constitutes a porous, continuous three-dimensional solid network of chemically bond (mostly covalent bonds) particles in a liquid phase. The amorphous network structures in sol-gel materials are formed based on kinetically controlled reactions (fast and (nearly) irreversible reactions) from molecular precursors which constitute the building blocks for the latter materials. In the gel, the sol particles agglomerate or aggregate through attractive van de Waals forces and/or minimization of the total surface or interfacial energy of the system. The aggregation can be prevented by repulsive forces from electrical charges or adsorbed polymers providing steric hindrance [4].

Rapid evaporation can induce gelation of the sol. During the drying process of wet gels by evaporation of the pore solution, capillary forces cause shrinkage of the gel network resulting in shrunken dry gels which are called xerogels [4]. Through capillary condensation, the pores contract abruptly as a result of attractive fluid-wall interactions whereas at larger pressures they expand again [28]. Because of this drying stress, monolithic gel bodies are often destroyed during the drying and granulate powders are formed. To prevent this stress, wet gels can be dried in a way that the pore and network structure of the gel is retained, resulting in a dried gel called an aerogel. One of the key steps in the fabrication of aerogels is the formation of a highly porous, three-dimensional network which means that the chemical parameters, especially the kind of precursors and the reaction conditions, influence the resulting microstructure. Aerogels can be achieved for inorganic, inorganic-organic and purely organic materials under controlled conditions and exhibit a typical solid content of only 1 – 5 vol % [4].

A common material produced via sol-gel processing is a silica sol or gel. The transformation of Si-OR- and Si-OH-containing species to siloxane units via condensation reactions is the basic chemical principle behind this sol–gel process. SiO_4 tetrahedra (or $RSiO_3$ tetrahedra in hybrid materials) connect to other units by sharing oxygen atoms in corners. A stable gel is obtained when the number of siloxane bonds (Si-O-Si) is maximized [29]. To achieve this, the number of silanol (Si-OH) and alkoxy (Si-OR) groups has to be minimized. The most common precursors are silicon alkoxides, mostly tetramethoxysilane (TMOS) or tetraethoxysilane (TEOS), and aqueous solutions of sodium silicate known as water glass [4, 29, 30]. Multicomponent inorganic gels can be produced via this method based on the polymerization reaction (i.e. hydrolysis and condensation) of the silanolate with other metal

alcoholates or suitable metal salts in the presence of a limited amount of water [4]. Furthermore, the sol-gel method is also used to synthesize layered calcium organosilicate hybrids containing covalently linked organic functionalities. Their synthesis involves the reaction of calcium salts and organo trialkoxysilanes with alkyl and phenyl functionalities in an alkaline aqueous/ethanolic solution [31], to synthsize clear and transparent $CaO\text{-}SiO_2$ glasses from TEOS and calcium nitrate [32] or monolithic transparent glasses of $CaO{\cdot}9SiO_2$ and $CaO{\cdot}4SiO_2$ from $Si(OEt)_4$ and $Ca(OEt)_2$ [33], and to synthesize covalently bonded polymer-calcium silicate hydrate composites [34].

The chemical reactions occurring in the sol–gel process can be described as follows:

≡Si-OR + H_2O → ≡Si-OH + ROH	Hydrolysis	**Equation (4)**
≡Si-OH + ≡Si-OR → ≡Si-O-Si≡ + ROH	Condensation	**Equation (5)**
≡Si-OH + ≡Si-OH → ≡Si-O-Si≡ + H_2O	Condensation	**Equation (6)**

In aqueous silicate systems, the gelation process is most often initiated by pH changes and in alkoxide precursor systems by addition of water to generate Si-OH groups via hydrolysis reactions [29].

The pH value presents an essential parameter to control the texture of gels formed from water glass solutions. Using acid or base catalysis involves completely different reaction mechanisms. The reaction mechanisms are the same for both silicate and alkoxysilane precursors. Under basic conditions, the reactions are based on a nucleophilic attack (S_N2) mechanism [29]. While in acid conditions *e.g.* at pH < 5, hydrolysis is favored, and condensation is the rate-determining step, therefore a large number of monomers or small oligomers with reactive Si-OH groups are formed simultaneously. On the contrary, at pH > 5, the condensation presents the faster step, therefore the hydrolyzed species are consumed immediately, because here hydrolysis is the rate-determining step [29].

For the sol-gel transition (gelation process), the structural development of silica gels from molecular precursors is shown in **Figure 10**. The initially formed primary nano particles can either aggregate once they have reached a certain size (at the descending branches in the left part of **Figure 10**) or continue to grow (at the descending branches in the right part of

Figure 10), depending on the experimental conditions, especially the pH value. Aggregation and condensation of the sol particles increases the viscosity of the sol gradually [29].

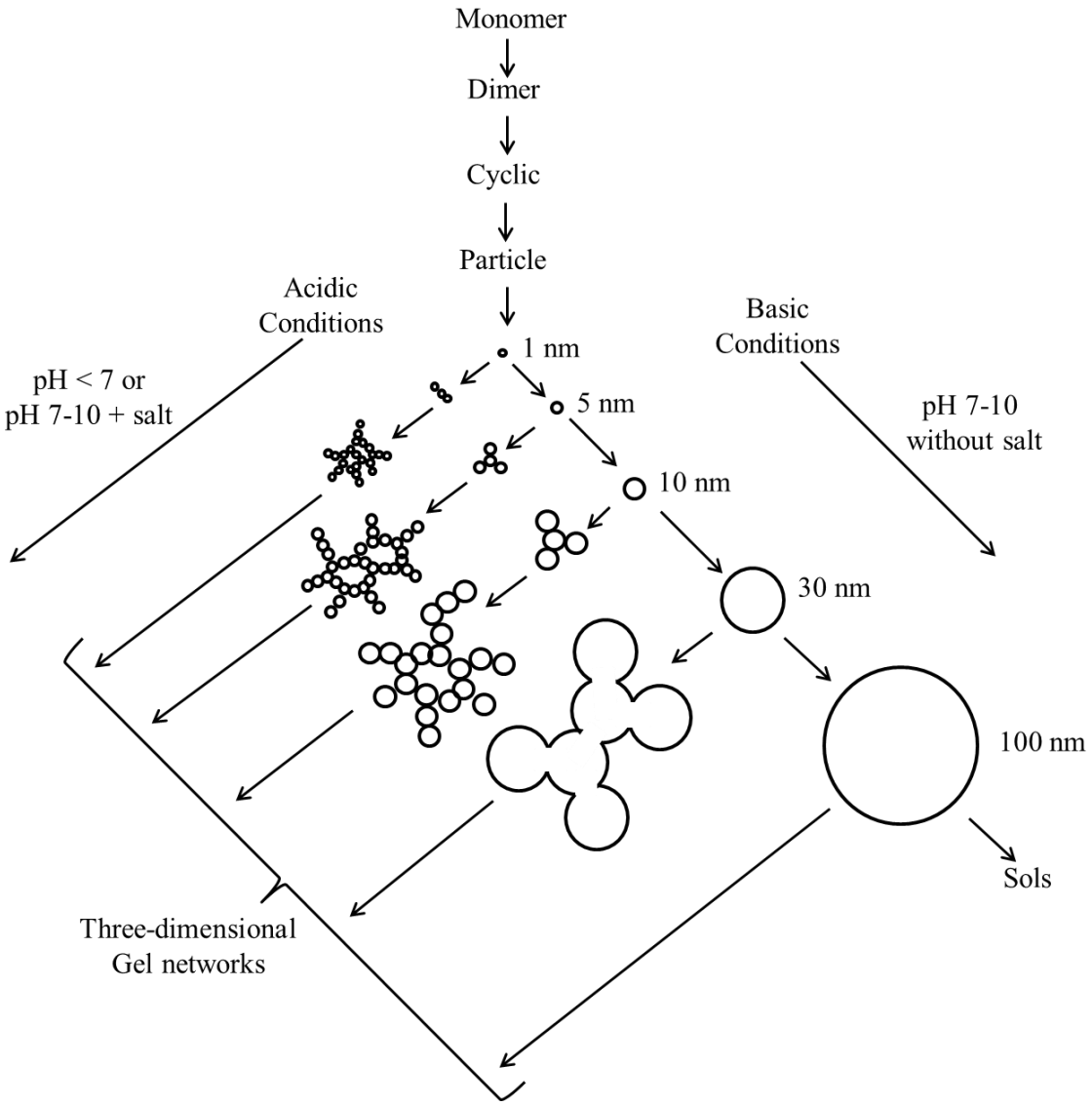

Figure 10. Principle of the structural development of silica gels (adapted from [29]).

Figure 11 illustrates the bond formation between silica particles with minor or no charge repulsion. Collision of the silica particles results in the formation of interparticle siloxane bonds which are base-catalyzed. Through this bonding, the particles grow together [35].

When TEOS is infiltrated into wood, additional condensation reactions might take place, as is shown below (Me = methyl, CH_3) [8]:

$$\text{Wood-Me-OH} + \text{Si(OEt)}_{4-x}\text{(OH)}_x \rightarrow \text{Wood-Me-O-Si(OEt)}_{4-x}\text{(OH)}_{x-1} + \text{H}_2\text{O} \qquad \textbf{Equation (7)}$$

$$\text{Wood-Me-OH} + \text{Si(OEt)}_{4-x}\text{(OH)}_x \rightarrow \text{Wood-Me-O-Si(OEt)}_{3-x}\text{(OH)}_x + \text{EtOH} \qquad \textbf{Equation (8)}$$

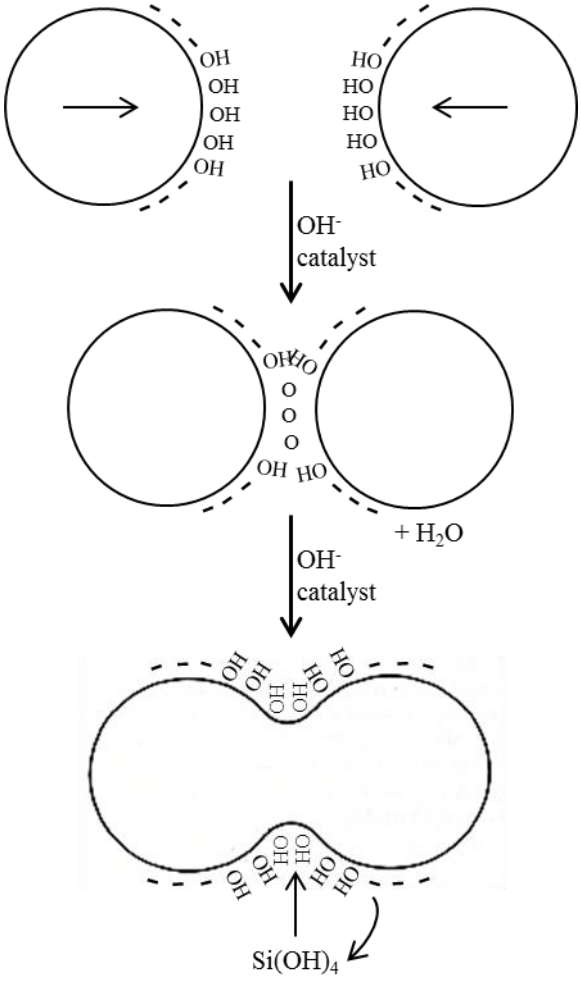

Figure 11. Principle of the bond formation between silica particles with minor or no charge repulsion (adapted from [35]).

3.4 Template removal

Under thermal treatment, polyoses (hemicelluloses) present in beech (hard wood) have been shown to degrade at 270 °C, followed by cellulose pyrolysis around 350 °C [27]. This degradation cascade is similar to that of soft wood such as spruce wood (*Picea abies*). Disintegration of the TEOS infiltrated hemicelluloses takes place between 250 and 300 °C, leaving the cellulose elementary fibrils embedded in a silica matrix. The silica network now presents a stable network in the form of long fibrils of about 10 nm. The next step is the disintegration of the cellulose elementary fibrils at temperatures between 350 and 450 °C, leaving empty pores of about 2 nm in diameter within the silica fibrils, as is describes by *Zollfrank et al.* [36].

In another study on the ultrastructural development of the soft wood (Scots pine, *Pinus sylvestris L.*) cell wall during pyrolysis, *Zollfrank et al.* found that at first the polyoses are degraded, while the cellulose microfibril orientation is still in place up to 225 °C, as was observed by transmission electron microscopic (TEM) imaging together with elemental analysis. At temperatures higher than 250 °C, the cellulose microfibrils were no longer observed, while the lignin containing middle lamella (CML) was still visible. The CML decreases gradually when temperature is raised up to 275 °C. Beginning at 300 °C, the cell wall became entirely isotropic [37]. The model proposed by the authors for the ultrastructural development of the softwood cell during the pyrolytic conversion is illustrated in **Figure 12**.

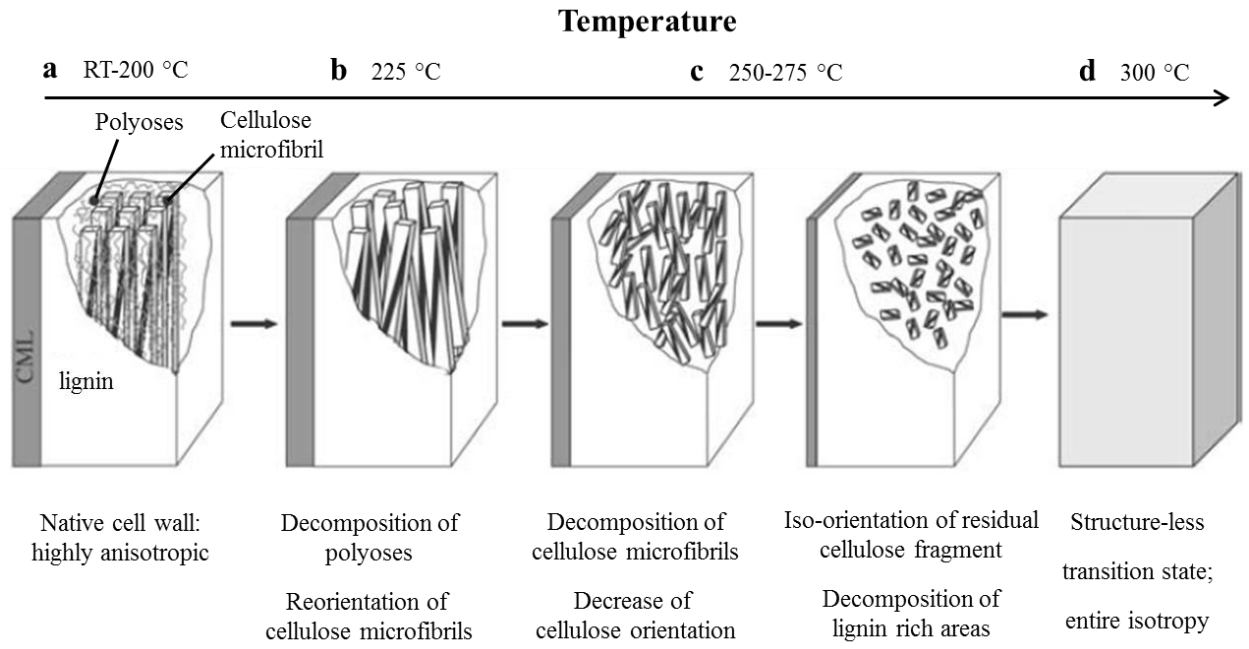

Figure 12. Proposed model for the ultrastructural development of the softwood cell during pyrolytic conversion. [37]

3.5 Replicas in other previous studies

There are several successful works on the replication of the hierarchical structure of wood from the micrometer to the nanometer scale. For example, a hierarchically ordered ceramic silica material was obtained by *in situ* mineralization of the ordered cellular structure in wood tissues (poplar and pine) by infiltrating the wood template with tetraethylorthosilicate as a silicate precursor together with cetyltrimethylammonium chloride as a surfactant [38]. The process of replication takes place via a modified sol-gel process in order to be able to adjust the hydrolysis rate easily by changing the solvent ratio and the acidity of the solution to avoid bulk precipitation or gelation of the silicate species during the entire process. The bulk precipitation has to be prevented in order to let the silicate species penetrate the cell wall structures and hydrolyze and condensate around the cellular tissues. Incorporation of the surfactant micelles in the silica network provides pathways for the organic decomposition products to leave during calcination without destroying the whole structure and also produces organized nanoporous channels [38].

Hierarchical iron oxide with a controllable porous structure was obtained by using wood templates (Paulownia, Lauan, pine and fir) infiltrated with ferric nitrate in a solvent mixture of ethanol and deionized water. Different wood templates and calcination temperatures lead to different pores in size, shape and distribution. High temperature leads to the increase in the size of the Fe_2O_3 particles and causes larger pore sizes, but decreased pore volume. Iron oxides prepared according to this wood template method have been proven to exhibit a hierarchical structure and show pore sizes at different scales ranging from about 20 nm to 50 µm [39].

A highly crystalline porous oxide of $Ce_{0.5}Zr_{0.5}O_2$ was synthesized by using nanoprecision casting of pine wood tissue with nonfunctionalized, crystalline nanoparticles [26]. The native wood samples were macerated (delignified) in a solution of acetic acid and hydrogen peroxide and kept moist in order to avoid collapse and warping of the structure due to drying. Acidic sols of $Ce_{0.5}Zr_{0.5}O_2$ were impregnated into the specimens to obtain cellulose/nanoparticle composites by using $[(NH_4)_2Ce(NO_3)_2]$, $ZrOCl_2{\cdot}8H_2O$, HCl, CH_3COOH and H_2O_2. Calcination of the impregnated samples at 500 °C for 24 h led to a material exhibiting the replicated hierarchical structure of wood in nanometer precision, including the orientation and long-range ordering of the cellulose microfibrillar structure [26].

Hierarchically structured phosphor materials based on soft wood could be fabricated using tailor-made precursor sols and salt solutions. Stoichiometric amounts of the precursor nitrate solutions of $Al(NO_3)_3{\cdot}9H_2O$, $Sr(NO_3)_2$ and $Eu(NO_3)_3{\cdot}5H_2O$ were dissolved in a solvent composed of distilled water and ethanol and infiltrated into pine wood. After temperature treatment of the infiltrated pine wood above 1100 °C, the biomorphous $SrAl_2O_4:Eu^{2+}$ ($Sr_{0.97}Al_2O_4:Eu_{0.03}$) with a structure mimicking the cellular anatomy of pine wood was obtained [18]. X-ray storage phosphor $BaFBr:Eu^{2+}$ is manufactured by applying vacuum assisted repeated infiltration of wood tissue (*Pinus sylvestris*) and precipitation from the chemical reaction of NH_4F, $BaBr_2{\cdot}2H_2O$ and $EuCl_3{\cdot}6H_2O$ in methanol [40]. A micron-scale replica of single-phase $Y_2O_3:Eu^{3+}$ ($(Y_{0.95}Eu_{0.05})_2O_3$) possessing a nanoscale crystallite structure was prepared by infiltrating pine wood with a precursor sol of yttrium oxide (Y_2O_3) and europium oxide (Eu_2O_3) dissolved in 10 vol% nitric acid and adding citric acid as the chelating agent. After calcination at 750 °C, the original wood cell walls were completely transformed into phosphor struts with pore

sizes between 5 and 20 µm. This preparation method is convenient to prepare highly porous and nanocrystalline phosphor materials. Furthermore, highly uniform Eu^{3+} lattice sites were obtained. The increased lattice constant of the materials reduces radiative transitions, and the emission quenching due to defects or functional groups existing on the surface of these highly porous materials is low [41].

Furthermore, the structure of wood has been reported to be replicated successfully on all levels of hierarchy from the macroscopic to the nanoscopic level of the cellulose elementary fibrils in the form of silica replicas. The delignified spruce wood which optionally can be further functionalized with maleic anhydride was infiltrated with tetraethyl orthosilicate (TEOS) in ethanol. The aim to functionalize the wood template with maleic anhydride was to reduce the shrinkage of the samples and to increase the uptake of material during the infiltration process. During calcination at 500 °C, the rest of the organic template was removed by oxidation, thus leaving a positive silica replica. The fibrillar structures parallel to the original cellulose fibrils at length scales in the order of 10 nm were evidenced by using small angle X-ray scattering. It was found that one infiltration cycle was insufficient to completely replicate the structure on the nanometer scale. Several cycles of infiltration with lower amounts of TEOS was the most effective way in their study [8].

3.6 Replicas in this study

3.6.1 SiO_2

In applications such as catalysis, sensoring, pharmaceuticals, building materials, etc., hierarchically structured inorganic materials have been recognized as attractive compounds [42]. Nano- and mesoporous materials are utilized for such purposes as well. For example, mesoporous silica materials (*e.g.* MCM-41) are prepared with quaternary ammonium surfactants (“quats”) as templating agents [43, 44], and nanoporous silica aerogels are fabricated via sol-gel processes utilizing alkoxysilane precursors [45, 46]. Among those materials, aerogels are the most interesting materials because of their unsurpassed heat insulating properties deriving from their nanoporosity and the Knudsen effect [47]. It should be noted that generally pores are classified as micropores (width, $w < 2$ nm), mesopores ($2 \text{ nm} < w < 50$ nm) and macropores ($w > 50$ nm), according to a IUPAC recommendation [4, 48, 49]. In the silica replicated wood, there

are: 1) macropores (the largest pores) which derive from the lumina of the tracheids, 2) mesopores at the interstices of the microfibrils, and 3) pores which correspond to the space originally occupied by the cellulose elementary fibrils [50].

Since *Kistler* had first synthesized a silica-based aerogel via a wet chemical sol-gel process and subsequent supercritical solvent extraction in the 1930s, various types of aerogels based on carbon, alumina, transition metal oxides or main-group metal oxides were introduced [51]. Aerogels are a great example to demonstrate that the profound knowledge and understanding of the chemistry of precursors and of the formation of the solid are necessary for the targeted optimization and tailoring of materials properties [4]. Furthermore, such porous materials are also interesting as functionalized supports for other applications, for example the adsorption of heavy-metal ions from aqueous solutions using mercapto-modified silica particles [52].

3.6.2 $CaCO_3$

Calcium carbonate has been used because of its compatibility with cement. It is known for long time that the Romans used mortar prepared from sand and lime obtained by heating limestone, $CaCO_3$ [53, 54]. This burnt limestone, CaO, hardens under CO_2 absorption from the air which will turn to limestone again [55, 56]. Ca is the fifth abundant element in the earth's crust with a percentage of around 3.63% [55].

There are several routes to synthesize a $CaCO_3$ aerogel. A facile way resulting from the condensation of vaterite nanoparticles was reported in a communication from our group in 2009 [51]. In this synthesis, the hydrolysis of calcium di(methylcarbonate) which was obtained by the reaction of CO_2 with CaO in abosolute methanol is controlled. The $CaCO_3$ alcogel was then dried under supercritical conditions with CO_2 to produce the $CaCO_3$ aerogel. The sequence of reactions is as below:

$$CaO + 2\,CH_3OH \longrightarrow Ca(OCH_3)_2 + H_2O \qquad \textbf{Equation (9)}$$

$$CaO + 2\,H_2O \longrightarrow Ca(OH)_2 \qquad \textbf{Equation (10)}$$

$$Ca(OH)_2 + 2\,CH_3OH \longrightarrow Ca(OCH_3)_2 + 2\,H_2O \qquad \textbf{Equation (11)}$$

$Ca(OCH_3)_2 + 2\,CO_2 \longrightarrow Ca(OCOOCH_3)_2$ **Equation (12)**

$Ca(OCOOCH_3)_2 + H_2O \longrightarrow CaCO_3\,(sol/gel) + 2\,CH_3OH + CO_2$ **Equation (13)**

The calcium carbonate aerogel formation occurs in a three-step process which is presented in **Figure 13** [51].

Owing to their nanoporosity, recently calcium carbonate aerogels have been considered as a potential replacement for polystyrene foam contained in heat insulating renders and panels used extensively by the construction industry [51, 57].

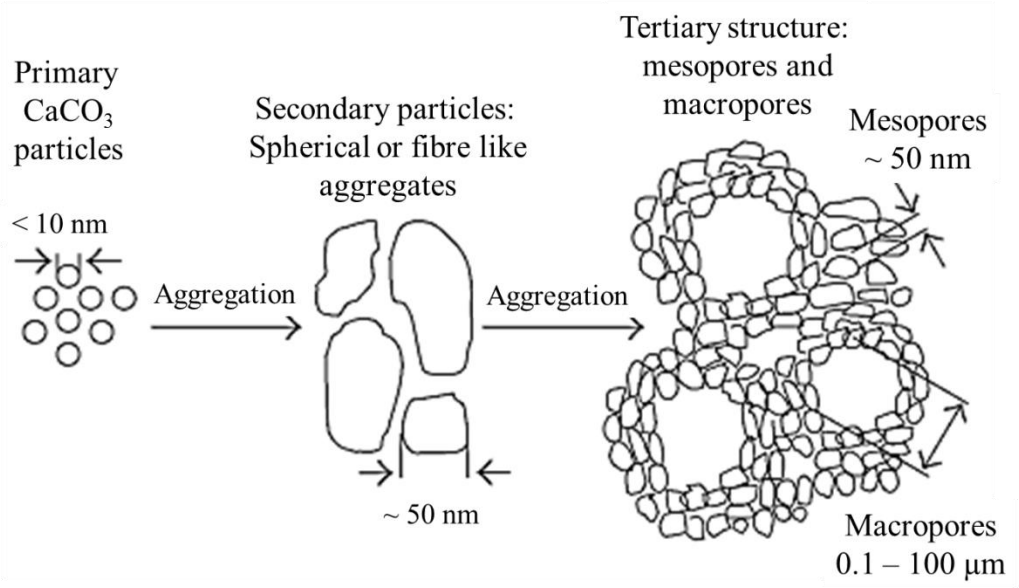

Figure 13. Schematic drawing of the three-step reaction process involved in the formation of the $CaCO_3$ gel (from [51]).

3.6.3 $MgCO_3$

Magnesium (Mg) is an alkaline-earth metal like calcium (Ca) [55]. Magnesium carbonate, $MgCO_3$, is found in two forms in the nature: dolomite, $MgCa(CO_3)_2$ (pearl spar, brown spar) and magnesite, $MgCO_3$ (talc spar, bitter spar) [58]. The usual way how this mineral was formed is strip mining deposition. In the lab it can be prepared in aqueous solution by combining Mg^{2+} and carbonate ions (a sufficient excess of free carbon dioxide). Magnesium

oxide (Magnesia), MgO is produced industrially by roasting $MgCO_3$ or $MgCa(CO_3)_2$, as is shown in **Equations 14-15**. Calcination of $MgCO_3$ or magnesium hydroxide, $Mg(OH)_2$ at 600 – 1000 °C yields a loose, white MgO powder. This material binds water, therefore it is used as binder in mortar (caustic magnesia) for construction [58]. Sintered magnesia is used to produce highly heat-resistant bricks called magnesia bricks, which are used for the cladding of electric furnaces in steel production, etc. It is also used for laboratory equipment, such as tubes, crucibles, watch glasses, etc. For insulation purposes, melted magnesia is used in electrical heaters [58]. In addition, MgO is widely used as a substrate in the fabrication of the high-T_c superconducting thin film [59].

$$MgCO_3 \rightarrow MgO + CO_2 ; \qquad \textbf{Equation (14)}$$

$$MgCa(CO_3)_2 \rightarrow MgO + CaO + 2\,CO_2 \qquad \textbf{Equation (15)}$$

Magnesium carbonate xerogels and aerogels which consist of networks of magnesium carbonate nanoparticles were synthesized earlier by our group via controlled hydrolysis of methoxy magnesium methyl carbonate, $Mg(OCOOCH_3)(OCH_3)$ as is shown in **Equations 16-18** [60]. This facile synthesis is based on the reaction between magnesium metal and methanol to form magnesium methanolate which was dispersed in methanol [61, 62]. After CO_2 had been bubbled through the suspension, it turned into a clear solution of methoxy magnesium methyl carbonate, as was confirmed by infrared spectroscopy and quantification of the mass of dried product obtained [60, 63]. A hydrolysis reaction occurred after addition of water to the methoxy magnesium methyl carbonate solution leading to magnesium carbonate.

These aerogels composed of alkaline earth metal compounds are of special interest for construction applications because of their high compatibility and inertness towards cement [60].

$$Mg + 2\,CH_3OH \rightarrow Mg(OCH_3)_2 + H_2\uparrow \qquad \textbf{Equation (16)}$$

$$Mg(OCH_3)_2 + (1+x)\,CO_2 \rightarrow Mg(OCOOCH_3)(OCH_3)\cdot xCO_2 \qquad \textbf{Equation (17)}$$

$$Mg(OCOOCH_3)(OCH_3)\cdot xCO_2 + H_2O \rightarrow MgCO_3 + 2\,CH_3OH + xCO_2\uparrow \qquad \textbf{Equation (18)}$$

Magnesium oxide (MgO) is obtained when $MgCO_3$ is burned at temperatures > 500 °C, as is shown in **Equation 19** [56].

$$MgCO_3 \rightarrow MgO + CO_2 \uparrow \quad \textbf{Equation (19)}$$

3.6.4 Mg_2SiO_4/$MgSiO_3$

Forsterite (Mg_2SiO_4) is named after the German scientist Johann Forster [64, 65]. Mg_2SiO_4 ceramics are of particular interest because of their low-cost, easily processable and light-weight characteristics [66]. This material is promising as a potential alternative to calcium phosphate bioceramics, because it shows exceptionally high toughness, close to that of cortical bones [67]. Forsterite-rich olivine is used to make fire-proof bricks and highly fire-resistant mortars, as an additive to ores in blast furnace processes, and for heat storage media in night storage radiators [58]. Olivine is known as the most abundant mineral in the Earth's upper mantle and transition zone [68].

Through a sol-gel process using $Mg(NO_3)_2 \cdot 6H_2O$ and colloidal SiO_2 with an initial molar ratio of MgO to SiO_2 of 2 and subsequent calcination at 1450 °C, pure forsterite ceramics with exceptionally high bending strength and fracture toughness, even higher than that of currently known hydroxyapatite ceramics, were obtained [69]. The mechanical strength decreased rapidly when the sintering temperature was increased to 1550 °C, because at this high sintering temperature, the pores were trapped in the grains as a result of grain growth. This result agrees well with a study of the sinterability of forsterite powder produced by a solid-state reaction, using magnesium oxide and talc ($Mg_3Si_4O_{10}(OH)_2$) [70]. It was found that the mechanical properties were improved when the calcination temperature was increased from 1200 to 1400 °C, but further increase of the sintering temperature above 1400 °C deteriorated the hardness and fracture toughness of the forsterite sample. The critical grain size in their study was found to be 21.74 µm and a fracture toughness 4.88 $MPam^{1/2}$[70] which is within the range of that of human bone (2-12 $MPam^{1/2}$) [71].

This forsterite material showed good biocompatibility in an in vitro study [69, 72]. Forsterite nanopowder synthesized in a sol-gel process involving $Mg(NO_3)_2 \cdot 6H_2O$, colloidal silica, polyvinyl alcohol polymer, sucrose and nitric acid possessed higher dissolution rates

during immersion in simulated body fluids than conventional forsterite powders and also possessed the ability to form apatite [72, 73].

Nonstoichiometric forsterite ceramics were prepared by a conventional solid-state ceramic preparation route using high-purity MgO and SiO_2 [74]. The powders were mixed and milled for 12 h in a polyethylene bottle charged with zirconia balls using ethanol as a medium, subsequent drying and calcination at 1200 – 1350 °C in air for 3 h. They found that a single-phase forsterite Mg_2SiO_4 could be obtained by calcining at 1350 °C. At this temperature, MgO is consumed and single-phase Mg_2SiO_4 is formed. The adequate amount of MgO could provide enough MgO to react with $MgSiO_3$ further to form Mg_2SiO_4. It could also provide enough MgO to react with amorphous SiO_2 to directly form Mg_2SiO_4. The results indicate that adequate addition of MgO can suppress the formation of the secondary phase $MgSiO_3$ as a by-product, however excessive addition of MgO leads to residual MgO as a secondary phase [74].

3.6.5 Calcium Silicate Hydrate (C-S-H)

The poorly crystalline or amorphous calcium silicate hydrates (so called “C-S-H”) are the main binding phases in all Portland cement-based systems possessing various compositions [75-78]. The C-S-H formed by the hydration of tricalcium silicate (alite, C_3S) or β-dicalcium silicate (belite, β-C_2S) which both are the main constituents in Portland cement, usually is called “C-S-H gel” while the C-S-H made via “synthetic” preparation routes such as the hydrothermal reaction of CaO and SiO_2 in aqueous solution is called “C-S-H phase” [79]. The formation of the “C-S-H gel” from C_3S and C_2S is illustrated in **Equations 20-23** [80].

Alite (C_3S):

$$2\,(3\,CaO\cdot SiO_2) + 6\,H_2O \rightarrow 3\,CaO\cdot 2\,SiO_2\cdot 3\,H_2O + 3\,Ca(OH)_2 \qquad \textbf{Equation (20)}$$

↑ ↑

C-S-H Portlandite

This equation can be written in a short form as:

$2\ C_3S\ +\ 6\ H\ \rightarrow\ C_3S_2H_3\ +\ 3\ CH$ **Equation (21)**

Belite (C_2S):

$2\ (2\ CaO \cdot SiO_2)\ +\ 4\ H_2O\ \rightarrow\ 3\ CaO{\cdot}2\ SiO_2 \cdot 3\ H_2O\ +\ Ca(OH)_2$ **Equation (22)**

↑ ↑

C-S-H Portlandite

This equation can be written in a short form as:

$2\ C_2S\ +\ 4\ H\ \rightarrow\ C_3S_2H_3\ +\ CH$ **Equation (23)**

Various structures of C-S-H are formed depending on the variation of the Ca/Si ration, the silicate content, and the contents of Si−OH and Ca−OH [79]. As models for crystalline calcium silicate hydrates, 1.4-nm tobermorite and jennite are used [78, 79, 81]. The structure of 1.4-nm tobermorite, $Ca_5Si_6O_{16}(OH)_2{\cdot}8H_2O$ is based on a composite layer composed of a distorted central Ca−O sheet connected to single dreierketten on both sides [79]. A dreierkette consists of silicate tetrahedra which coordinate to Ca^{2+} by connecting in a repeated kinked pattern after every three tetrahedra. Two of the three tetrahedra (paired tetrahedra) share O−O edges with the central Ca−O part of the layer, while the third tetrahedron (bridging tetrahedron) shares an O atom at the pyramidal apex of a Ca polyhedron and connects the two paired tetrahedra [79, 81, 82]. This structure is illustrated in **Figure 14.** Defects such as the omission of bridging tetrahedra, or variations in the contents of interlayer Ca and protons attached to $Si{-}O^-$ allow variations in the Ca/Si ratio [79].

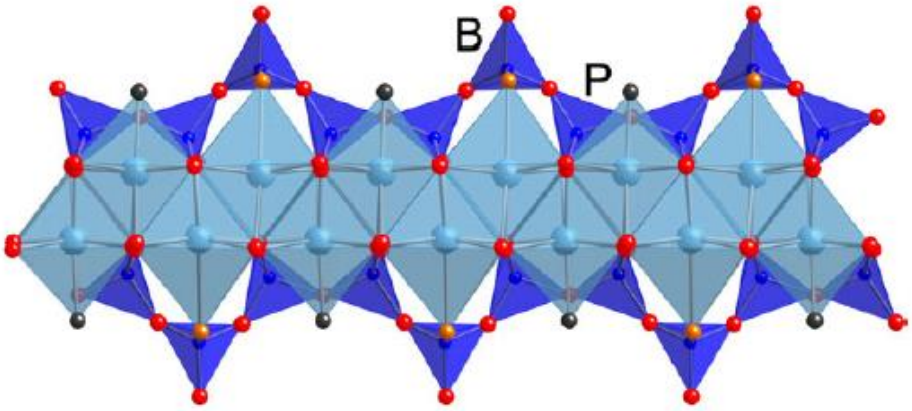

Figure 14. Schematic diagram showing chains of dreierketten present in tobermorite (in theory they are of infinite length) (P = paired tetrahedra, B = bridging tetrahedron); after [81].

4 Experimental Section

4.1 Preparation of the templates

The preparation followed the method established in 1971 by *Ahlgren et al*. [23]. It is commonly practiced in *C. Zollfrank*'s group from where all templates were received.

Sections (either cubes with side lengths of 1 cm or radial thin discs of 1 cm (tangential and radial) in diameter and 0.3 mm (axial) in thickness) were cut from the sapwood of spruce (*Picea abies*) or pine trees (*Pinus sylvestris*), weighed and subjected to a series of chemical treatments. The sample axes are shown in **Figure 15**.

In the first step, 150 g of wood were washed by extraction for 6 h in a Soxhlet apparatus using 500 mL of a 2:1 by weight mixture of toluene and ethanol. This was followed by another extraction over 6 hrs with the same amount of pure ethanol. Between the processing steps, all samples were stored in ethanol to prevent drying.

For preparation of the templates, 1 g of this wood was placed in an oxidizing solution containing 1.4 g of sodium chlorite ($NaClO_2$) and 0.5 g of acetic acid in 23.1 g of deionized water. Delignification was carried out twice at 70 °C for 3 h each whereby the delignification solution was renewed after the initial 3 h. Afterwards, a mild vacuum from a waterjet pump was applied for half an hour. Following the delignification treatment, the templates were immediately extracted with ethanol to remove any residual solutions of reagents [23]. A photo of a delignified spruce wood template is presented in **Figure 16**.

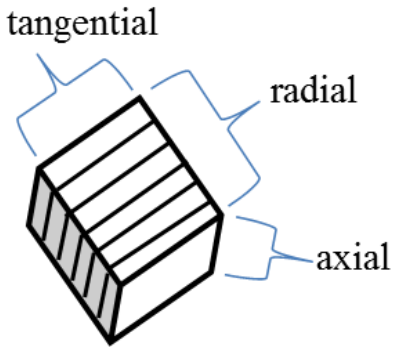

Figure 15. Schematic of a wood template showing the tangential, radial and axial axes.

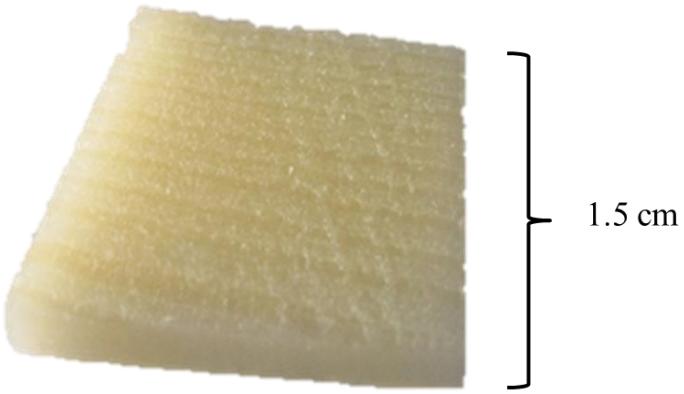

Figure 16. Photograph of a delignified spruce wood template.

4.2 Infiltration process

4.2.1 Calcium carbonate and calcium oxide replicas

Calcium metal in the amount of 1.5 g (0.0374 mol) was suspended in 250 mL of absolute methanol (dried and stored over a molecular sieve, 3 nm) and heated to 65 °C to produce a solution of $Ca(OCH_3)_2$. After 90 min of stirring at room temperature, carbon dioxide gas was bubbled through the $Ca(OCH_3)_2$ solution. After 90 min of reaction time, a turbid solution of $Ca(OCOOCH_3)_2$ had formed which was centrifuged. The clear solution (containing ~ 13 g of the salt) was rinsed into a vial which contained the spruce wood template. Infiltration of the wood cells occurred during the drying process on a hotplate performed at 70 °C as is shown in **Figure 17**. The infiltrated wood template was then kept in an oven at 80 °C for 7 h.

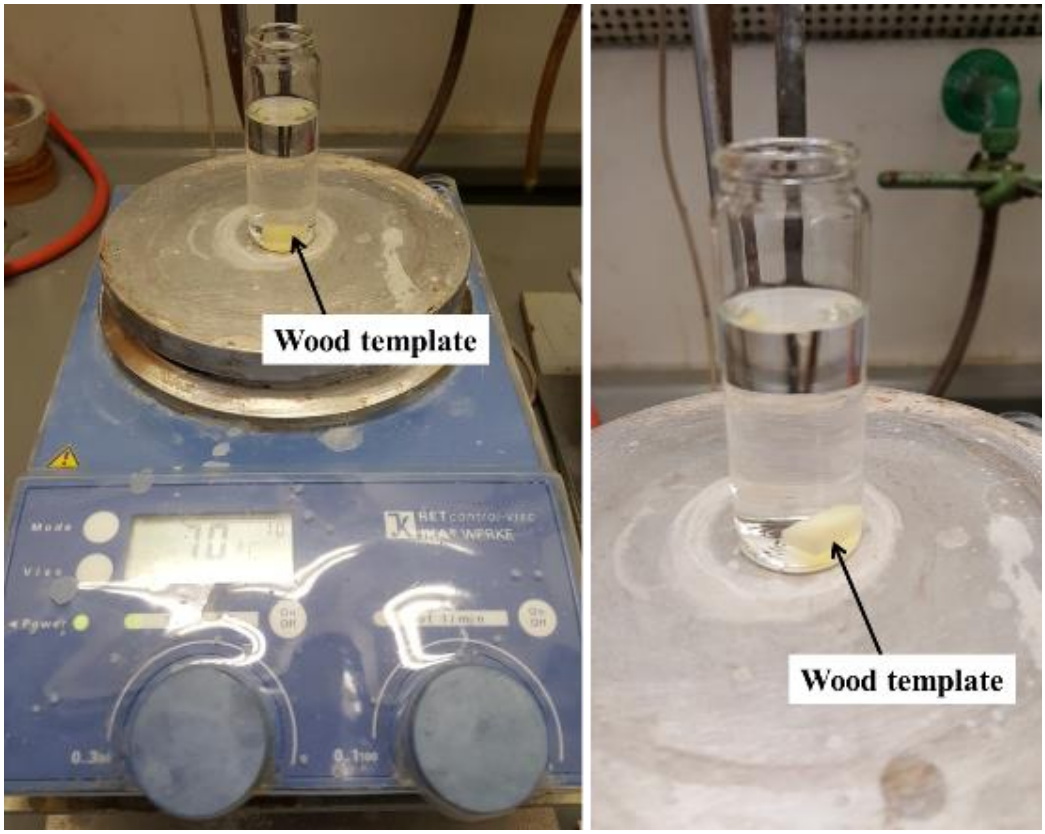

Figure 17. Photographs of a delignified spruce wood template placed in the clear solution of $Ca(OCOOCH_3)_2$ during the drying process on a hotplate.

4.2.2 Magnesium oxide and magnesium silicate replicas

Magnesium oxide replicas

Magnesium metal in the amount of 2.5 g (0.1029 mol) for high solid content, or 0.5 g (0.0206 mol) for low solid content, was dissolved in 250 mL of absolute methanol (dried and stored over a molecular sieve, 3 nm) and heated to 65 °C to produce a turbid solution of $Mg(OCH_3)_2$. After 90 min of stirring at room temperature, carbon dioxide gas was bubbled through the $Mg(OCH_3)_2$ solution. A turbid solution of $MeOMgOCO_2Me$ had formed which was then centrifuged. The clear solution (~13 g of either 4.9 or 0.9 mass% solid content) was rinsed into a vial containing the pine wood template. Infiltration of the wood cells occurred in the same way as for the $CaCO_3$ replica during the drying process on a hotplate performed at 70 °C, as was shown in **Figure 17**. The infiltrated wood template was then kept in an oven at 80 °C for 7 h.

Magnesium silicate replicas

Magnesium silicate replicas were obtained using the methoxy magnesium methyl carbonate infiltrated templates which were further soaked once with a TEOS solution (1 g TEOS in 8 g EtOH). The infiltrated wood template was then kept in an oven at 80 °C for 7 h.

4.3 Calcination of infiltrated templates

4.3.1 Calcium carbonate and calcium oxide replicas

The infiltrated samples were dried and subsequently calcined at various temperatures (*e. g.* at 500 °C) for 2 h at a heating rate of 1 K · min^{-1}. Additional calcination experiments were performed at 200, 330 and 470 °C with 0.5 h of exposure time. Immediately after infiltration, hydrolysis of $Ca(OCOOCH_3)_2$ caused by residual moisture from the wood template occurred and a $CaCO_3$ sol was formed *in situ*. For calcination, the sample was transferred to a platinum crucible and placed in an oven, as is shown in **Figure 18**.

Figure 18. Photograph showing the platinum crucible holding the infiltrated template after placement in the oven for calcination.

4.3.2 Magnesium oxide and magnesium silicate replicas

Magnesium oxide replicas

To achieve MgO replicas, calcination was performed at various conditions, namely at 500 °C for 2 h and at 1450 °C for 5 h at a heating rate of 1 K · min^{-1} with holding steps of 0.5 h each at 200, 330 and 470 °C, respectively. Immediately after infiltration, hydrolysis of $MeOMgOCO_2Me$ caused by residual moisture from the wood template occurred and an $MgCO_3$ sol formed. A final magnesium oxide replica in a platinum crucible after calcination is shown in **Figure 19**.

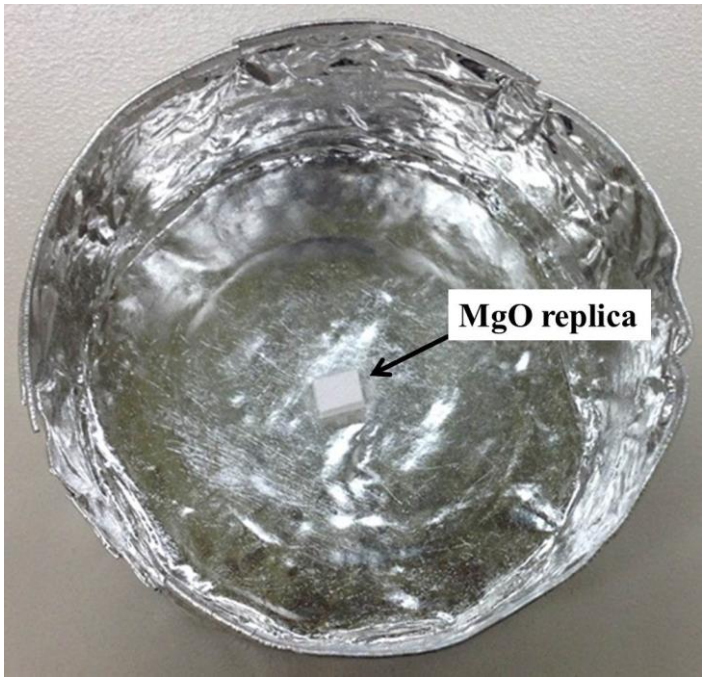

Figure 19. Photograph of a magnesium oxide replica sample in a platinum crucible obtained after calcination.

Magnesium silicate replicas

The magnesium silicate replicas were synthesized at a calcination temperature of 1350 °C for 5 h at a heating rate of 1 K · min^{-1}. Additional calcination experiments were performed at 200, 330 and 470 °C for 0.5 h each and at 600°C for 3 h.

The preparation process is summarized in **Figure 20**.

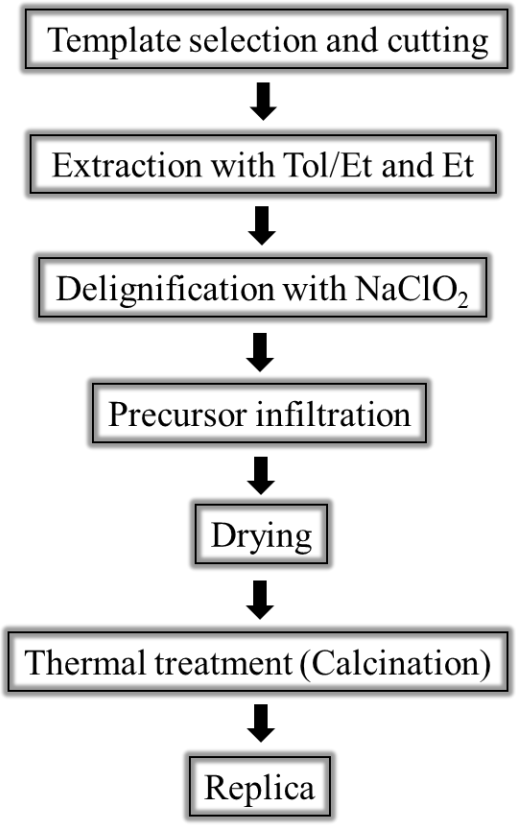

Figure 20. Steps taken in the preparation of the magnesium silicate replicas.

4.4 Analysis

4.4.1 Dynamic light scattering (DLS)

The absence of premature nanoparticle formation in the methoxy magnesium methylcarbonate precursor solution was tracked via dynamic light scattering (DLS) using a Zetasizer Nano ZS apparatus (Malvern Instruments, Workestershire, UK). The measurements were performed at 25 °C using methanol as solvent. The sample solution was transferred into a cuvette. All measurements were repeated three times whereby each time three values were recorded. Therefore, for each sample 9 values are reported.

4.4.2 Thermogravimetric analysis (TGA)

In order to find the appropriate calcination temperature where all cellulose was completely removed (complete combustion) from the replica, TGA was conducted using a NETZSCH STA409PC Luxx instrument equipped with a mass spectrometer. The measurement

was performed in air by using an Al_2O_3 pan as a sample holder. The samples were heated up to 1200 °C at a heating rate of 10 $K \cdot min^{-1}$.

4.4.3 X-ray diffraction (XRD)

The calcium carbonate polymorph and the magnesium oxide contained in the replica were identified via X-ray diffraction analysis (D8 advance instrument, Bruker AXS, Bruker, Karlsruhe, Germany). XRD patterns were collected in the range of 5-70° 2θ on an instrument with a Bragg-Brentano geometry and a Cu Kα source (30 kV, 35 mA).

4.4.4 Scanning electron microscopy (SEM)

SEM images of the products obtained from calcination were captured (without sputtering) using an XL30 ESEM FEG instrument (Philips/FEI Company, Eindhoven, The Netherlands). All measurements were performed under high vacuum with a secondary electron detector. The acceleration voltage varied in the range of 5-15 kV.

4.4.5 Energy dispersive X-ray (EDX) spectroscopy

EDX was performed on an XL30 ESEM FEG instrument (Philips/FEI Company, Eindhoven, The Netherlands) equipped with an energy-dispersive X-ray detector (EDX) for elemental analysis (New XL30, EDAX Inc., Mahwah, NJ, USA). The detector is a lithium-doped silicon (Si(Li)) crystal (EDAX instrument DETECTING UNIT PV7760/77-ME; Model: New XL-30 132-2.5 Port: EDS Active Area: 10 mm^2+ (Serial No. 9036-60770-ME), Amplifier Model: 194 (Serial No.: n/a SUTW 3.3)).

4.4.6 ^{29}Si MAS NMR spectroscopy

Solid state ^{29}Si MAS NMR measurements were conducted on a Bruker Advance 300 MHz (7.0455 T) instrument. The sample was siffed into a 7 mm ZrO_2 rotor at a spinning frequency of 5 kHz, a magic angle of 54°44' (MAS), resonance frequency 59.63 MHz for ^{29}Si and pulse 6 millisec., single pulse measurement with repetition time D1 - 45 s, 1200 - 1800 scans. Tetrakis(trimethylsiloxy)silane (TMS) was used as external standard.

4.4.7 Specific surface area (BET)

The specific surface area (BET method, N_2) was measured on a Nova 4000e instrument from Quantachrome (Boynton Beach, FL, USA) utilizing a replica sample degassed for 2 h at 200 ° C.

4.4.8 Infrared spectroscopy (IR)

Infrared spectra were recorded on a Vertex 70 FT-IR spectrometer (Bruker Optik GmbH, Ettlingen, Germany) equipped with a diamond ATR cell.

4.4.9 Compressive strength tests

Mechanical testing was carried out in plate-plate compression geometry adapted from DIN/EN/ISO-844 on a smarTens010 universal testing machine (Karg Industrietechnik, Krailing, Germany). The plate size was reduced to 4 cm^2 to account for the small sample sizes of the templates. Each measurement was repeated three times and the values reported for the compressive strength represent the average.

5 Methods

5.1 Dynamic light scattering (DLS)

Dynamic light scattering (DLS) is a spectroscopic method used to determine the size distribution of particles such as polymers, proteins, colloids, etc. which are in solution or suspension. This method is also known as photon correlation spectroscopy (PCS) or quasi-elastic light scattering (QLS) [83]. The principle of light scattering involves that light from a laser passes through a polarizer which defines the polarization of the incedent beam and then impinges on the scattering medium. Then the scattered light passes through an analyzer which selects a given polarization and enters a detector, as is illustrated in **Figure 21** [84]. The scattering angle θ is the angle between the incident beam and the detector.

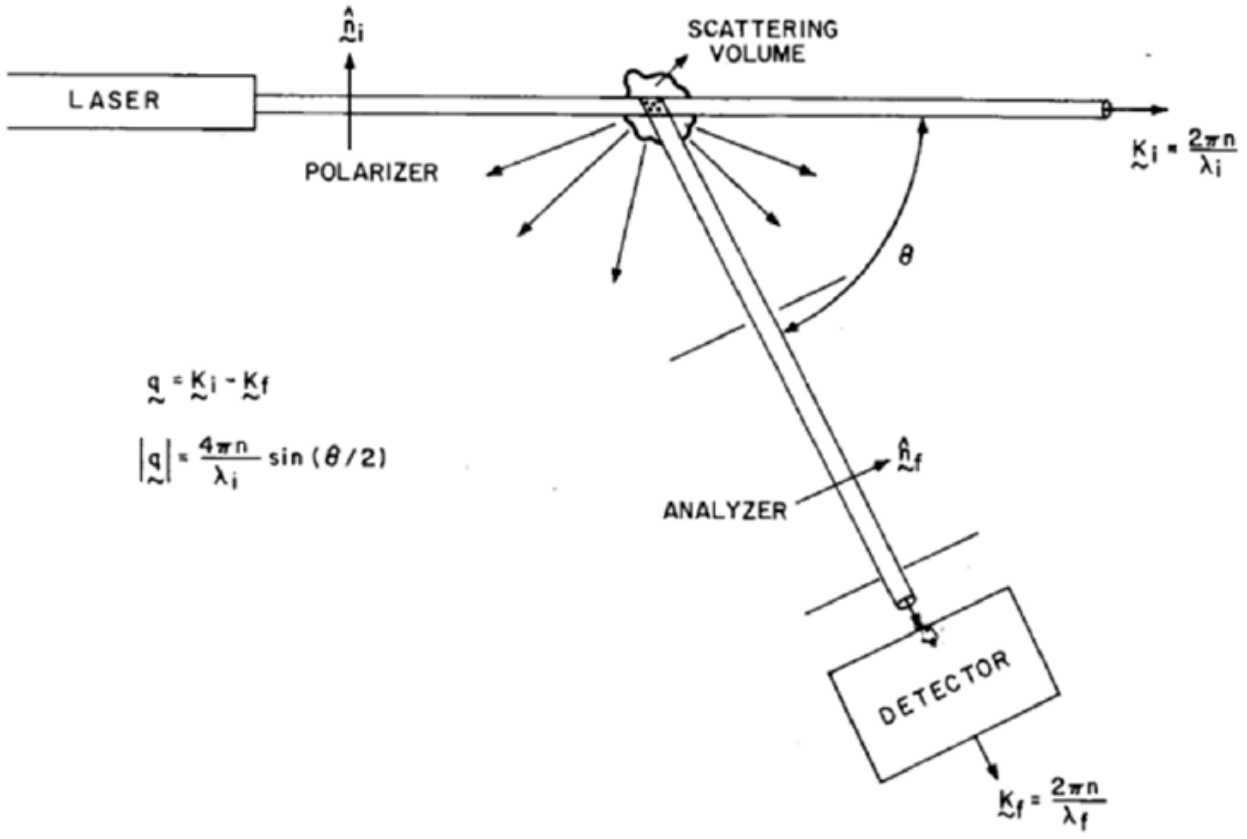

Figure 21. Schematic representation of the set-up in a light-scattering instrument (after [84]).

The diffusion coefficient *D* depends on the particle diameter *d* as is shown in **Equation 24**.

$$D = \frac{k_B T}{3\pi\eta d} \qquad \textbf{Equation (24)}$$

where

T is the temperature,

k_B is Boltzmann's constant,

η is the viscosity of the background fluid [83].

In the experiment, the incident light will be scattered by the small particles present in the solution. According to Brownian motion, these fine particles in the solution are in constant random movement and will diffuse at a speed related to their size; smaller particles diffuse faster than larger ones [83, 84]. The size distribution can be acquired via the software program of the DLS instrument [85]. In our experiments, the DLS measurements confirmed that no sol particles were present in the $MeOMgOCO_2Me$ precursor solution prior to infiltration (**Figure 22**). However, when a small amount of water was added to the $MeOMgOCO_2Me$ solution, immediately small particles in the range of 0.6 – 11 nm were found (**Figure 23**).

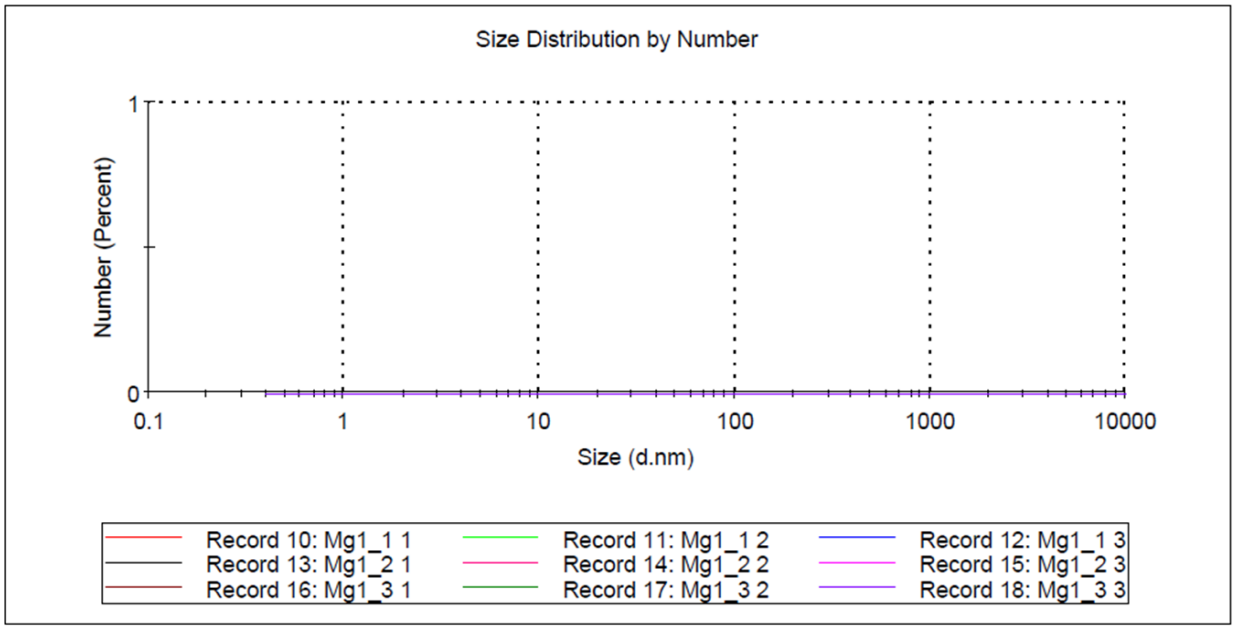

Figure 22. Particle size measurement for the $Mg(OCOOCH_3)(OCH_3)$ solution after 1 h of storage on air, measured on the Zetasizer instrument. The measurement was repeated three times whereby each measurement provided three values.

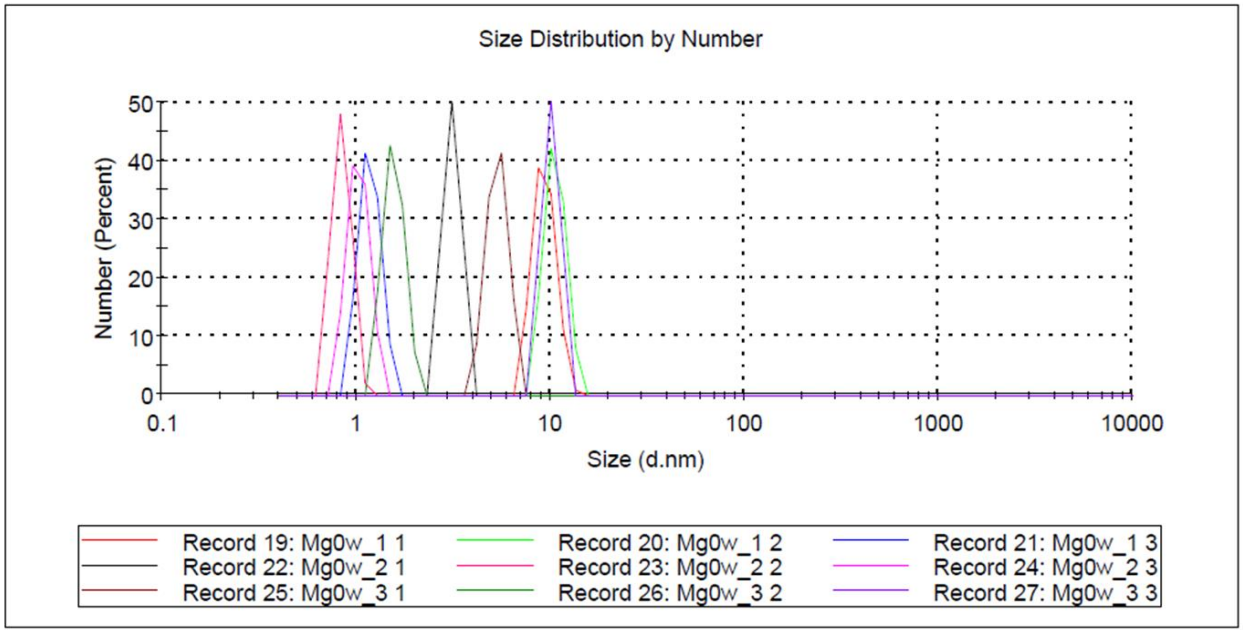

Figure 23. Particle size distribution of the $Mg(OCOOCH_3)(OCH_3)$ solution after water had been added, as measured on the Zetasizer instrument. The measurement was repeated three times yielding three values for each measurement.

5.2 Thermogravimetric analysis (TGA)

Thermal analysis is a method based on the physical properties of materials such as decomposition and melting points or desorption of substances and their reaction products which is temperature-dependent. The sample will be processed following a temperature program. Pure substances as well as mixtures of substances can be measured. The thermograms obtained are useful not only in quality control, but also in the study of diverse materials including metals, alloys, polymers and minerals and natural products [86].

The thermogravimetric analysis (TGA) measures the change of mass as a function of temperature. The exact weight of the sample is determined before and during the entire measurement. A high precision balance and a furnace for heating are needed for this analysis. Inside the sample chamber inert gas or a reactive atmosphere can be applied [86].

This technique was utilized in this study in order to identify the appropriate calcination temperature where all cellulose is completely removed (complete combustion) from the replica.

In a typical experiment, a sample of $Mg(OCO_2CH_3)(OCH_3)$-infiltrated pine wood was measured on a TGA instrument equipped with a mass spectrometer (TGA-MS), as is shown in **Figure 24**. The mass loss owed to the combustion shows that the removal is complete at a temperature around 540 ºC. The residual mass 18 which is H_2O decomposed at 100 ºC which presents the boiling point of water and at 310 ºC which is assigned to water from inside the wood template. All three residual masses at 12 (C), 18 (H_2O) and 44 (CO_2) are completely decomposed at 540 ºC (**Figure 25**). The residual mass 28 which is CO is decomposed at 320 ºC (**Figure 26**).

The mass loss from combustion shown in the TGA curve confirms that the combustion of the delignified, non-infiltrated pine wood is complete at a temperature around 530 °C (**Figure 27**). This temperature varies for different samples infiltrated with different inorganic precursors. The combustion temperatures studied here were 500, 540 and 550 °C for $Ca(OCOOCH_3)_2$-, $Mg(OCOOCH_3)(OCH_3)$- and $Si(OC_2H_5)_4$-infiltrated pine wood, respectively (**Figure 27**).

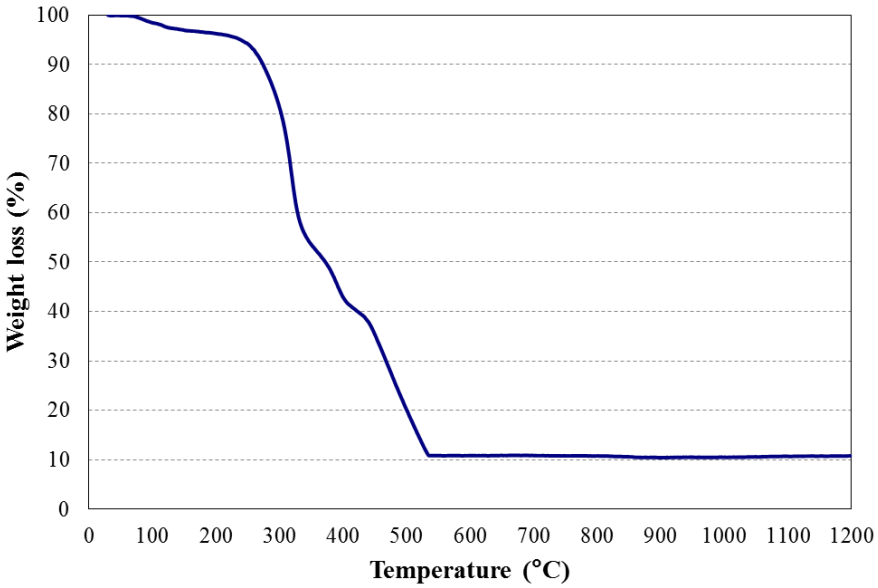

Figure 24. TGA curve of a pine wood sample infiltrated once with a $Mg(OCOOCH_3)(OCH_3)$ solution (solid content = 0.9 wt.%).

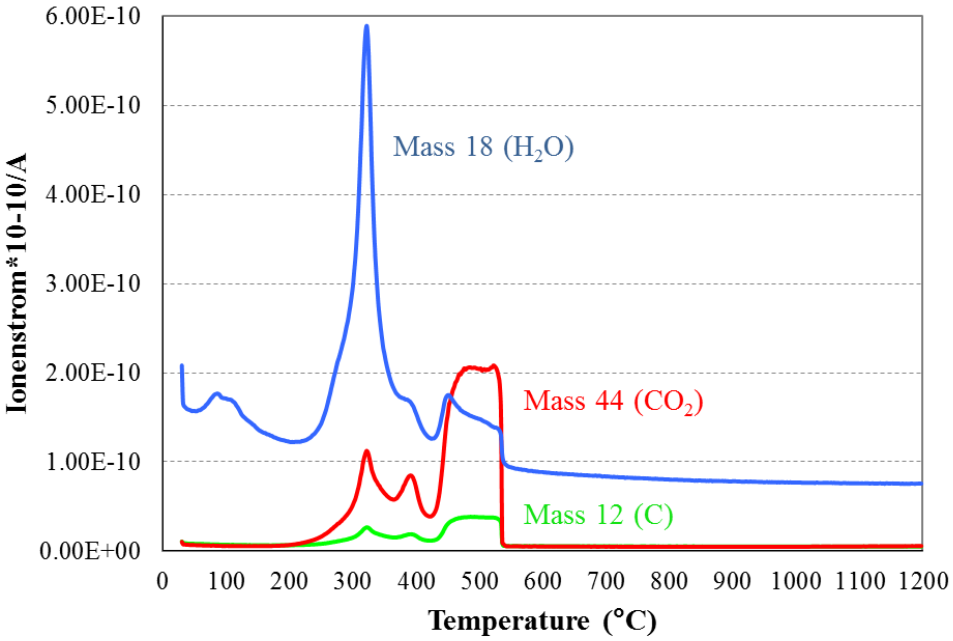

Figure 25. Mass spectra from TGA-MS measurements of the pine wood sample infiltrated once with a $Mg(OCOOCH_3)(OCH_3)$ solution (solid content = 0.9 wt.%) at m/z = 12 (green line), 18 (blue line) and 44 (red line) corresponding to C, H_2O and CO_2 respectively.

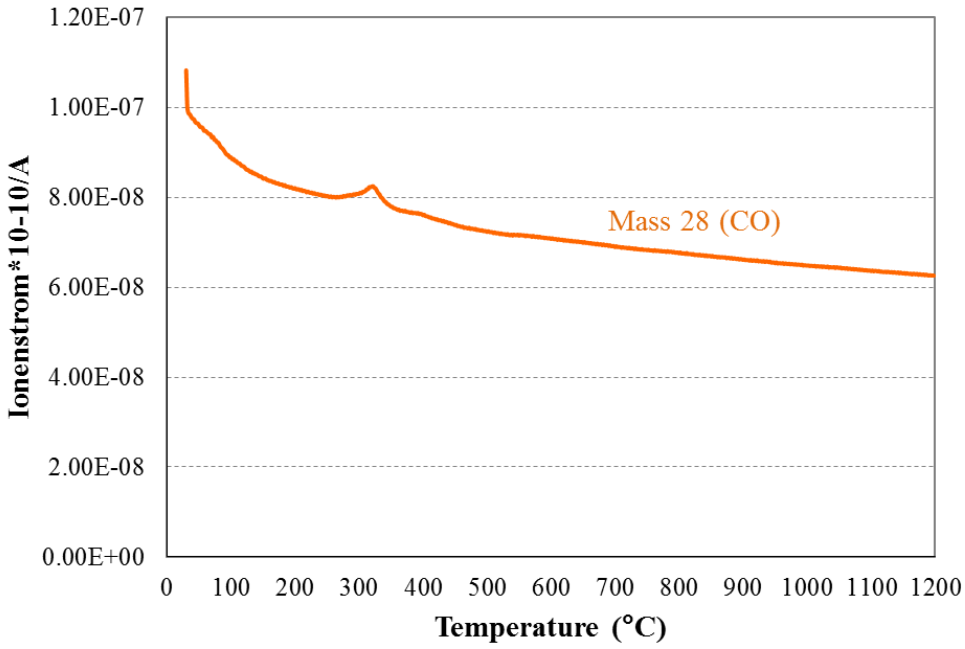

Figure 26. Mass spectrum from TGA-MS measurement of the pine wood sample infiltrated once with a $Mg(OCOOCH_3)(OCH_3)$ solution (solid content = 0.9 wt.%) at m/z = 28 corresponding to CO.

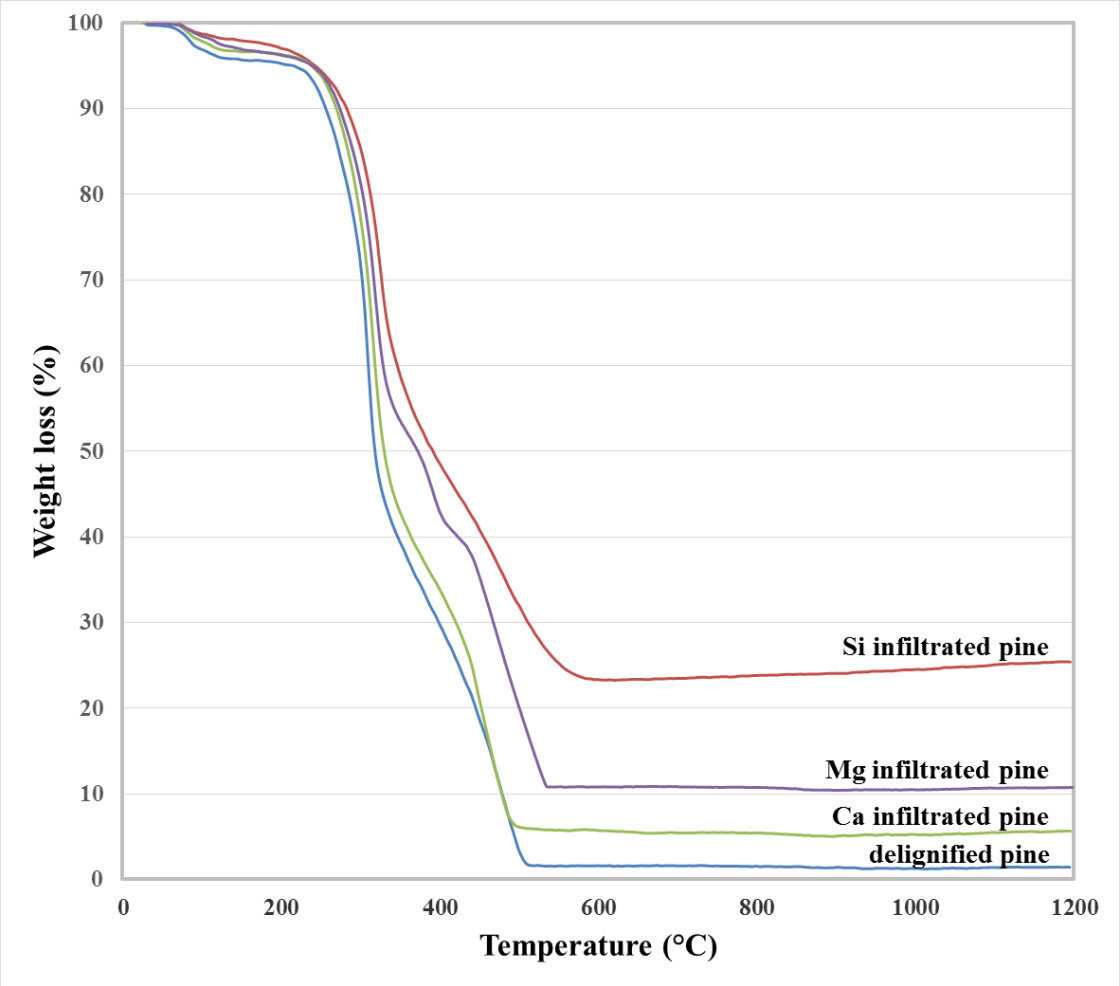

Figure 27. TGA curves of a delignified pine wood sample infiltrated with $Ca(OCOOCH_3)_2$-, $Mg(OCOOCH_3)(OCH_3)$- and $Si(OC_2H_5)_4$-precursors.

5.3 X-ray diffraction (XRD)

XRD is a method which is widely used to identify bulk phases. Due to the low wavelengths of X-rays which are in the Angstrom range (0.2 – 20 Å) [86], it has sufficient energy to penetrate solids, so it is suitable to analyse the solids' internal structures [87].

X-ray is produced from bombarding a metal target with high energy electrons. In an x-ray tube, a cathode and an anode are present, as is illustrated in **Figure 28**. At the cathode, heavy elements such as tungsten (W) are heated to generate electrons called primary electrons.

These electrons are accelerated by the high voltage (60-80 kV) between cathode and anode, and then hit the metal target (usually Cu) and the anode [86]. The emitted X-rays originate from two processes; 1) primary electrons slowed down by the target emit a continuous background spectrum of braking radiation or deceleration radiation (Bremsstrahlung), 2) a primary electron hits a shell electron in the metal target, for example the primary electron hits the K shell electron of Cu and creates a core hole in the K shell (**Figure 29**) which is then filled by an electron from the L shell and emits an X-ray quantum with an enery of 8.04 keV ($\Delta E = E_K - E_{LIII}$ = (8.973 – 0.933) keV) called K_α. When the electron-hole in the K shell is filled with an electron from the M shell, the radiation is called K_β. This process is called X-ray fluorescence [87]. The radiation leaves the X-ray tube through a Be window which is transparent to X-ray [86] (**Figure 28**).

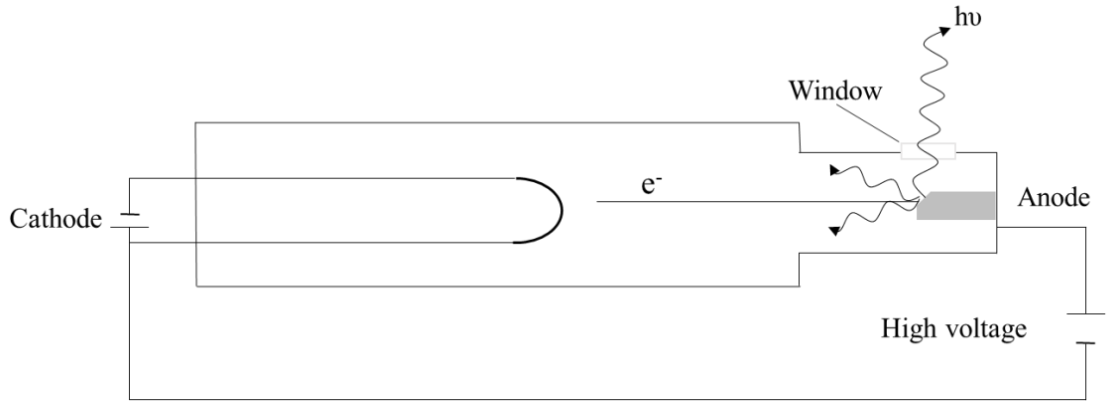

Figure 28. Schematic illustration of the set-up of an X-ray tube (from [86]).

X-ray diffraction involves the elastic scattering of X-ray photons by atoms arranged in a periodic lattice. This analysis is useful to indentify crystal structures depending on the interference principle [86]. When X-ray waves interact with atoms in crystals, X-ray interference will occur. Crystal structures contain planes of atoms and each plane will reflect the incident X-ray beam differently. In **Figure 30**, two rays are reflected from two planes. Beam 1 reflects already at the top atomic plane, while beam 2 penetrates deeper into the structure and reflects from the second atomic plane. Therefore beam 2 travels farther than beam 1, at a different distance of $2d \cdot \sin\Theta$. When this path differential $2d \cdot \sin\Theta$ is equal to any integer n of the wavelength of the two beams, the reflection of these two waves which emerge from the crystal

will be in phase interference and cause constructive interference, thus yielding a higher amplitude wave [86, 87].

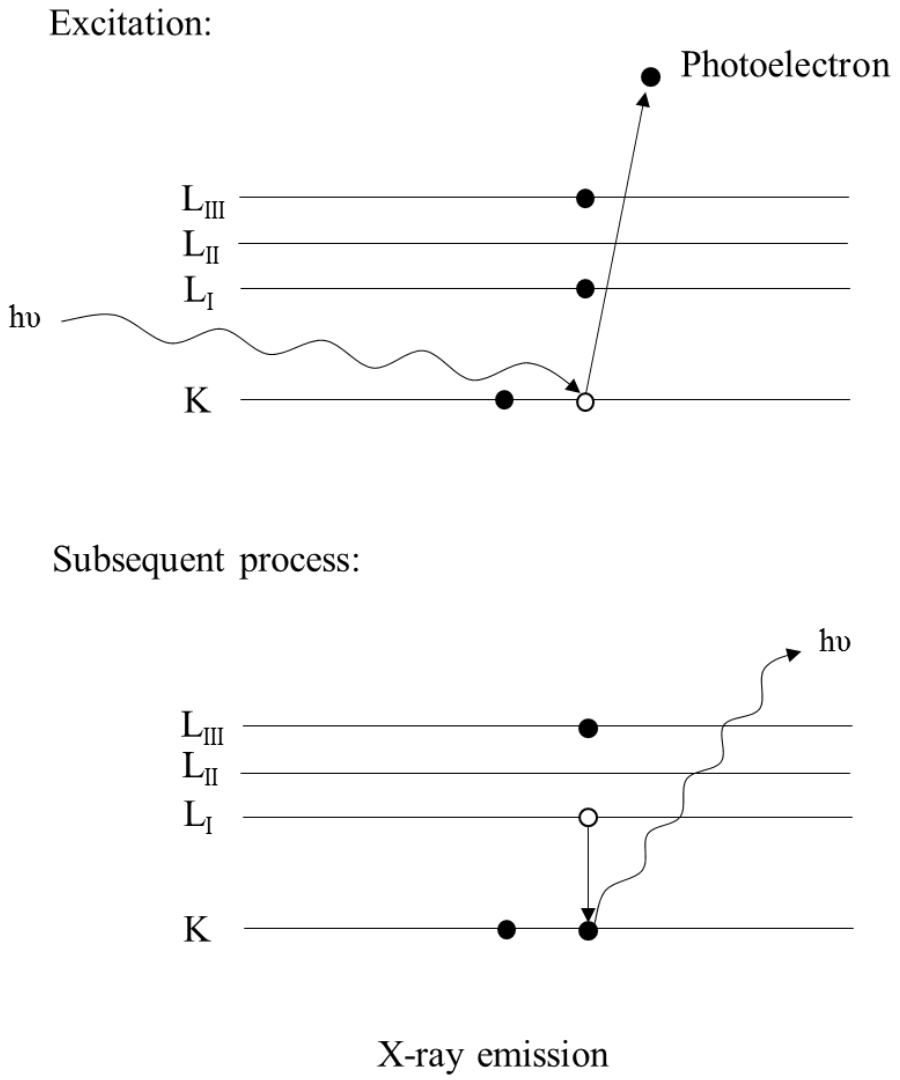

Figure 29. Excitation mechanism as occuring in X-ray spectroscopy (● = electron, ○ = hole) (from [86]).

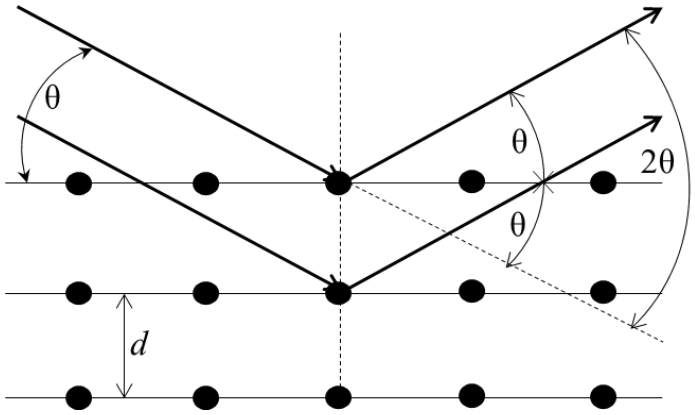

Figure 30. Wave interference occurring from reflection of beams at different planes existing in the analyzed crystal (from [86]).

From **Figure 30**, the lattice spacing can be derived based on the diffraction of the X-rays by the crystal planes, as expressed in the Bragg equation [87]:

$$n \cdot \lambda = 2d \cdot \sin\Theta \quad ; \quad n = 1, 2, \ldots \qquad \textbf{Equation (25)}$$

where

- λ is the wavelength of the X-rays
- d is the distance between two lattice planes
- Θ is the angle between the incoming X-rays and the normal to the reflecting lattice plane
- n is the integer called order of the reflection.

During measurement, the X-ray source stays stationary while the detector is moving. The XRD pattern of a powdered sample is measured by scanning the intensity of the diffracted radiation as a function of the angle 2Θ between the incoming and the diffracted beams (**Figure 31**). As λ is constant for the same X-ray source, therefore, from the Bragg's equation, only the proper angle which relates to the incoming beam will give constructive interference. Then this equation can be solved to obtain the lattice spacing which is characteristic for a specific compound [86].

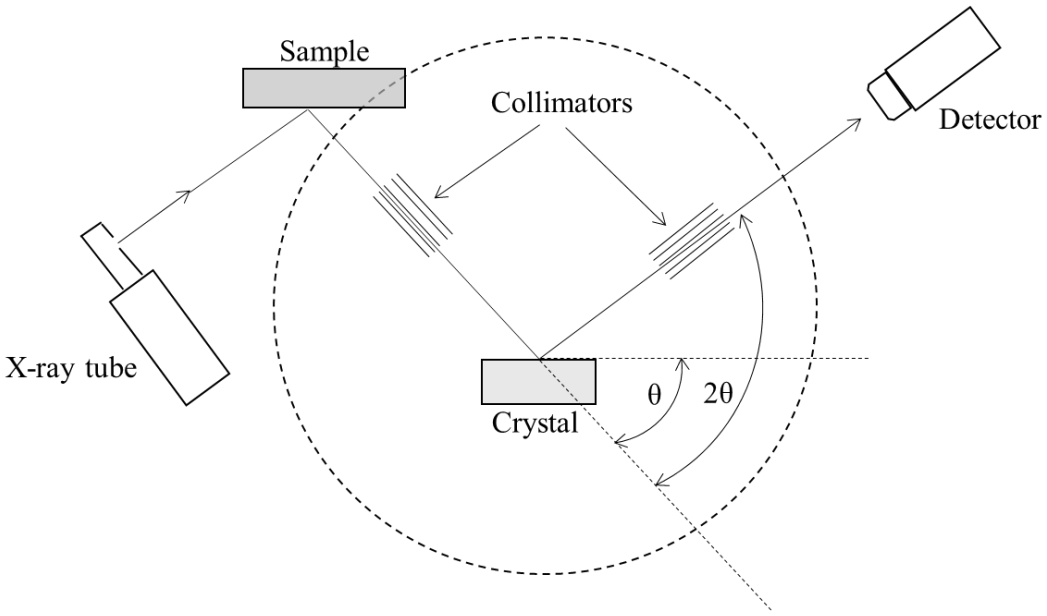

Figure 31. Schematic of the detector of an X-ray diffractometer (from [86]).

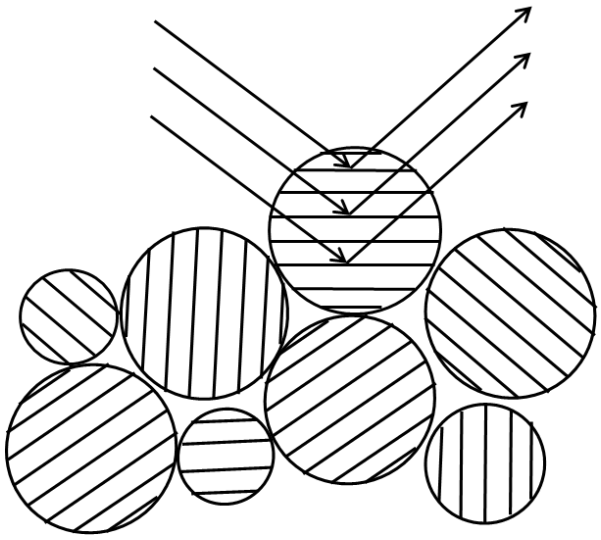

Figure 32. X-ray scattered by atoms contained in powder particles and arranged in an ordered lattice interfere constructively in the directions given by Bragg's law (from [87]).

When working with powdered samples, the diffraction pattern is formed by the small fraction caused by the particles, because the powder particles are oriented randomly, and only a small fraction of these powder particles are oriented by chance at a certain crystal plane

which is at the right angle Θ with the incident beam for constructive interference (**Figure 32**). For this reason, rotation of the sample during measurement is the solution to enhance the number of particles that contribute to the diffraction [87].

5.4 Scanning electron microscopy (SEM)

When the primary electron beam interacts with the sample in an electron microscope, it leads to a number of detectable signals as is shown in **Figure 33**. Scanning electron microscopic images are accomplished by scanning a narrow electron beam over the surface of the sample and detecting either secondary or backscattered electrons. Their yield is a function of the position of the primary electron beam. Using SEM provides information about particle sizes and the form and arrangement of the particles (morphology) [4]. Since electrons have characteristic wavelengths of less than an Angstrom, they come close to identifying atomic details [87].

Secondary electrons are emitted from the sample surface due to inelastic collisions between primary electrons and the sample. They mostly have low energies in the range of around 5 – 50 eV. In SEM instruments using a secondary electron detector, the contrast on the SEM image is caused by the orientation: parts of the surface facing the detector appear brighter than parts of the surface which are away from the detector. SEM instruments with a backscattered electron detector can provide information on the composition of the sample because heavy elements scatter more efficiently, yielding brighter images [87]. Since an SEM equipped with a secondary electron detector recognizes the contrast due to the topology of a surface, it presented a suitable technique to investigate the quality of the replicas in this study.

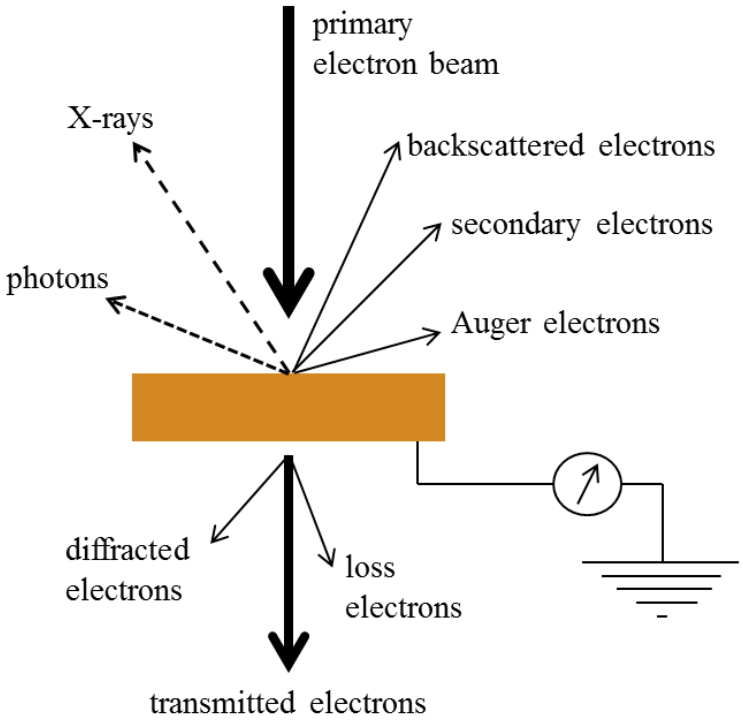

Figure 33. Interaction between the primary electron beam and the sample in a scanning electron microscope (from [87]).

5.5 Energy dispersive X-ray (EDX) spectroscopy

X-rays are one of the byproducts in an electron microscope as is illustrated in **Figure 33**. They are emitted from the material, which is bombarded with electrons. This phenomenon can be explained by quantum mechanics. The interaction between an electron and an atom leads to two types of X-ray: 1) Characteristic emission lines and 2) Braking radiation [87].

X-rays characteristic for elements are emitted when an electron from a higher shell fills an initial hole generated by ejection of a bound electron from an atomic orbital by the incident electron. For example, a K_α X-ray photon is emitted when the K shell hole is filled with an electron form the L_{III} or L_{II} shell (**Figure 34**). The energy of an X-ray photon is characteristic for each emitting atom [87].

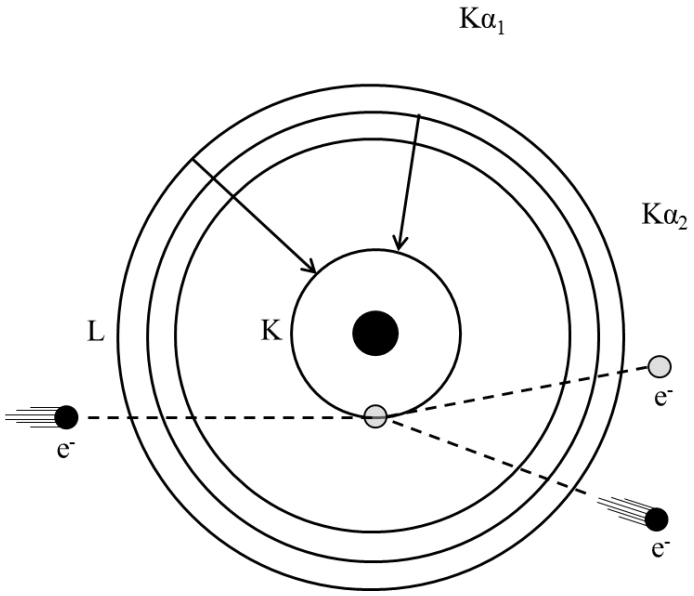

Figure 34. X-ray fluorescence: A core hole is filled up by an electron from a higher shell, the energy gained is used to emit an X-ray photon (from [87]).

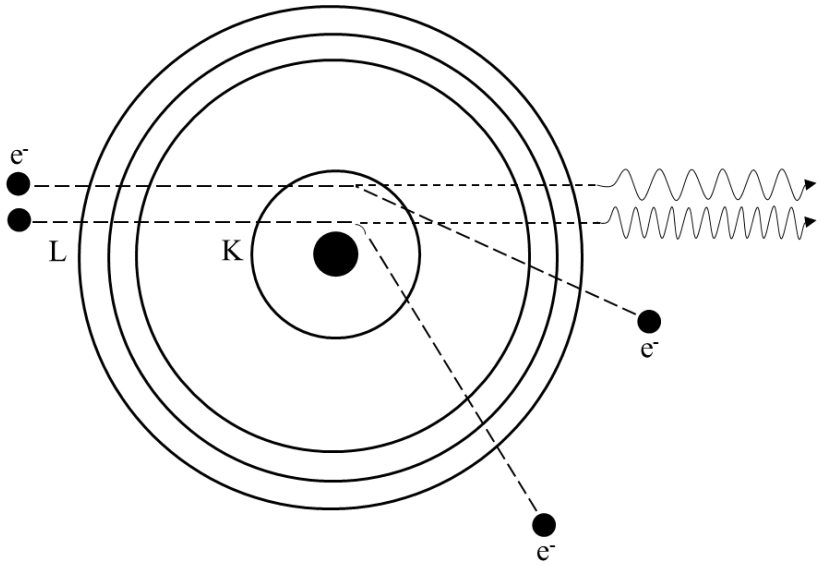

Figure 35. X-ray fluorescence: Braking radiation is emitted when an electron is accelerated in the attractive force field of the positively charged nucleus (from [87]).

Braking radiation which gives a structureless continuum background in the X-ray spectrum is emitted during the acceleration of an electron in the attractive force field of the positively charged nucleus. The distance between the electron and the nucleus effects the hyperbolic curvature path which the electron follws (**Figure 35**) [87].

Based on X-ray fluorescence produced in an SEM, the elemental composition of a sample can be dertemined when the SEM is equipped with an energy dispersive X-ray detector. A most common type of this detector is a liquid-nitrogen cooled solid-state device which constitutes a lithium-doped silicon semiconductor [86, 87]. This Si(Li) detector consists of p-type silicon compensated by lithium in order to increase its electrical resistivity. When incident X-ray photons pass through this detector, they will interact to produce a specific number of electron hole pairs [88]. The bias voltage is used to sweep the charge produced from the diode to a charge-sensitive pre-amplifier. After that, a charge loop intergrates the charge on a capacitor to produce a voltage pulse which is proportional to the incident X-ray photon energy. The arriving pulses are sorted by a multichannel analyzer and the spectrum will be in the form of the X-ray energy spectrum [88]. As an example, an EDX spectrum of a magnesium silicate replica is presented in **Figure 36**.

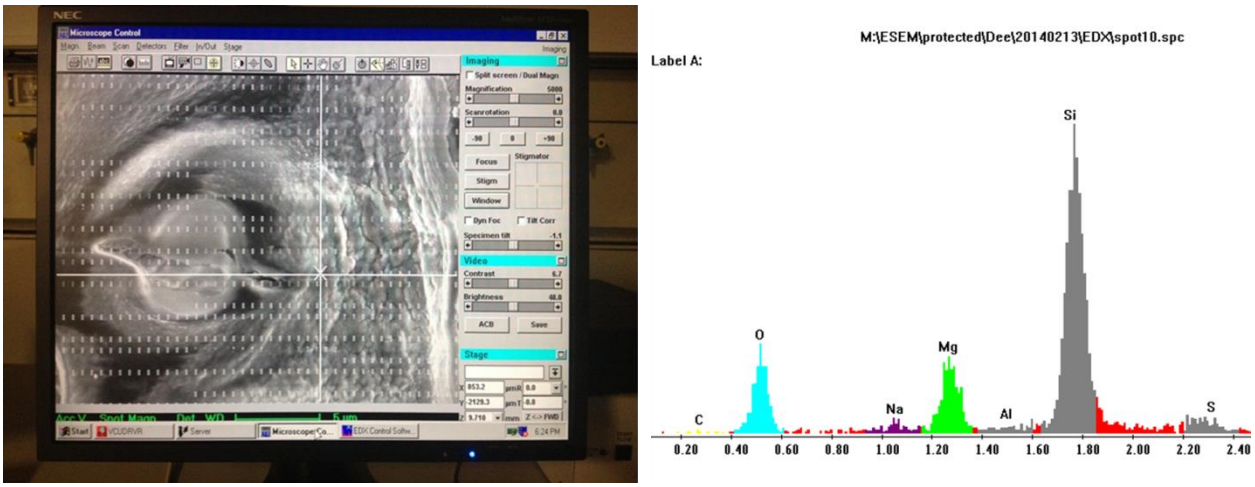

Figure 36. EDX spectrum of a magnesium silicate replica, measured at a spot near a pit-hole structure of the replica which is shown on the left side.

5.6 ^{29}Si MAS NMR spectroscopy

Solid state NMR spectroscopy is useful to gain insight into the structure of many materials. Most nuclei possess a nuclear or intrinsic angular momentum, P. The atomic nucleus is assumed to be spherically rotating about an axis. This angular momentum is quantified [89].

$$P = \sqrt{I(I+1)}\hbar \qquad \textbf{Equation (26)}$$

Where

$\hbar = h/2\pi$, h is Planck's constant (= 6.6256 x 10^{-34} J s), and

I is the angular momentum quantum number, usually called the nuclear spin [89].

The angular momentum, P, is proportional to a magnetic moment, μ. Both are vectorial parameters.

$$\mu = \gamma P \qquad \textbf{Equation (27)}$$

where, γ is called the magnetogyric ratio which is a constant for each nuclide (e.g. each isotope of each element). The detection sensitivity of a nuclide in an NMR experiment depends on this γ. The larger the value of γ is, the more sensitive is the nuclide (easier to observe) [89].

By combining **Equations (26)** and **(27)**, the magnetic moment, μ can be calculated as:

$$\mu = \gamma\sqrt{I(I+1)}\hbar \qquad \textbf{Equation (28)}$$

Therefore, nuclides with a spin I = 0 have no nuclear magnetic moment [89].

When a nucleus with angular momentum, P, and magnetic moment, μ is placed in a static magnetic field B_0, the angular momentum takes up an orientation such that its component P_z along the direction of the field is:

$$P_z = m\hbar \qquad \textbf{Equation (29)}$$

where m is the magnetic or directional quantum number; m = I, I-1,…-I. For the isotope with I = 1/2, this results in two m values (+ 1/2 and -1/2), see **Figure 37**.

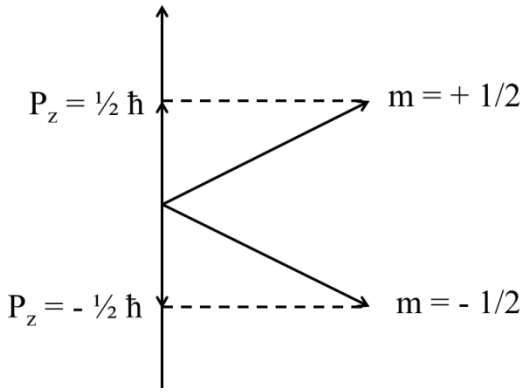

Figure 37. Directional quantification of the angular momentum P in the magnetic field for nuclei with I = ½ (from [89]).

From **Equations (27)** and **(29)**, the magnetic moment along the field direction Z is:

$$\mu_z = m\gamma\hbar \qquad \textbf{Equation (30)}$$

In classical presentation, the precession nuclear dipoles around the z axis (which is the direction of the magnetic field) is similar to that of a spinning top (**Figure 38**). The precession frequency, or Larmor frequency υ_L, is proportional to the magnetic flux density B_0:

$$\upsilon_L = |\gamma/2\pi|B_0 \qquad \textbf{Equation (31)}$$

Because of the directional quantization (in contrast to the classical spinning top), only certain angles are allowed for a precessing nuclear dipole such as at 54°44′ for the proton with I = 1/2 [89].

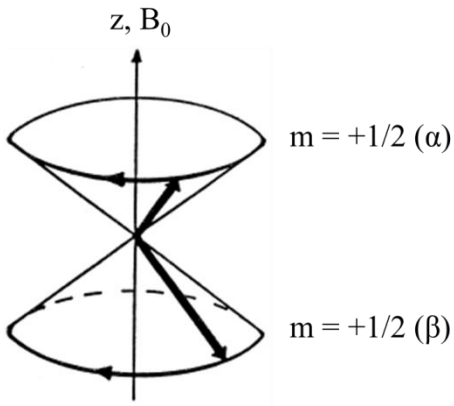

Figure 38. Precession of nuclear dipoles with spin I = 1/2 around a double cone; the half-angle of the cone is 54°44′ (from [89]).

The NMR technique depends on the principle that when a sample placed in an applied magnetic field, B_0, then the energy level of the nuclear spin is split into different energy levels called degeneracy resulting from Zeeman interaction. A nucleus of spin quantum number I will have 2I + 1 possible orientations in a magnetic field, so there are 2I + 1 energy levels which are designated by the magnetic quantum number, m_I, such that m_I = I, I-1,…, -I. The spaces between each energy level are equal, therefore there are 2I transitions with the same energy corresponding to a frequency, υ_0 in Hz (or ω_0 in rad s^{-1}), termed the Larmor frequency [90].

^{29}Si is the only NMR-active isotope of silicon with I = 1/2, therefore its nuclear spin splits into 2 degeneracies with magnetic quantum numbers m_I = 1/2 and -1/2 [89], as is shown in **Figure 39**.

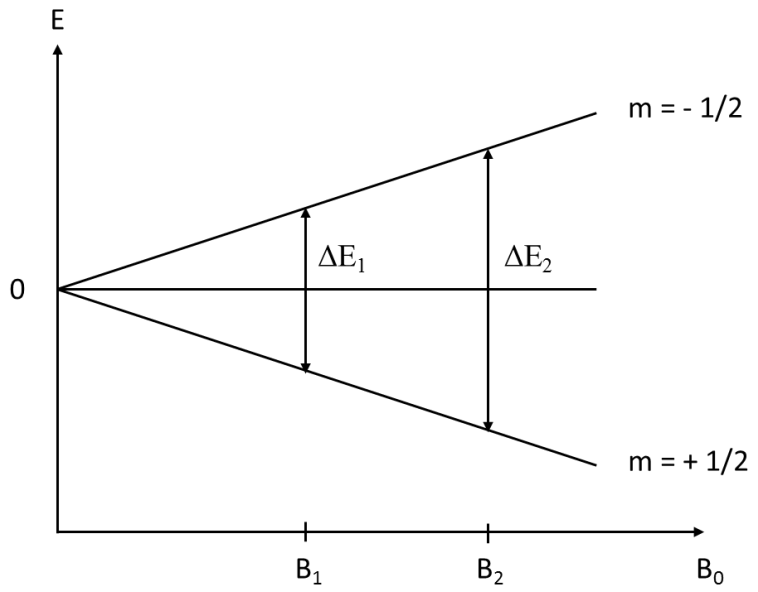

Figure 39. The energy difference ΔE between two adjacent energy levels in an atom as a function of the magnetic flux density, B_0 (from [89]).

The presence of a local magnetic field generated by surrounding electrons causes a chemical shielding interaction which changes the total magnetic field experienced by the nucleus. This small change in the magnetic field slightly perturbs the resonant frequency of the nucleus from the basic Larmor frequency. This perturbation provides the basis of NMR as an analytical method, because nuclei in different chemical environments lead to different degrees of perturbation from the Larmor frequency, thus enable their discrimination in an NMR spectrum [90].

Forsterite, α-Mg_2SiO_4, is an analogue of olivine ($Mg_{1.8}Fe_{0.2}SiO_4$). The crystal structure of forsterite (space group P_{nma}) composes of SiO_4^{4-} units that are linked through Mg^{2+} ions in octahedral coordination with oxygen as is shown in **Figure 40**. The structure contains a single Si site, two crystallographically distinct magnesium sites and three crystallographically distinct oxygen sites [90].

The isotropic chemical shift of forsterite which has been evaluated using magic angle spinning (MAS) yields a value of -62 ppm which is typical for Q^0 Si species [90-92]. The

superscript refers to the number of bridging oxygens coordinated to the Si atom, so the superscript "0" reflects an isolated SiO_4 tetrahedra (mono silicate) in the structure [90].

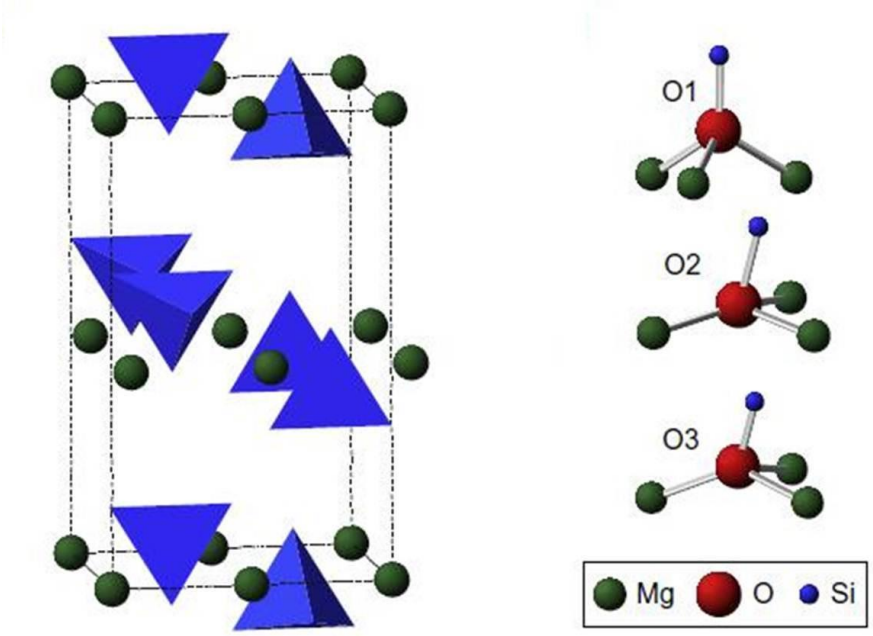

Figure 40. (Left) Crystal structure and (right) oxygen coordination environments for forsterite, α-Mg_2SiO_4·SiO_n. Polyhedra are shown in blue, Mg atoms in green and O in red (from [90]).

5.7 Specific surface area (BET)

The BET method mostly uses N_2 adsorption and desorption to investigate the specific surface area and distributions of pore radii in a material.

In a Langmuir isotherm it is assumed that adsorption is restricted to a monolayer coverage, and that adsorption is localized. However, due to the van der Waals forces, physical adsorption can also lead to multiple adsorbed layers (**Figure 41**). Therefore the assumption of a single monolayer is unrealistic in many cases. Brunauer, Emmet and Teller (BET) modified the Langmuir approach by balancing the rates of adsorption and desorption for the various molecular layers. In the BET model, it is assumed that adsorption in the first monolayer produces a characteristic heat of adsorption ΔH_A, while the subsequent layers are controlled by the heat of

condensation of the vapor, ΔH_L [93]. The most common linearized form of the final BET equation is:

$$\frac{p}{V(p_0-p)} = \frac{1}{V_m c} + \frac{(c-1)p}{V_m c p_0} \qquad \textbf{Equation (32)}$$

Where

V is the volume of adsorbed vapor at standard temperature and pressure (STP): at 273.15 K, 1 atm,

V_m is the monolayer capacity at STP,

p is the partial pressure of the adsorbate,

p_0 is the saturation vapor pressure of the adsorbate, and

$$c \approx \exp \frac{(\Delta H_A - \Delta H_L)}{RT} \qquad \textbf{Equation (33)}$$

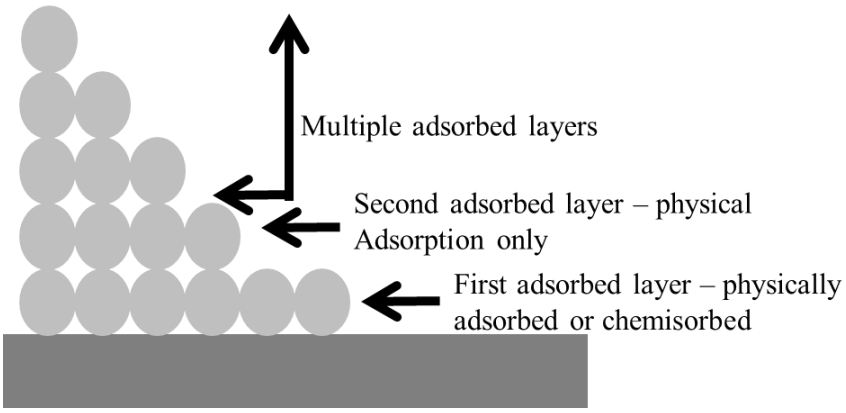

Figure 41. In multilayer sorption on a solid surface, the first layer may be physically adsorbed or chemisorbed. Subsequent layers will always be physically adsorbed (from [93]).

The BET isotherm is commonly used to determine the surface area of finely divided solids by physical adsorption. This technique produces useful results when the pressure,

p, is between 0.05 p_0 and 0.35 p_0 [93]. However, for porous solids which show an adsorption hysteresis, V_m cannot be accurately dertermined. From **Equation (32)**, a plot of $\frac{p}{V(p_0-p)}$ versus $\frac{p}{p_0}$ should be linear over the pressure region of 0.05 - 0.35 p_0, the slope of the line, S = $\frac{(c-1)}{V_m c}$, and the intercept, I = $\frac{1}{V_m c}$. Therefore the monolayer capacity, V_m of the solid and its specific area, A_s can be calculated as follows [93]:

$$V_m = \frac{1}{S+I} \qquad \textbf{Equation (34)}$$

$$A^s = \frac{V_m k}{sample\ weight} \qquad \textbf{Equation (35)}$$

$$k = \frac{N_a A}{M_V} \qquad \textbf{Equation (36)}$$

where

N_a is Avogadro's number,

A is the area per molecule of the adsorbed gas, and

M_v is the gram molecular volume of gas (22.400 L at STP).

The most common adsorbate used to determine the BET surface area is nitrogen, N_2, which has an effective area per molecule, A, of 0.162 nm^2 at the temperature of liquid nitrogen (77K) [93]. The specific surface area and pore size distributions are investigated by using N_2 adsorption and desorption. Using this technique, only pores which are accessible for N_2 are detected. Falsification of the values for the pore radii may be found when structural changes are induced by the N_2 pressure during the measurement [4].

5.8 Infrared spectroscopy (IR)

Infrared spectroscopy presents a vibration spectroscopy. The vibration in molecules or in solid lattices is excited by the absorption of photons. Infrared radiation is classified into three categories: far, mid and near infrared. Mid infrared is the most interesting

one [87]. The wavelengths in this mid IR region is between 2.5 x 10^{-4} cm and 25 x 10^{-4} cm which correspond to energies of about 4.6 to 46 kJ/mol (1.1 to 11 kcal/mol) [94]. Infrared photons do not have enough energy to cause electronic transition, but they cause groups of atoms to vibrate depending on the bonds that connect them. Similar to electronic transitions, these vibrational transitions correspond to distinct energies, and molecules absorb infrared radiation only at certain wavelenths and frequencies [94].

Every molecule possesses discrete levels of vibrational energy. Absorption of photons with frequencies υ in the mid-infrared range leads to transitions between vibrational levels [87]. The corresponding vibrational energy levels are as shown in **Equation 38**:

$$E_n = \left(n + \frac{1}{2} \right) h\upsilon \qquad \textbf{Equation (37)}$$

$$\upsilon = \frac{1}{2\pi} \sqrt{\frac{k}{\mu}} \qquad \textbf{Equation (38)}$$

$$\frac{1}{\mu} = \frac{1}{m_1} + \frac{1}{m_2} \quad \text{or} \quad \mu = \frac{m_1 m_2}{m_1 + m_2} \qquad \textbf{Equation (39)}$$

where

- E_n is the energy of the n^{th} vibrational level
- n is an integer
- h is Planck's constant
- υ is the frequency of the vibration
- k is the force constant of the bond
- μ is the reduced mass
- m_i is the mass of the vibrating atoms.

Therefore, vibrational frequencies increase with increasing bond strength, and with decreasing mass of the vibrating atoms [87].

According to the vibrational selection rule, transitions are allowed when the vibrational quantum number changes by one unit, and the dipole moment of the molecule must change during the vibration [87].

The attenuated total reflection (ATR) technique is an alternative sampling technique that is based on reflection of the light source off the surface of the sample. With this technique, solids including powders and plastic films etc. and liquids can be determined directly without the need for further preparation. As is illustrated in **Figure 42**, the sample is placed on a crystal with direct contact. The crystal used in ATR has a high reflective index such as diamond (often used), zinc selenide or germanium [95]. The measurement principle is that the beam of infrared light is passed through the crystal in such a way that it is reflected at least once off the internal surface in contact with the sample. The beam will penetrate into the sample which has a lower reflective index than the crystal. The radiation penetrates the sample to a depth of about 20 µm and may be absorbed by it [96]. The material that is in close contact with the reflecting surface will absorb radiation selectively, leaving the beam with lower energy at the wavelength where the material absorbs [95, 97]. The absorption spectra which are characteristic of the sample will be obtained by measuring and plotting the resultant attenuated radiation as a function of wavelength [97].

The number of reflections into the sample can be controlled by varying the angle of incidence, ø. A high quality spectrum is obtained when the number of reflections is high. A detector is used to collect the exciting beam [95].

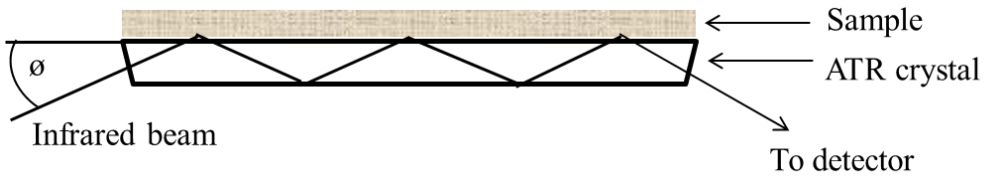

Figure 42. Schematic diagram of an infrared ATR cell set-up (from [95]).

5.9 Compressive Strength Tests

For the use of replicas in different applications it is necessary to determine their mechanical properties. Important mechanical properties include strength, hardness, ductility and stiffness [98, 99]. In this study, the compressive strength was measured.

The mechanical behavior may be assessed via a simple stress-strain test, whereby a load is static or changes relatively slowly with time and is applied uniformly over a cross section or surface of a sample. The cross section is normally circular, but rectangular specimens are also used. The load is applied uniaxially along the long axis of a specimen, causing deformation of the specimen. Usually the load is applied until the specimen fractures. Since the load-deformation characteristics are dependent on the specimen size, the respective parameters of stress and strain are used to minimize these geometrical factors, load and elongation [98].

Stress (σ) is defined by:

$$\sigma = \frac{F}{A_0} \qquad \textbf{Equation (40)}$$

where

F is the instantaneous load applied perpendicularly to the specimen cross section, in Newton (N) or pounds force (lb_f) unit

A_0 is the original crosssectional area before any load is applied (m^2 or $in.^2$)

The units of stress are mega pascals, MPa (SI), where 1 MPa is equal to 10^6 N/m^2 [98].

Strain (ε) is defined as:

$$\varepsilon = \frac{l_i - l_0}{l_0} = \frac{\Delta l}{l_0} \qquad \textbf{Equation (41)}$$

where

l_0 is the original length before any load is applied

l_i is the instantaneous length

Strain is unitless, but meters per meter or inches per inch are also often used. Sometimes strain is presented as a percentage (the strain value is multiplied by 100).

The stress-strain curves for three different materials at room temperature are shown in **Figure 43** [100-102]:

- Material I represents the characteristic behavior of many ceramics including hardened cement. This material has a high Young's modulus, high failure stress, low ductility, low toughness, and fractures without any significant plastic deformation.
- Material II represents the characteristic behavior of many metals. This material has moderate strength, moderate ductility, deforms plastically prior to failure and is the toughest of the three.
- Material III represents the characteristic behavior of many elastomers. This material has a low Young's modulus, is very ductile and has low ultimate tensile strength and limited toughness.

A compressive load produces contraction and negative linear strain as is shown in **Figure 44**. The force is compressive and the specimen contracts along the direction of the stress [98]. Compressive tests are used for materials which are brittle under tension such as *e.g.* concrete [98].

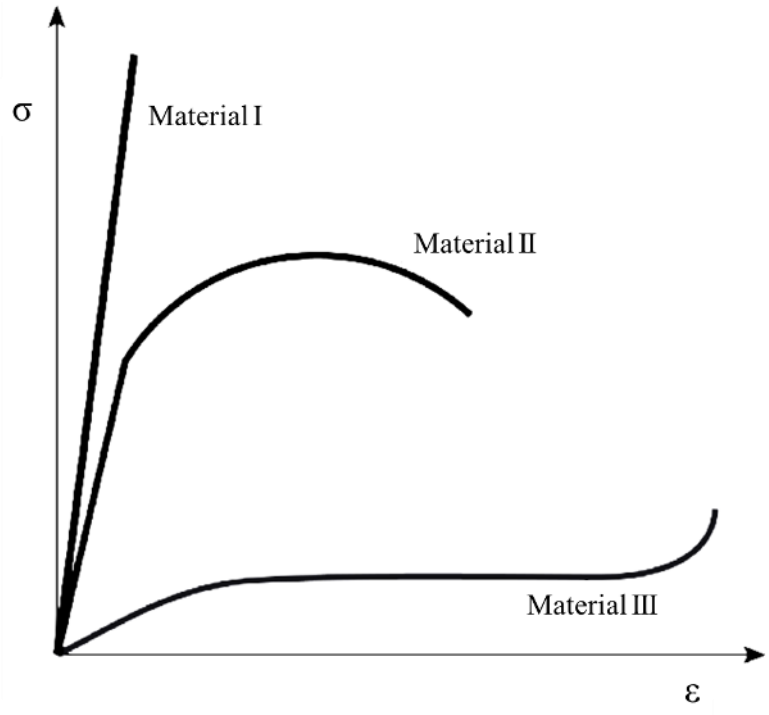

Figure 43. Idealized stress-strain curves for three classes of different materials (from [100]).

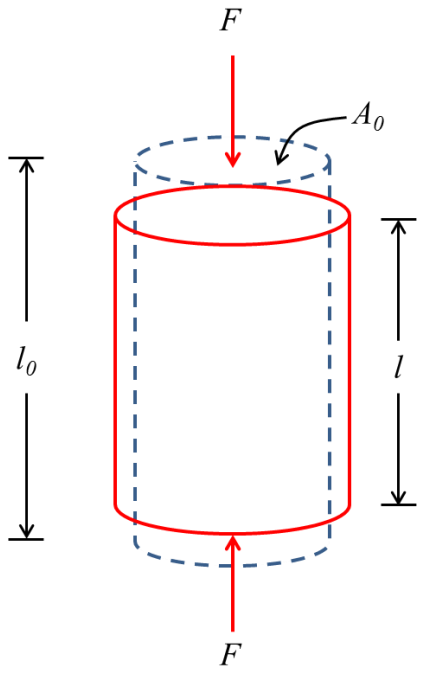

Figure 44. A compressive load produces contraction and a negative linear strain (from [98]).

6 Results and discussion

This chapter includes a summary of each publication attached to this thesis and briefly states the novelty of the work. Furthermore, additional results which were not yet published are presented at the end of the chapter.

6.1 Preparation of $CaCO_3$ and CaO Replicas Retaining the Hierarchical Structure of Spruce Wood

Paper #1

The first study which was published as paper #1 was conducted to produce positive replicas of spruce wood by infiltrating pretreated softwood templates with a $Ca(OCOOCH_3)_2$ precursor solution which was synthesized according to **Equations (1)** and **(2)**. Through hydrolysis of the calcium precursor caused by residual moisture present in the wood cells, $CaCO_3$ is eventually formed (**Equation (3)**).

It was found that this method allows successful replication of the hierarchical structure of the wood from the macroscopic to the submicron scale. Different materials were obtained, depending on the number of infiltration steps and the calcination conditions.

Synthesis of calcium dimethylate

$$Ca + 2\,CH_3OH \rightarrow Ca(OCH_3)_2 + H_2O\uparrow \qquad \textbf{Equation (1)}$$

Synthesis of calcium di(methylcarbonate)

$$Ca(OCH_3)_2 + 2\,CO_2 \rightarrow Ca(OCOOCH_3)_2 \qquad \textbf{Equation (2)}$$

Formation of a calcium carbonate sol/gel

$$Ca(OCOOCH_3)_2 + H_2O \rightarrow CaCO_3 + 2\,CH_3OH + CO_2\uparrow \qquad \textbf{Equation (3)}$$

One infiltration and calcination at 500 C° for 2 h led to a calcite replica which constitutes of individual submicron $CaCO_3$ particles, as was evidenced by SEM imaging (**Figure 45)**, with low mechanical stability. In order to improve the mechanical stability of the replica, two parameters were considered: the amount of precursor infiltrated and the calcination conditions (temperature and duration).

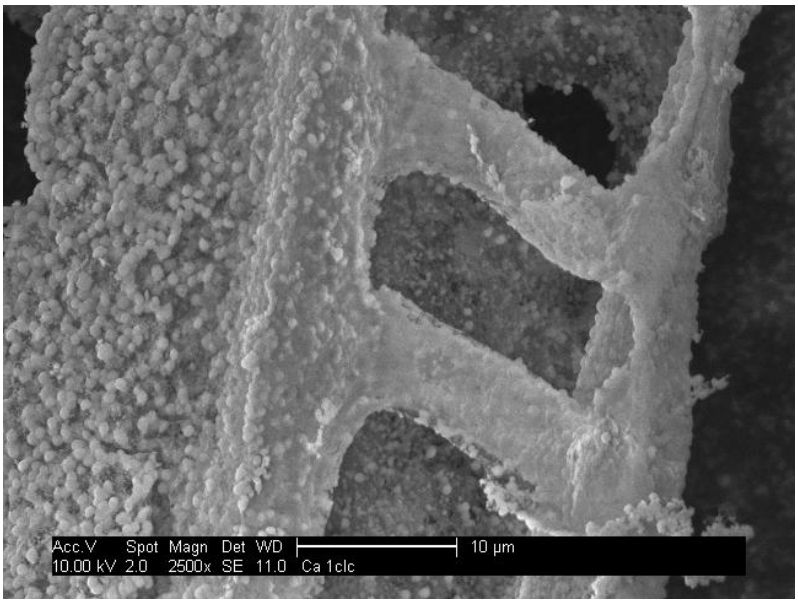

Figure 45. SEM image of a $CaCO_3$ replica containing the polymorph calcite, obtained from one infiltration and calcination at 500 °C for 2 h; it is obvious that the replica consists of spherical $CaCO_3$ nanoparticles.

The results show that neither only several infiltration steps and calcination at low temperature (500 °C) nor higher calcination temperatures (750 and 900 °C) and only one infiltration lead to replicas possessing sufficient mechanical stability. However, a combination of multiple infiltration steps and high calcination temperature proved to be the solution. The product from five infiltrations and subsequent calcination at 900 °C constituted an almost monolithic wood replica with reasonable mechanical stability.

The spruce wood template infiltrated 5 times by the calcium di(methylcarbonate) precursor solution (solid content 0.4 wt.%) before and after calcination at 900 °C for 2 h are shown in **Figures 46 (a)** and **46 (b)**, respectively. At this temperature, $CaCO_3$ decomposes into CaO and CO_2 and the CaO (as evidenced by XRD, diagram not shown here) was more annealed, as observed by SEM (**Figure 47**).

This research shows that the ionic character of $CaCO_3$ prevents it from sintering into mechanically more stable monoliths such as in SiO_2 replicas where covalent bonds are formed between the primary particles.

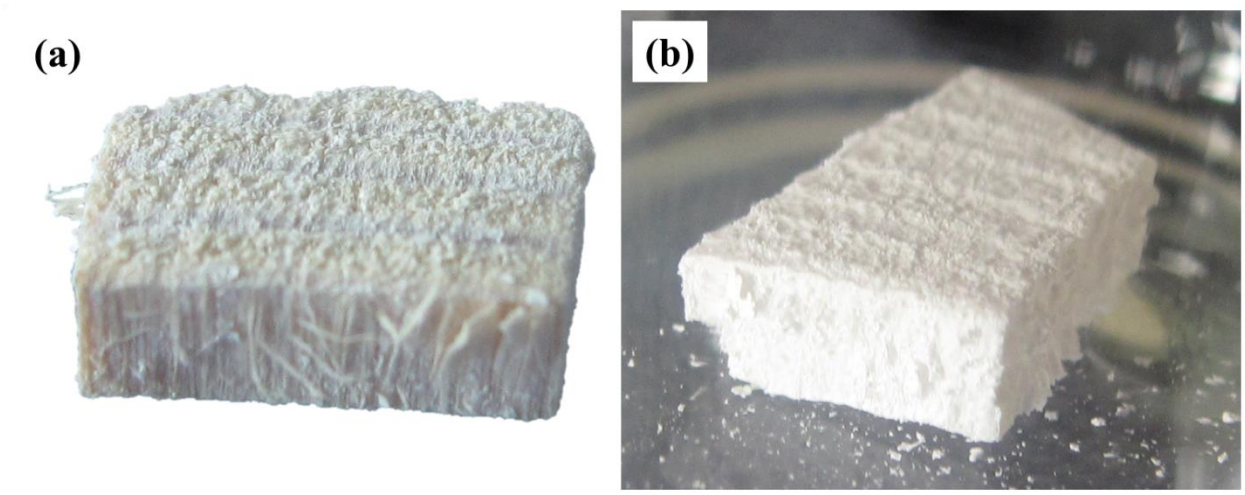

Figure 46. Spruce wood infiltrated 5 times with calcium di(methycarbonate) precursor solution (solid content 0.4 wt.%) before calcination (a) and after calcination at 900 °C for 2 h (b).

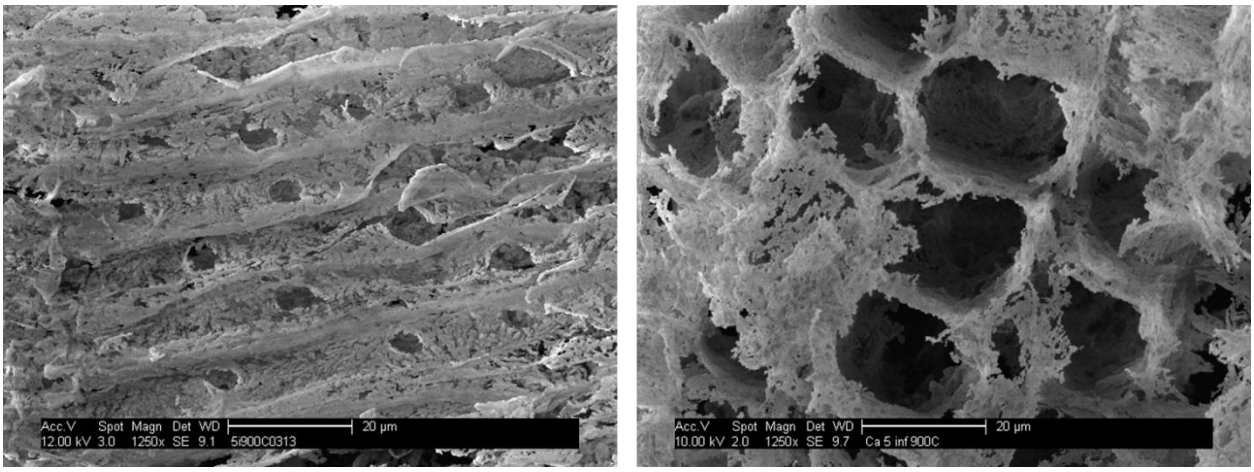

Figure 47. SEM images of the CaO replica obtained from 5 times infiltration and calcination at 900 C° for 2 h showing pit-hole structure (left) and honeycomb structure (right)

Preparation of $CaCO_3$ and CaO Replicas Retaining the Hierarchical Structure of Spruce Wood

Somruedee Klaithong[a], Daniel Van Opdenbosch[b], Cordt Zollfrank[b], and Johann Plank[a]

[a] Lehrstuhl für Bauchemie, Technische Universität München, 85747 Garching, Lichtenbergstraße 4, Germany

[b] Fachgebiet Biogene Polymere, Technische Universität München, 94315 Straubing, Schulgasse 16, Germany

Reprint requests to Prof. Dr. Johann Plank. Fax: +49-89-289-13152.
E-mail: sekretariat@bauchemie.ch.tum.de

Z. Naturforsch. **2013**, *68b*, 533 – 538 / DOI: 10.5560/ZNB.2013-3062
Received February 21, 2013

Dedicated to Professor Heinrich Nöth on the occasion of his 85th birthday

The principal structural characteristics of softwood (spruce) were replicated in $CaCO_3$ and CaO on various levels of hierarchy from the macroscopic to the submicron scale. Positive replicas were obtained by infiltrating pretreated softwood templates with a $Ca(OCOOCH_3)_2$ precursor solution which hydrolyzed into $CaCO_3$ nanoparticles. They reproduce the hierarchical porous structure of the wood template. Calcination at temperatures from 350 to 900 °C yields calcite as the main polymorph. Mechanical stability of the replica is optimized when the specimen is calcined at 900 °C.

Key words: Wood Template, Calcium Carbonate, Submicron Particles, Hierarchical

Introduction

Hierarchically structured inorganic materials have been recognized as attractive compounds and materials in applications such as catalysis, sensoring, pharmaceuticals, building materials, *etc.* [1]. For similar purposes, nano- and mesoporous materials are utilized as well. Some well documented examples include mesoporous silica (*e. g.* MCM-41), prepared with quaternary ammonium surfactants ("quats") as templating agents [2, 3], or nanoporous silica aerogels which are fabricated *via* sol-gel processess utilizing alkoxysilane precursors [4, 5]. Among those materials, aerogels stand out because of their unsurpassed heat insulating properties which derive from their nanoporosity and the Knudsen effect [6]. In spite of their many advantages, these porous materials exhibit a homogeneous porosity across the matrix which in many cases is undesirable. In specific applications, those materials require a three-dimensional hierarchy in addition to an anisotropic porosity. More recently, a number of hierarchically structured inorganic materials have been synthesized by using biological templates originating from plants (*e. g.* wood, seed, reed, bamboo) or animals (*e. g.* shell, nacre, tooth, bone) [7]. Replication of these structures was achieved by infiltrating the biotemplates with inorganic precursors and subsequent removal of the organic matrix *via* chemical or thermal treatment [8]. Wood has been identified as a versatile template. Contrary to *e. g.* aerogels, it combines an uniaxial porosity with high stiffness [7]. For example, spruce wood consists of parallel tube-like wood cells, the tracheid fibers, with a diameter in the range of 20 microns. In the cell wall of the tracheid fibers, cellulose fibrils are embedded in a hemicellulose and lignin matrix [9]. The cellulose fibrils are partly crystalline and they spiral the lumen at the characteristic microfibril angle [10]. Consequently, this structure is hierarchical at the nanometer level which was proven by SAXS analysis [11, 12]. Wood templates useful for the synthesis of porous materials can be prepared according to different methods. One process includes acid extraction followed by partial delignification with sodium chlorite [13]. This approach not only removes inorganic impurities, but also opens up the pore structure in order to create accessibility for the precursor molecules [14]. Furthermore, functionalization of the template with maleic acid anhydride was found to be

advantageous to stabilize the fibrillar structure and to reduce the shrinkage of the template [15 – 17]. Several attempts to replicate the hierarchical structure of wood from the micrometer to the nanometer scale were successful. For example, a hierarchically porous ceramic silica material was obtained by *in situ* mineralization of wood cellular structures infiltrated with a surfactant-templated sol-gel solution [18]. A hierarchically structured iron oxide possessing a tunable porous structure was synthesized from different wood templates [19]. Also, a highly crystalline porous oxide material was produced by infiltrating a $Ce_{0.5}Zr_{0.5}O_2$ sol into the tissue of wood [20]. Furthermore, a nanoscopic replication of the cellulose fibril was successfully fabricated by infiltrating TEOS into delignified and functionalized spruce wood templates [15]. Using tailor-made precursor sols and salt solutions, hierarchically structured phosphor materials based on softwood could be fabricated [21 – 23]. Very recently calcium carbonate aerogels have been considered as a potential replacement for polystyrene foam contained in heat insulating renders and panels used by the construction industry [24]. The preparation of $CaCO_3$ aerogels utilizes calcium di(methylcarbonate) as precursor and subsequent hydrolysis to calcium carbonate particles [25]. However, their poor mechanical strength currently restricts their use as insulating material in cement mixtures. Further, their purely nanometer-scale porosity does not allow reaction with microcrystalline cement hydrates and influences bonding to the cementitious matrix.

In this study, we investigated the fabrication of hierarchically structured $CaCO_3$ by using calcium di(methylcarbonate) as calcium precursor [25] and subsequent hydrolysis into a $CaCO_3$ sol. After infiltrating spruce wood templates with the precursor, their cellulose matrix was removed by calcination at temperatures varying between 350 and 900 °C. Calcination temperature and duration was varied in order to study their effect on the type of $CaCO_3$ polymorph formed, on the $CaCO_3$ particle size, the quality of replication, and the mechanical stability of the replica.

Results and Discussion

Calcium carbonate precursor

The concept of wood replication with $CaCO_3$ is based on the hydrolysis of calcium di(methylcarbonate) as precursor [25]. First, calcium dimethylate is prepared by reacting calcium metal with methanol (Eq. 1). Subsequent bubbling of gaseous CO_2 through this solution results in calcium di(methylcarbonate) (Eq. 2) which partly precipitates from the solution as several μm long needles which are removed by centrifugation. The clear solution (solid content 0.4 wt.-%) is used in the following infiltration process. Through hydrolysis of the calcium precursor with residual moisture present in the wood cells, $CaCO_3$ is eventually formed (Eq. 3) and successfully replicates the hierarchical structure of the wood. However, depending on the number of infiltration steps and the calcination conditions, different materials are obtained.

$$Ca + 2CH_3OH \rightarrow Ca(OCH_3)_2 + H_2 \uparrow \quad (1)$$

$$Ca(OCH_3)_2 + 2CO_2 \rightarrow Ca(OCOOCH_3)_2 \quad (2)$$

$$Ca(OCOOCH_3)_2 + H_2O \rightarrow CaCO_3 + 2CH_3OH + CO_2 \uparrow \quad (3)$$

Low-temperature treatment

Here, the pre-treated wood samples were infiltrated only once and treated thermally at 350 °C over a period of 48 h to decompose the wood template very slowly. This method produced large specimens which exceptionally precisely replicated the hierarchical structure as is shown in Fig. 1. Functional elements of the original wood samples such as pit holes were exactly replicated (Fig. 1a). Additionally, the tracheids of the wood are clearly reproduced in detail (Fig. 1b). Surprisingly, this product was found to consist of the meta-stable $CaCO_3$ polymorph vaterite as evidenced by XRD analysis (Fig. 2). Even a sample stored for 4 months still contained only vaterite, according to the XRD pattern (Fig. 2b). This demonstrates the exceptional stability of this polymorph under the given conditions.

Preparation of calcined replicas

A replica of the wood sample was produced by infiltrating a pretreated spruce wood template once with $Ca(OCOOCH_3)_2$ solution, followed by calcination at 500 °C for 2 h to completely remove the cellulose and other biopolymers. The resulting product consisted of a quite fragile positive $CaCO_3$ replica of the original wood template whereby the hierarchical structure was precisely reproduced by individual submicron $CaCO_3$ particles, as was evidenced by SEM imaging (Fig. 1c,

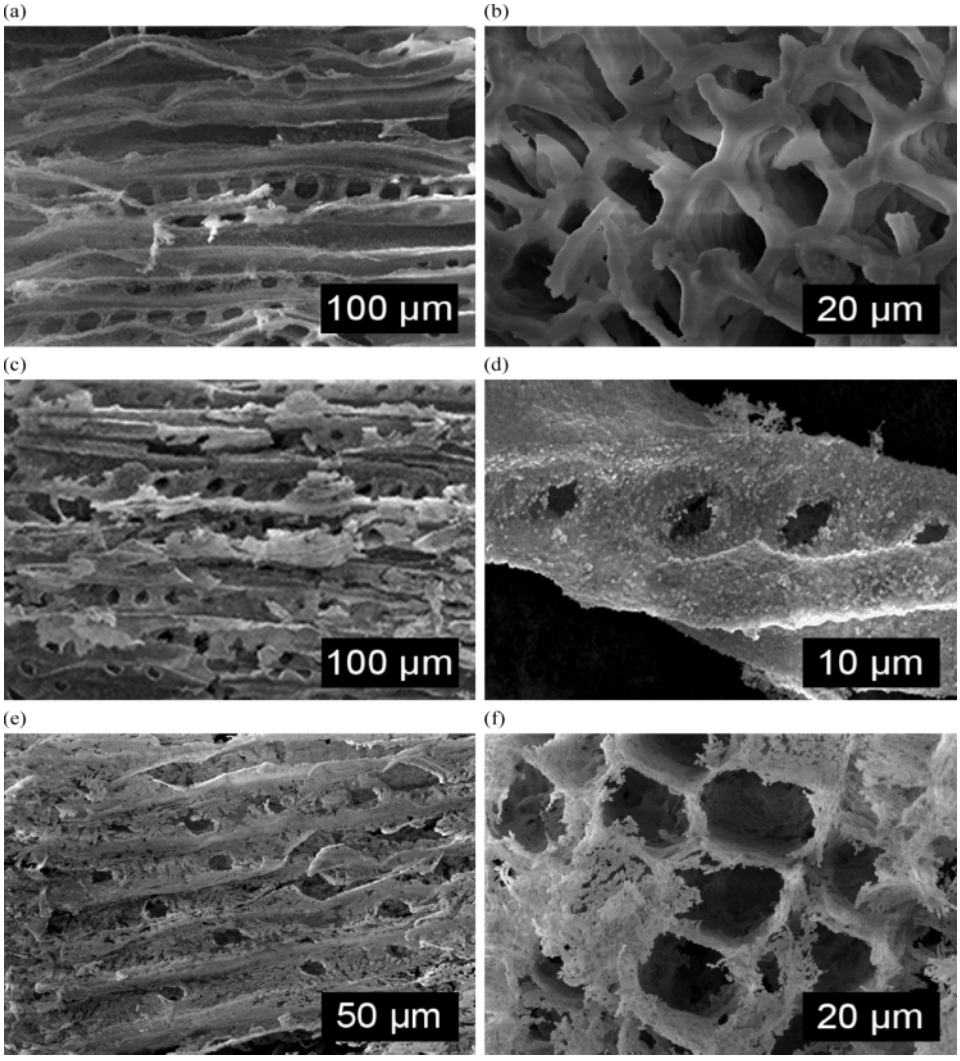

Fig. 1. SEM images of the $CaCO_3$-replicated wood samples: a, b) one infiltration and calcination at 350 °C for 48 h, resulting in a structure made of vaterite polymorph; c, d) one infiltration and calcination at 500 °C for 2 h leading to calcite and e, f) five infiltrations and calcination at 900 °C, producing CaO.

d). Spherical $CaCO_3$ particles with diameters of between 200 and 500 nm are visible which are assembled such as to replicate the structural features of the original wood, particularly the pit holes and tracheid fibers. This appearance differs significantly from previous silica replicas of wood where initially formed SiO_2 nanoparticles coalesced into an annealed monolith. As a result of the particulate structure, the $CaCO_3$ replica forms a fragile body with an extremely poor mechanical stability. XRD analysis revealed that the $CaCO_3$-replicated wood sample consisted only of the polymorph calcite (Fig. 2c).

Effect of multiple infiltration steps

In order to improve the mechanical stability of the replica, two parameters were considered: The amount of precursor infiltrated and the calcination conditions. At first, repeated infiltration steps were probed with the aim to obtain a more dense assembly of the $CaCO_3$

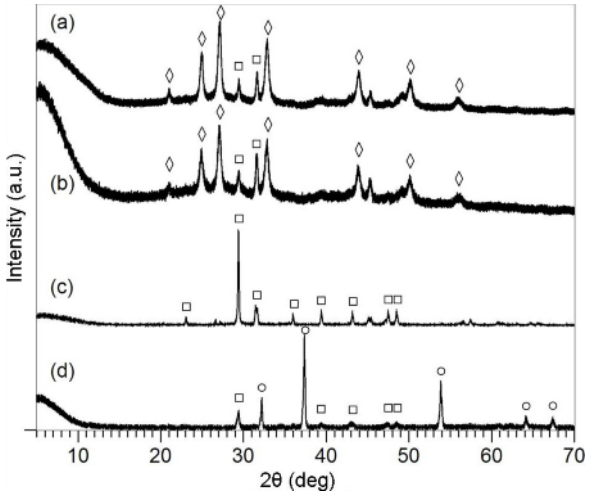

Fig. 2. XRD patterns of the $CaCO_3$-replicated wood samples: a, b) after thermal treatment at 350 °C (vaterite: JCPDS 25-127), c) after calcination at 500 °C for 2 h (calcite: JCPDS 05-586) and d) formation of CaO (JCPDS 37-1497) after calcination at 900 °C; ♢ = vaterite, □ = calcite, ◯ = CaO.

nanoparticles. These new samples were prepared by infiltrating them for 2 or 5 times and subsequent calcination at 500 °C for 2 h. After the first infiltration step, these samples were kept at 80 °C for 5 h before the second infiltration was conducted and subsequent calcination was performed. The twice infiltrated product was still fragile, but its stability had improved compared to the sample from one infiltration only. This effect can be attributed to larger and more compactly arranged submicron $CaCO_3$ particles ($d = 200$ nm to 1 μm). The number of infiltration steps was subsequently increased to 5. However, the stability of the replicas improved only slightly, and the material was still very brittle, thus limiting its applicability. SEM micrographs revealed that in spite of this multiple infiltration, a similar size and arrangement of the calcite particles like after two infiltrations was observed. From these results it was concluded that several infiltration steps do not lead to replicas possessing sufficient mechanical stability.

Effect of calcination temperature

Next, samples infiltrated once were calcined at 750 and 900 °C. The product obtained at 750 °C was similarly fragile as the sample calcined at 500 °C. However, calcination at 900 °C led to replicas consisting of CaO (as evidenced by XRD, see Fig. 2d) with again only slightly annealed particles, and thus with limited mechanical stability. Apparently, increasing the calcination temperature did not improve the mechanical stability of the replicas. It should be noted that when stored in air the CaO replica is hygroscopic and will be carbonated slowly over time.

Combination of multiple infiltrations and high calcination temperature

Furthermore, various combinations of multiple infiltration and high calcination temperature were probed. Samples infiltrated five times were calcined at 750 or 900 °C for 2 h. The product obtained at 750 °C exhibited higher stability compared to the product calcined at 500 °C only, but it still was much inferior to silica replicas [3]. However, the product calcined at 900 °C constituted an almost monolithic wood replica with reasonable stability. At this temperature, $CaCO_3$ decomposes into CaO and CO_2, the CaO (as evidence by XRD, diagram not shown here) being more annealed as observed by SEM (Fig. 1e, f). There, the well replicated honey comb structures of the cell wall as well as strongly annealed CaO particles are visible. From these experiments it was concluded that the ionic character of $CaCO_3$ prevents it from sintering into mechanically stable monoliths such as in SiO_2 replicas where covalent bonds are formed between the primary particles.

Specific surface area

Using the BET method, a specific surface area of 8.0 $m^2\,g^{-1}$ was found for the sample obtained from five infiltrations and calcination at 500 °C. This value is significantly lower than that reported for aerogels which lie between 45 and 200 $m^2\,g^{-1}$ [3, 24]. The result suggests that the $CaCO_3$ replicas produced here might be useful as carriers for drugs, catalysts or sensors. However, with respect to their thermal insulation properties they appear to be inferior to aerogels.

Conclusion

Our experiments have demonstrated that a $CaCO_3$ replica of hierarchically structured spruce wood can be obtained by infiltrating pretreated wood specimens with a solution of calcium di(methylcarbonate) in methanol which hydrolyses with residual moisture from the wood into a $CaCO_3$ sol. Upon calci-

nation, the sol produces $CaCO_3$ nanoparticles which precisely reproduce the mesoporous structure of the wood template. Heating to 900 °C transforms the $CaCO_3$ into a more robust CaO replica. The $CaCO_3$ replicas exhibit relatively poor mechanical stability and normally consist of the $CaCO_3$ polymorph calcite. Under mild, but extended calcination conditions (350 °C 48 h), the meta-stable $CaCO_3$ polymorph vaterite is formed. The specific surface area of the replicas is similar to that of mesoporous silica. In further experiments, the results obtained with other earth alkaline di(methylcarbonates), particularly of $Mg(OCOOCH_3)_2$, will be studied whereby a focus lies on the preparation of mechanically more stable replicas.

Experimental Section

Preparation of the template

The spruce wood samples (either cubes with side lengths of 1 cm or radial thin sections of 300 μm in thickness) were cut from the sapwood of spruce trees, weighed and subjected to a series of chemical treatments. In a first step, 150 g of wood was washed by extraction with 500 mL of a 2 : 1 by weight mixture of toluene and ethanol and then with the same volume of pure ethanol for 6 h each using a Soxhlet apparatus. All samples were stored in ethanol between the process steps to prevent drying. For preparation of the templates, 1 g of this wood was placed in an oxidizing solution containing 1.4 g of sodium chlorite ($NaClO_2$) and 0.5 g of acetic acid in 23.1 g of deionized water. Delignification was carried out twice at 70 °C for 3 h, the delignification solution being renewed after the initial 3 h. Afterwards, a mild vacuum from a water-jet pump was applied for half an hour. Following the delignification treatment, the templates were immediately extracted with ethanol to remove any residual solution [13].

Infiltration and calcination

Calcium metal in the amount of 1.5 g (0.0374 mol) was suspended in 250 mL absolute methanol (dried and stored over molecular sieve, 3 nm) and heated to 65 °C to produce a solution of $Ca(OCH_3)_2$. After 90 min of stirring at room temperature, carbon dioxide gas was bubbled through the $Ca(OCH_3)_2$ solution. After 90 min of reaction time, a turbid solution of $Ca(OCOOCH_3)_2$ had formed which was centrifuged. The clear solution (containing $\sim$ 13 g of the salt) was rinsed into a vial which contained the spruce wood template. Infiltration of the wood cells occurred during the drying process at 70 °C. The infiltrated wood template was then kept in an oven at 80 °C for 7 h and subsequently calcined *e. g.* at 500 °C for 2 h at a heating rate of 1 K min^{-1}. Additional calcination experiments were performed at 200, 330 and 470 °C for 0.5 h. Immediately after infiltration, hydrolysis of $Ca(OCOOCH_3)_2$ with residual moisture from the wood template occurred and a $CaCO_3$ sol was formed. SEM images of the product obtained from calcination were taken using an XL30 ESEM FEG instrument (FEI Company, Eindhoven/The Netherlands). The calcium carbonate polymorph contained in the replicas was indentified *via* X-ray diffraction (D8 advance, Bruker AXS instrument, Bruker, Karlsruhe/Germany). The specific surface area (BET method, N_2) was measured on a Nova 4000e, Quantachrome instruments (Boynton Beach, FL/USA) utilizing a sample degassed for 2 h at 200 °C.

Acknowledgement

Financial support by the German Research Foundation (Deutsche Forschungsgemeinschaft, DFG) within the framework of the priority program SPP1420 is gratefully acknowledged.

[1] C. E. Byrne, D. C. Nagle, *Carbon* **1997**, *352*, 259 – 266.
[2] C. Y. Mou, H. P. Lin, *Pure Appl. Chem.* **2000**, *72*, 137 – 146.
[3] H. Zheng, C. Gao, S. Che, *Micropor. Mesopor. Mater.* **2008**, *116*, 299 – 307.
[4] S. S. Kistler, *Nature* **1931**, *127*, 741 – 741.
[5] S. S. Kistler, *J. Phys. Chem.* **1932**, *36*, 52 – 64.
[6] K. Raed, U. Gross, *Int. J. Thermophys.* **2009**, *30*, 1343 – 1356.
[7] P. Fratzl, R. Weinkamer, *Pro. Mater. Sci.* **2007**, *52*, 1263 – 1334.
[8] O. Paris, I. Burgert, P. Fratzl, *MRS Bull.* **2010**, *35*, 219 – 225.
[9] D. Fengel, G. Wegener, A. Greune, *Wood Sci. Technol.* **1989**, *23*, 123 – 130.
[10] H. F. Jacob, D. Fengel, S. E. Tschegg, P. Fratzl, *Macromol.* **1995**, *28*, 8782 – 8787.
[11] A. Gourrier, W. Wagermaier, M. Burghammer, D. Lammie, H. S. Gupta, P. Fratzl, C. Riekel, T. J. Wess, O. Paris, *Appl. Crystallogr.* **2007**, *40*, s78–s82.
[12] O. Paris, *Biointerphases* **2008**, *3*, fb16 – fb26.
[13] P. A. Ahlgren, W. Q. Yean, D. A. I. Goring, *Tappi.* **1971**, *5*, 737.
[14] L. Sapei, R. Nöske, P. Strauch, O. Paris, *Chem. Mater.* **2008**, *20*, 2020 – 2025.

[15] D. Van Opdenbosch, G. Fritz-Popovski, O. Paris, C. Zollfrank, *J. Mater. Res.* **2011**, *26*, 1193 – 1202.
[16] C. Zollfrank, R. Kladny, H. Sieber, P. Greil, *J. Europ. Ceram. Soc.* **2004**, *24*, 479 – 487.
[17] G. Fritz-Popovski, D. Van Opdenbosch, C. Zollfrank, B. Aichmayer, O. Paris, *Adv. Funct. Mater.* **2013**, *23*, 1265 – 1272.
[18] Y. S. Shin, J. Liu, J. H. Chang, Z. M. Nie, G. Exarhos, *Adv. Mater.* **2001**, *13*, 728 – 732.
[19] Z. T. Liu, T. X. Fan, W. Zhang, D. Zhang, *Micropor. Mesopor. Mater.* **2005**, *85*, 82 – 88.
[20] A. Deshpande, I. Burgert, O. Paris, *Small* **2006**, *2*, 994 – 998.
[21] D. Van Opdenbosch, M. H. Kostova, S. Gruber, S. Krolikowski, P. Greil, C. Zollfrank, *Wood Sci. Technol.* **2010**, *44*, 547 – 560.
[22] M. H. Kostova, M. Batentschuk, F. Goetz-Neunhoeffer, S. Gruber, A. Winnacker, P. Greil, C. Zollfrank, *Mater. Chem. Phys.* **2010**, *123*, 166 – 171.
[23] M. H. Kostova, C. Zollfrank, M. Batentschuk, F. Goetz-Neunhoeffer, A. Winnacker, P. Greil, *Adv. Funct Mater.* **2009**, *19*, 599 – 603.
[24] T. Kornprobst, J. Plank, *GDCh-Monographie: Tagung Bauchemie* **2010**, *42*, 121 – 128.
[25] J. Plank, H. Hoffmann, J. Schölkopf, W. Seidl, I. Zeitler, Z. Zhang, *Res. Lett. Mater. Sci.* **2009**, 1 – 3.

6.2 Preparation of Magnesium Oxide and Magnesium Silicate Replicas Retaining the Hierarchical Structure of Pine Wood

Paper #2

In paper #1 it was demonstrated that the hierarchical structure of wood can be replicated by an alkaline earth metal carbonate like calcium carbonate. However, the $CaCO_3$ and CaO replicas exhibited low mechanical stability due to the ionic character of $CaCO_3$ which prevents it from sintering into mechanically stable monoliths. This makes them not suitable for actual application in construction application.

For this reason, methoxy magnesium methyl carbonate ($MeOMgOCO_2Me$) was used as a precursor in this **paper #2** in order to synthesize MgO replicas, according to the reactions presented in **Equations (42) – (44)**.

$$Mg + 2\,CH_3OH \rightarrow Mg(OCH_3)_2 + H_2\uparrow \qquad \textbf{Equation (42)}$$

$$Mg(OCH_3)_2 + (1+x)\,CO_2 \rightarrow Mg(OCOOCH_3)(OCH_3)\cdot xCO_2 \qquad \textbf{Equation (43)}$$

$$Mg(OCOOCH_3)(OCH_3)\cdot xCO_2 + H_2O \rightarrow MgCO_3 + 2\,CH_3OH + xCO_2\uparrow \qquad \textbf{Equation (44)}$$

Elemental mapping of magnesium in a cross section of the sample embedded in paraffin, performed after one infiltration, evidenced that magnesium was present only in the wood cell walls, indicating that the magnesium precursor had penetrated them and therein had formed hydrated $MgCO_3$ (nesquehonite) (XRD not shown here) (**Figure 48**).

Two infiltrations with $MeOMgOCO_2Me$ solution of low solid content (0.9 mass%) and calcination at 500 °C for 2 h provides a more precise replica (**Figure 49**). It replicates the characteristic structure of wood such as pit hole more precisely than the replicas infiltrated by a high solid content precursor solution (4.9 mass%). Calcination at 1450 °C leads to a replica consisting of larger annealed MgO particles exhibiting improved mechanical stability compared to the sample calcined at 500 ºC, however this condition has the disadvantage that the pit holes were no longer clearly visible and high shrinkage had occurred.

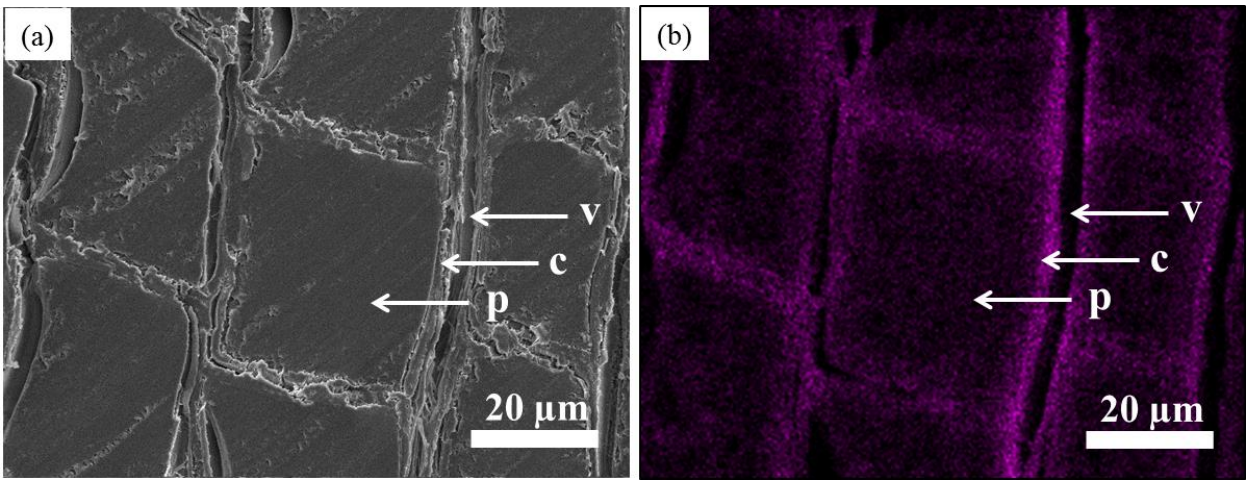

Figure 48. (a) SEM image of a cross section of a pine wood sample embedded in paraffin after one infiltration with the methanolic methoxy magnesium methylcarbonate precursor solution (p = paraffin, c = wood cell walls, v = void between wood cell walls), and (b) elemental mapping showing the accumulation of magnesium in the wood cell walls.

Infiltrating the pine wood template five times with 0.9 mass% $MeOMgOCO_2Me$ solution and subsequent immersion in TEOS solution and calcination at 1350 ºC led to a forsterite replica as a dominant product. It exhibited a compressive strength of 31 ± 8 MPa which was three times higher than that of a silica replica prepared according to the literature [8].

The results suggest that when the amount of magnesium precursor is high enough, then forsterite formation takes place through a reaction between MgO and the hydrolysed alkoxysilane, as is presented in **Equations (45)** and **(46)**.

$$MgO + SiO_2 \text{ (amorphous)} \rightarrow MgSiO_3 \text{ (enstatite, metastable)} \qquad \textbf{Equation (45)}$$

$$MgO + MgSiO_3 \rightarrow Mg_2SiO_4 \text{ (forsterite)} \qquad \textbf{Equation (46)}$$

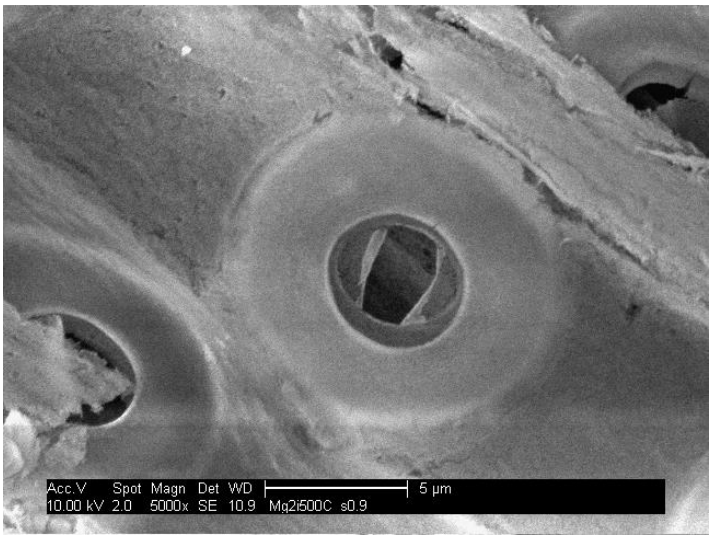

Figure 49. Replica from two infiltrations with 0.9 mass% $MeOMgOCO_2Me$ solution and calcination at 500 ºC for 2 h.

DE GRUYTER Z. Naturforsch. 2017; 72(5)b: 341–349

Somruedee Klaithong, Daniel Van Opdenbosch, Cordt Zollfrank and Johann Plank*

Preparation of magnesium oxide and magnesium silicate replicas retaining the hierarchical structure of pine wood

DOI 10.1515/znb-2016-0241
Received November 23, 2016; accepted December 16, 2016

Abstract: Replicas retaining the structural characteristics of softwood (*Pinus sylvestris*) were obtained by infiltrating pretreated templates with a methanolic methoxymagnesium methyl carbonate ($MeOMgOCO_2Me$) solution as a precursor which then hydrolyzed into $MgCO_3$ nanoparticles. Subsequent calcination at temperatures ranging from 500 to 1450°C yielded annealed MgO replicas on levels of hierarchy from the macroscopic to the submicron scale. The mechanical stability of the replicas could be improved through calcination at 1450°C. However, this treatment leads to considerable shrinkage ($\Delta_{ax} = 56\%$). Even more stable MgO replicas were obtained by infiltrating the pine template first with $MeOMgOCO_2Me$, followed by a second infiltration step with an ethanolic tetraethyl orthosilicate (TEOS) solution and subsequent calcination at 1350°C. The resulting replicas constitute an MgO framework overgrown with Mg_2SiO_4 (forsterite) and exhibit compression strengths of 31 ± 8 MPa, as well as hierarchical structures combined with an anisotropic porosity.

Keywords: biotemplating; hierarchical structure; magnesium oxide; magnesium silicate; wood template.

1 Introduction

Silica aerogels are highly attractive materials because of their exceptional thermal insulating property resulting from the Knudsen effect [1]. They can be fabricated, e.g. via a sol–gel process utilizing an alkoxysilane as precursor [2, 3]. Aerogels possess a non-hierarchical porosity across the matrix which in some applications is undesirable. However, for certain purposes a three-dimensional hierarchy associated with anisotropic porosity is advantageous. For example, hierarchical structures provide higher chances to trap particles with different diameters in fibrous membranes applied for air filtration [4]. Another example where hierarchically porous morphologies are desirable are, e.g. lithium-ion batteries. A nanoporous structure accelerates lithium ion intercalation/deintercalation and electron transport, and enlarges the electrode–electrolyte interphase area, while micron-sized assemblies provide high volumetric density, easy processability and electrode integrity [5].

Wood has been identified as a versatile template exhibiting a hierarchical structure [6]. Spruce wood is a soft-wood consisting of parallel tube-like wood cells, the tracheid fibers, with diameters in the range of 10–40 µm. In the cell walls of the tracheid fibers, cellulose fibrils are accompanied by polyoses which are embedded altogether in a lignin matrix [7]. The cellulose elementary fibrils are partly crystalline and exhibit a thickness of around 2.5 nm. The fibrils spiral the lumen at the characteristic microfibril angle [8].

The advantage of using wood as a template is an easy access to hierarchically porous materials [6]. To achieve a good replication, the wood template needs to be extracted with organic solvents in order to remove inorganic impurities, followed by partial delignification with sodium chlorite to open up the pore structure for accessibility of the precursor molecules [9, 10]. In this manner, a successful nanoscopic replication of cellulose fibrils was fabricated by infiltrating tetraethyl orthosilicate (TEOS) into delignified spruce wood followed by calcination [11]. During the calcination step, polyoses decompose between 250 and 300°C, resulting in a silica network in the form of long fibrils exhibiting a diameter of about 10 nm, embedded in the partly intact cellulose microfibrils. The cellulose elementary fibrils are further degraded between 350 and 450°C. In their place, corresponding nanopores with diameters of 2 nm are formed. These pores are stable up to 625°C, beyond which sintering occurs [12]. Furthermore, other groups have prepared tailor-made precursor sols

***Corresponding author: Johann Plank,** Lehrstuhl für Bauchemie, Technische Universität München, Lichtenbergstraße 4, 85747 Garching, Germany, Fax: +49-89-289-13152,
E-mail: sekretariat@bauchemie.ch.tum.de
Somruedee Klaithong: Lehrstuhl für Bauchemie, Technische Universität München, Lichtenbergstraße 4, 85747 Garching, Germany
Daniel Van Opdenbosch and Cordt Zollfrank: Chair für Biogenic Polymers, Technische Universität München, Schulgasse 16, 94315 Straubing, Germany

and salt solutions and used them to fabricate hierarchically Eu-doped Y_2O_3 from softwood [13–15].

Owing to their nanoporosity, calcium carbonate aerogels have recently been proposed as potential replacements for polystyrene foams contained in heat insulating renders and panels used by the construction industry [16, 17]. Also, magnesium carbonate xerogels and aerogels which consist of networks of magnesium carbonate nanoparticles were produced by controlled hydrolysis of methoxymagnesium methyl carbonate, $Mg(OCOOCH_3)(OCH_3)$ ($MeOMgOCO_2Me$) [18]. These aerogels composed of alkaline earth metal compounds are of special interest for construction applications because of their high compatibility and inertness towards cement [18]. Furthermore, such porous materials are also interesting as functionalized supports for other applications, for example the adsorption of heavy-metal ions from aqueous solution using mercapto-modified silica particles [19].

Magnesium silicate (forsterite), Mg_2SiO_4, constitutes the most abundant mineral in the Earth's upper mantle and transition zone [20]. Because of the exceptionally high fracture toughness of forsterite, this material has been proposed as a potential alternative to calcium phosphate bioceramics [21]. Through calcination of the wet gel obtained from $Mg(NO_3)_2 \cdot 6H_2O$ and colloidal SiO_2 in a sol–gel process at 1450°C, forsterite ceramics with exceptionally high bending strength and fracture toughness, even superior to those of currently known hydroxyapatite ceramics, were obtained [22]. Furthermore, forsterite nanopowder was produced via a sol–gel process [23, 24]. In a study of the sinterability of forsterite powder synthesized via solid-state reaction using MgO and talc ($Mg_3Si_4O_{10}(OH)_2$) it was found that the mechanical properties were improved when the calcination temperature was increased from 1200 to 1400°C. However, higher sintering temperatures led to grains larger than ~22 µm, resulting in lower values of hardness and fracture toughness [25]. The product formed was phase-pure forsterite, and no decomposition into phases such as MgO or enstatite was observed. Furthermore, nanostructured forsterite bioceramics were shown to possess excellent mechanical properties and thus can be used as a bioactive bone tissue engineering material [24].

In previous research, we have synthesized a $CaCO_3$ replica of hierarchically structured spruce wood by infiltrating pretreated wood specimens with a solution of calcium di(methylcarbonate) in methanol. This precursor hydrolyses into a $CaCO_3$ sol [26, 27]. However, the disadvantage of these $CaCO_3$ replicas is their poor mechanical stability which limits their use, e.g. for construction applications. In the present work we investigate the fabrication of hierarchically structured MgO replicas. It was hoped that the MgO replicas would exhibit higher mechanical stability than the previously synthesized porous $MgCO_3$ monoliths [18] by using $MeOMgOCO_2Me$ as a magnesium precursor and subsequent hydrolysis into a $MgCO_3$ sol inside the wood cell walls. After infiltration, the cellulose matrix was removed by calcination at temperatures ranging from 500 to 1450°C yielding porous monoliths composed of MgO nanoparticles. The calcination temperature was varied in order to study its effect on the MgO particle size, the quality of replication and the mechanical stability of the replicas. Additionally, magnesium silicate replicas exhibiting high compressive strength were synthesized by infiltrating the MgO replica with an alkoxysilane precursor and subsequent calcination at 1350°C. For this system, the temperature-dependent formation of different magnesium silicates was studied.

2 Results and discussion

2.1 Magnesium carbonate precursor

The concept of wood replication with MgO was based on the hydrolysis of methoxymagnesium methylcarbonate as a precursor, as was reported earlier [18]. For this purpose, magnesium methanolate was prepared by reacting magnesium metal with methanol (eq. 1) [28, 29]. Subsequent bubbling of gaseous CO_2 through this solution results in methoxymagnesium methylcarbonate which physically binds an additional amount of CO_2 (eq. 2) [18, 30]. The structure of this compound has been confirmed in an earlier work [18]. Using IR and elemental analysis it has been shown that CO_2 inserts into one methylate group resulting in $Mg(OCO_2Me)(OMe)$. The clear solution (solid content 4.9 mass%) thus obtained was used in the following infiltration process. Dynamic light scattering showed that no sol particles were present in the $MeOMgOCO_2Me$ solution prior to infiltration. It revealed that sol particles in the range of 0.6 to 11.0 nm were formed only after additional water was added to the $MeOMgOCO_2Me$ solution. However, such sol particles would be unable to diffuse into polyoses [12, 27]. Therefore, it can be hypothesized that the $MeOMgOCO_2Me$ solution reacts with the moisture inside the wood cell wall to form a sol and, most likely, later a gel. Consequently, $MgCO_3$ was obtained from the magnesium precursor (eq. 3). After calcination in air, the macroscopic and submicron scale structure of the wood was replicated. However, depending on the number of infiltration steps and the calcination conditions, materials

with different structures were obtained, as discussed in the following.

The infiltration process was assessed by elemental mapping of magnesium in a cross section of the sample embedded in paraffin, performed after one infiltration. It revealed that magnesium was present only in the wood cell walls, indicating that the magnesium precursor had penetrated them and therein had formed hydrated $MgCO_3$ (nesquehonite) [X-ray diffraction (XRD) not shown here] (Fig. 1). The voids between the cell walls originated from the delignification process.

$$Mg + 2\,CH_3OH \rightarrow Mg(OCH_3)_2 + H_2\uparrow \quad (1)$$

$$Mg(OCH_3)_2 + (1+x)\,CO_2 \rightarrow Mg(OCOOCH_3)(OCH_3)\cdot xCO_2 \quad (2)$$

$$Mg(OCOOCH_3)(OCH_3)\cdot xCO_2 + H_2O \rightarrow MgCO_3 + 2\,CH_3OH + xCO_2\uparrow \quad (3)$$

2.2 Preparation of MgO replicas

A replica of the delignified pine wood sample was produced by infiltrating the pretreated template one time with $MeOMgOCO_2Me$ solution, followed by calcination at 500°C for 2 h to completely remove all organic matter. The resulting product constituted a positive, yet very fragile MgO replica of the original wood template, whereby the hierarchical structure was reproduced by annealed submicron-sized MgO particles possessing diameters of 200–500 nm (Fig. 2a). As a result of this particulate structure, the MgO replica presented a fragile body exhibiting poor mechanical stability and high shrinkage ($\Delta_{rad} = 26\%$ and $\Delta_{tan} = 25\%$; determination of Δ_{ax} was not feasible). XRD analysis revealed that the sample consisted of the polymorph periclase of MgO (Fig. 3a).

2.3 Effect of multiple infiltration

In order to improve the mechanical stability of the replica, three parameters were considered: The amount of precursor infiltrated, the calcination temperature and additional infiltration with an alkoxysilane precursor. At first, repeated infiltration steps were performed with the aim to obtain a more dense assembly of the MgO submicron particles. Such samples were prepared by immersing the pine template twice in the Mg precursor solution and subsequent calcination at 500°C for 2 h. After the first infiltration, the samples were kept at 80°C for 5 h before the second immersion step was conducted and calcination was performed. The resulting product was still fragile, but its mechanical stability had improved noticeably compared to the sample obtained after one infiltration only, providing a compressive strength of 1.0 ± 0.2 MPa (Fig. 4a). This effect can be attributed to the formation of larger and more densely arranged submicron MgO particles (d = 200–600 nm), as observed by scanning electron microscopy (SEM) and lower shrinkage ($\Delta_{rad} = 18\%$ and $\Delta_{tan} = 17\%$; determination of Δ_{ax} was not possible).

Interestingly, the stress-strain curves does not show a linear increase due to elastic deformation, followed by a sharp drop in stress due to final catastrophic failure, as expected in a ceramic material. Instead, the curve shows a linear increase whose inclination drops close to the maximum compressive strength. The material failure is

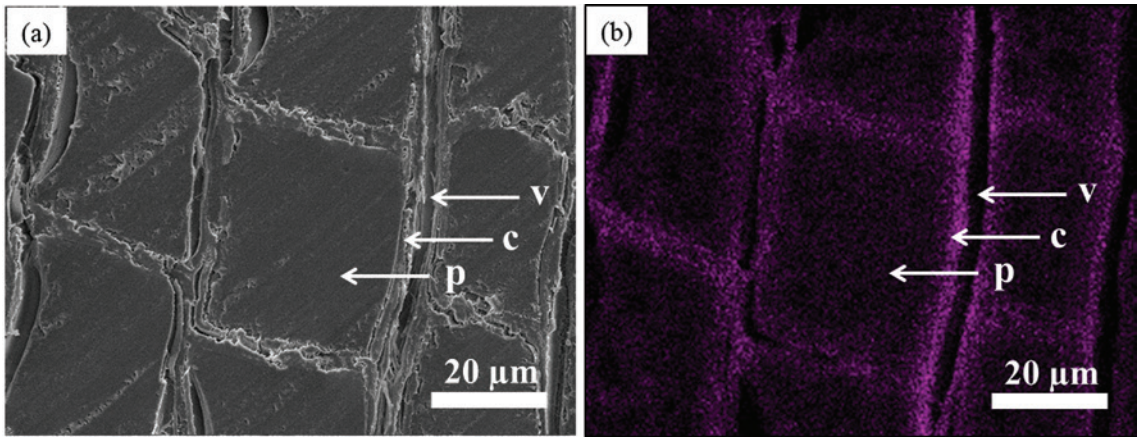

Fig. 1: (a) SEM image of a cross section of a pine wood sample embedded in paraffin after one infiltration with the methanolic magnesium precursor solution (p = paraffin, c = wood cell walls, v = void between wood cell walls), and (b) elemental mapping showing the accumulation of magnesium in the wood cell walls.

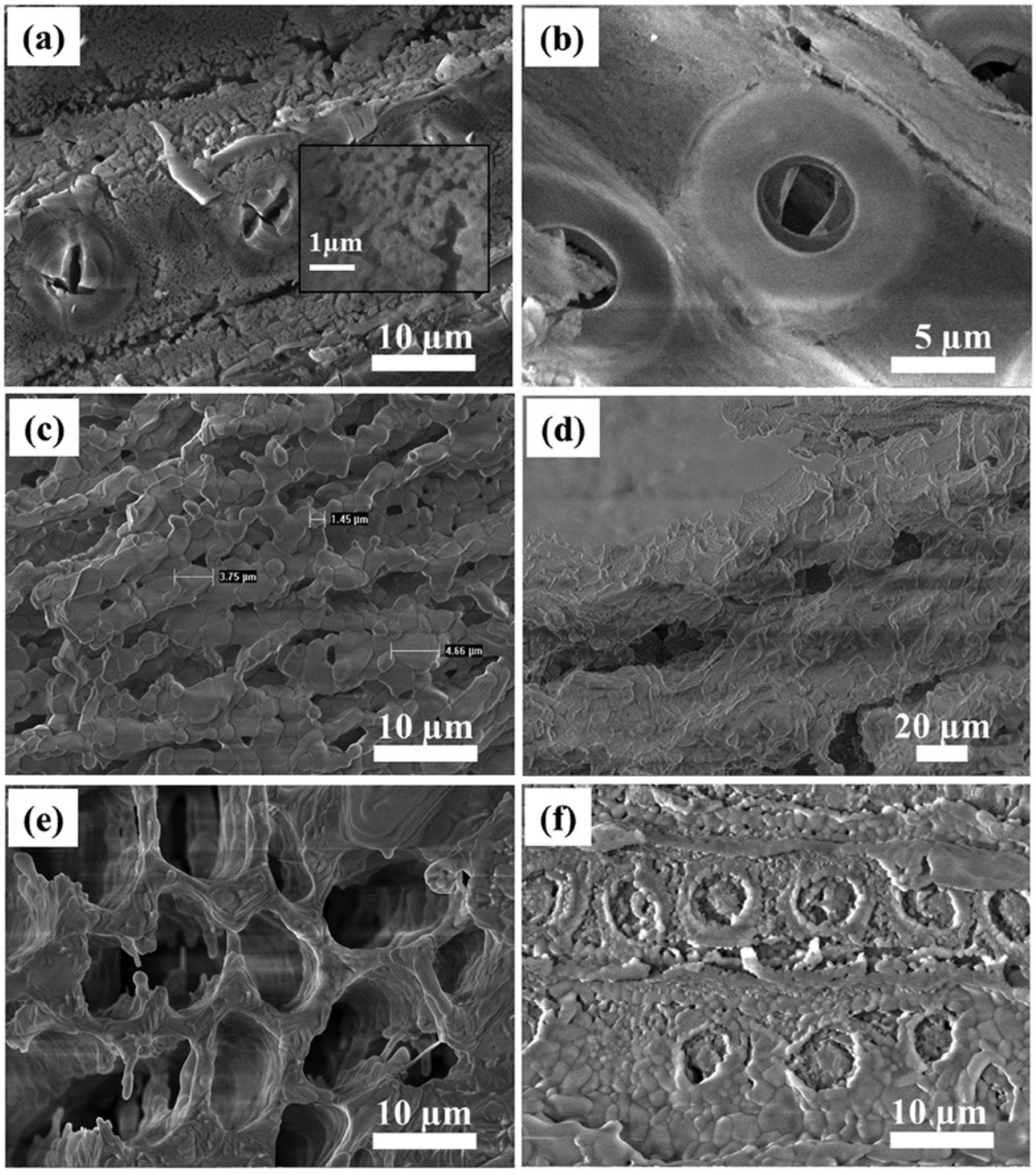

Fig. 2: SEM images of the MgO replicated wood samples: (a) one infiltration with 4.9 mass% $MeOMgOCO_2Me$ solution and calcination at 500°C for 2 h; (b) two infiltrations with 0.9 mass% $MeOMgOCO_2Me$ solution and calcination at 500°C for 2 h; (c) two infiltrations with 0.9 mass% $MeOMgOCO_2Me$ solution and calcination at 1450°C for 5 h; (d) and (e) forsterite/enstatite-replicated wood sample obtained after five infiltrations with 0.9 mass% $MeOMgOCO_2Me$ solution, subsequent soaking with TEOS and calcination at 1350°C for 5 h; and (f) forsterite/MgO replica from one infiltration with 4.9 mass% $MeOMgOCO_2Me$ solution, subsequent soaking with TEOS and calcination at 1350°C for 5 h.

defined by a gradual drop in recorded stress over a compression strain range of more than 20%. We interpret this as a successive fracture of connecting struts or sintering necks, leading to a gradual compaction of the material. We observed that after a compression strain of 30%, the recorded stresses again increased, due to the powdered sample being compacted. This shows that the retention of the hierarchical wood structure increases the resilience of the material to catastrophic fracture, and allows for a large degree of plastic deformation.

Additional tests involving multiple infiltration steps and calcination at 500°C did not lead to samples

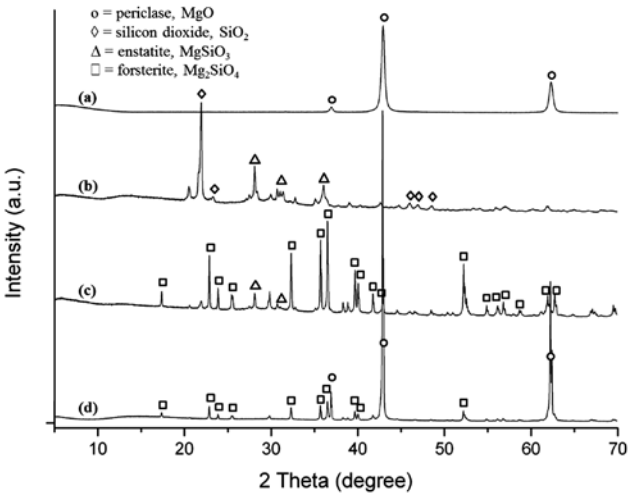

Fig. 3: XRD patterns of the MgO and forsterite replicated wood samples: (a) after thermal treatment at 500°C for 2 h (periclase, MgO: JCPDS 45-0946); (b) after one infiltration with 0.9 mass% $MeOMgOCO_2Me$ solution, subsequent soaking with TEOS and calcination at 1350°C for 5 h (silicon dioxide, SiO_2: JCPDS 14-0260 and enstatite, $MgSiO_3$: JCPDS 07-0216); (c) forsterite/enstatite obtained from five infiltrations with 0.9 mass% $MeOMgOCO_2Me$ solution, subsequent soaking with TEOS and calcination at 1350°C for 5 h (forsterite, Mg_2SiO_4: JCPDS 89-5130); and (d) formation of forsterite, Mg_2SiO_4 and periclase, MgO after one infiltration with 4.9 mass% $MeOMgOCO_2Me$ solution, subsequent soaking with TEOS and calcination at 1350°C for 5 h.

possessing further enhanced mechanical stability. Thus it was concluded that two infiltration steps represented the optimum with respect to the compressive strength of the sample.

2.4 Effect of low precursor concentration

The most likely infiltration mechanism starts with the methyl carbonate precursors entering the lumen via convection, followed by diffusion into the cell walls driven by concentration gradients [27]. After the infiltration, the liquid phase was evaporated, leading to further condensation of the precursor by loss of alcohol. Since the cell walls provide limited space, a large fraction of the high solid content of the $MeOMgOCO_2Me$ is deposited in the cell lumen, as observed via SEM (Fig. 2a).

In the literature, to achieve SiO_2 replicas that are accurate on the nanometer scale, repeated infiltration with low concentration precursors was found to be suitable [11]. Correspondingly, the solid content of the $MeOMgOCO_2Me$ precursor solution was reduced from 4.9 to 0.9 mass%. Again, calcination was performed at 500°C over 2 h. This approach led to a more precise replica (the characteristic pit hole structure was better replicated) composed of annealed submicron MgO particles exhibiting diameters of 200–500 nm. Furthermore, the template was infiltrated twice to achieve the desired higher mechanical stability, as presented before. The replica now precisely revealed the characteristic pit holes structure of wood (Fig. 2b). The downside was an even increased shrinkage of $\Delta_{rad} = 37\%$ and $\Delta_{tan} = 33\%$.

2.5 Effect of calcination temperature

The samples infiltrated twice with a precursor solution of low solid content (0.9 mass%) were calcined for 5 h at considerably higher temperatures as before, namely at 1000 and 1450°C, respectively. The product obtained at 1000°C was as fragile as the sample calcined at 500°C. However, calcination at 1450°C led to a replica now consisting of larger annealed MgO particles (periclase polymorph, as determined by XRD) with sizes ranging from 600 nm to 5 µm (Fig. 2c). At this temperature, highly annealed MgO particles exhibiting improved mechanical stability compared to the sample calcined at 500°C are formed owed to high particle compaction. Consequently, at this calcination temperature, shrinkage values of $\Delta_{ax} = 56\%$, $\Delta_{rad} = 65\%$ and $\Delta_{tan} = 62\%$ had occurred. In addition, this product had lost the characteristic microstructure of wood. For example, the pit holes were no longer clearly visible (Fig. 2c).

2.6 Combined treatment with Mg and Si precursors

In another series of experiments, the wood templates were infiltrated once with the magnesium precursor and then additionally immersed in an ethanolic TEOS solution. Alternatively, the imbibition with TEOS was also carried out after calcination of the magnesium infiltrated samples. The consideration behind this consecutive treatment was to coat the initially formed MgO replica with a layer of SiO_2 or magnesium silicate which was expected to further improve the compressive strength of the replica. Calcination was carried out at 1350°C for 5 h. According to literature, this condition produces single-phase forsterite [25, 31]. The sample resulting from one Mg infiltration and TEOS treatment before calcination constituted a monolithic piece containing annealed particles in the range of 500 nm to 3 µm, but it did not show the characteristic structures of wood (pit holes, etc.). XRD patterns revealed that this material consisted of a mixture of silicon dioxide,

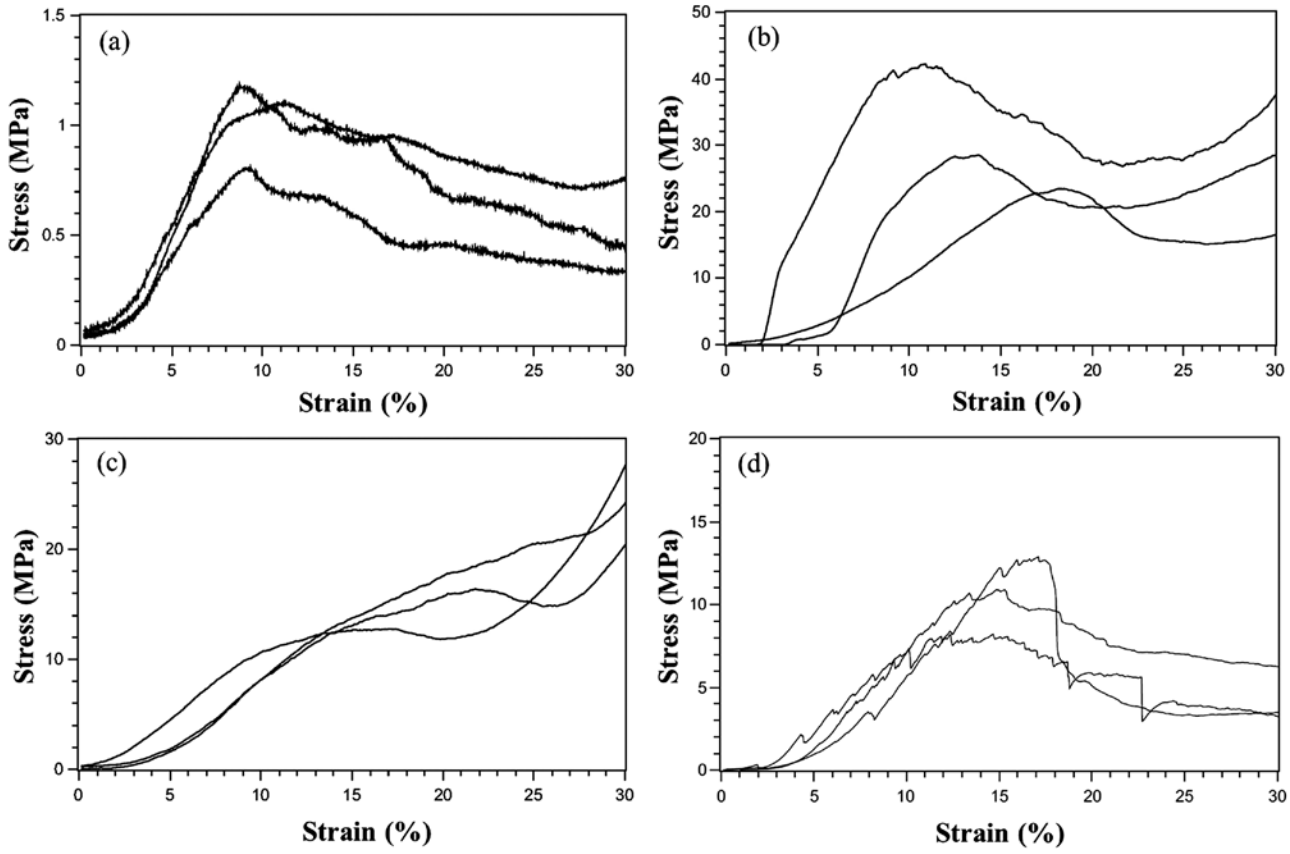

Fig. 4: Compression stress/strain curves of MgO, forsterite and silica replicated wood samples: (a) after 2 infiltrations with 4.9 mass% $MeOMgOCO_2Me$ solution, subsequent calcination at 500°C 2 h; (b) after 5 infiltrations with 0.9 mass% $MeOMgOCO_2Me$ solution, subsequent immersion in TEOS solution and calcination at 1350°C 5 h; (c) after 1 infiltration with 4.9 mass% $MeOMgOCO_2Me$ solution, subsequent immersion in TEOS solution and calcination at 1350°C 5 h; and (d) silica replica prepared after [11]. The three curves shown for each sample represent three independent measurements.

SiO_2 and enstatite, $MgSiO_3$, a metastable phase (Fig. 3b). Apparently, under those conditions there is not enough magnesium precursor present to form the thermodynamically stable forsterite, Mg_2SiO_4.

2.7 Preparation of forsterite replica

In order to increase the amount of magnesium in the sample that is subsequently treated with the alkoxysilane, it was infiltrated five times with $MeOMgOCO_2Me$ solution (solid content 0.9 mass%) before adding the TEOS solution and subsequent calcination at 1350°C for 5 h. This process led to a mixture of forsterite (Mg_2SiO_4) as the dominant product, and residual amounts of clinoenstatite, as confirmed by XRD (Fig. 3c) and ^{29}Si MAS nuclear magnetic resonance (NMR) spectroscopy (Fig. 5). In these spectra, the signal at –61.79 ppm can be attributed to Si in Q^0 coordination mode. This chemical shift has been reported before

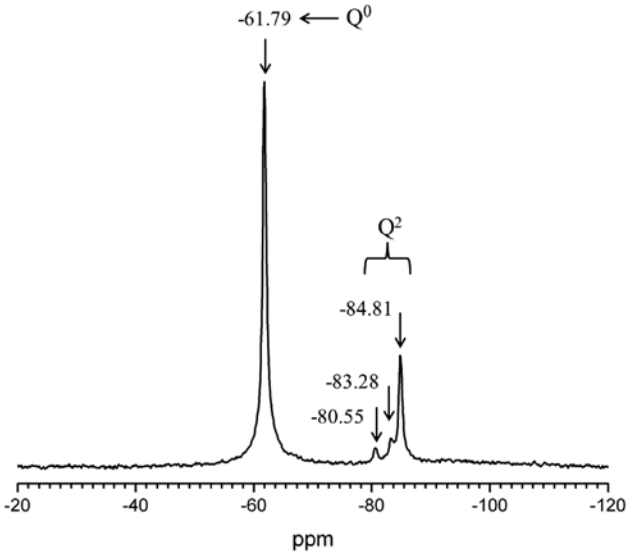

Fig. 5: ^{29}Si MAS NMR spectrum of the sample obtained after five infiltrations with 0.9 mass% $MeOMgOCO_2Me$ solution, subsequent immersion in TEOS solution and calcination at 1350°C for 5 h.

for forsterite [32–34]. Furthermore, three resonances are present at −80.55, −83.28, and −84.81 ppm which can be assigned to ortho or clinoenstatite [32]. Integration of the peak areas indicates a ratio of 78% for Q^0 (forsterite) and 22% for Q^2 (ortho or clinoenstatite). These results suggest that when the amount of magnesium is sufficient and the calcination temperature is high enough, then forsterite is formed through a reaction between MgO and the hydrolysed alkoxysilane, as presented in eqs. 4 and 5.

$$MgO + SiO_2(\text{amorphous}) \rightarrow MgSiO_3(\text{enstatite, metastable}) \quad (4)$$

$$MgO + MgSiO_3 \rightarrow Mg_2SiO_4 \ (\text{forsterite}) \quad (5)$$

The replica consists of annealed particles in the range of 500 nm to a few micrometers (Fig. 2d, e). However, shrinkage of the porous monolith was still at $\Delta_{ax} = 31\%$, $\Delta_{rad} = 50\%$ and $\Delta_{tan} = 48\%$. This sample showed a compressive strength of 31 ± 8 MPa (Fig. 4b). The stress–strain curves show the same progression, atypical for ceramic materials, as already observed for the samples calcined at 500°C (Fig. 4a). This confirms that the progression of the curve is due to the samples' micro-, and not their crystal structures.

Samples calcined at 1350°C and containing high Mg contents were obtained by infiltrating $MeOMgOCO_2Me$ at a solid content of 4.9 mass%, instead of 0.9 mass%, followed by a TEOS treatment. The replica obtained from this process contained a mixture of forsterite and periclase, as shown in the XRD pattern (Fig. 3d). Apparently, under those conditions the initial MgO framework had partly reacted with the silicon precursor resulting in a layer of magnesium silicate. Apparently, only the surface of the magnesium oxide framework which had contact with the silicon precursor had reacted, thus leaving the inner MgO framework intact and yielding a mixture of forsterite and MgO as was evidenced in the XRD pattern. This sample exhibited a compressive strength of 17 ± 3 MPa (Fig. 4c) and reproduced the wood structure such as pit holes precisely. It contained annealed particles in the range of 500 nm to a few micrometers, but exhibited decreased porosity as seen in the SEM image (Fig. 2f). Again, shrinkage was substantial, with $\Delta_{ax} = 43\%$, $\Delta_{rad} = 49\%$ and $\Delta_{tan} = 49\%$.

Furthermore, it was attempted to achieve phase-pure forsterite by varying the solid content of the $MeOMgOCO_2Me$ precursor from 1.5 to 3.1 mass%. However, the replicas obtained from this series only contained mixtures of SiO_2, $MgSiO_3$ and Mg_2SiO_4 when the solid content of methoxymagnesium methyl carbonate was between 1.5 and 2.2 mass%, and mixtures of $MgSiO_3$, Mg_2SiO_4 and MgO for the higher solid contents.

2.8 Compressive strength in comparison

The $Mg_2SiO_4/MgSiO_3$ replica obtained from five times infiltration with $MeOMgOCO_2Me$ (solid content 0.9 mass%), subsequent immersion in TEOS solution and calcination at 1350°C for 5 h (see Section 2.7) exhibited a compressive strength (31 ± 8 MPa) which was three times higher than that of a silica replica prepared according to the literature [11] (Fig. 4d).

2.9 BET surface area of forsterite replica

Using nitrogen sorption and evaluation via the BET method, a specific surface area of 0.4 $m^2 \cdot g^{-1}$ was determined for the $Mg_2SiO_4/MgSiO_3$ replica obtained from five infiltrations with $MeOMgOCO_2Me$ (solid content 0.9 mass%), subsequent immersion in TEOS solution and calcination at 1350°C for 5 h (see Section 2.7). This replica was selected because it presented the highest compressive strength. It is expected that the thermal conductivity of this material would be larger than that of aerogels, since its specific surface area is significantly lower. Its average pore size is therefore higher than those reported for aerogels, whose specific surface areas lie between 45 and 200 $m^2 \cdot g^{-1}$ [16, 17, 35]. Nevertheless, the result suggests that the replicas produced here possess sufficient porosity to be useful as carriers for drugs or sensors, and to a minor extent as insulating material in construction applications.

3 Conclusion

Our study has demonstrated that $Mg(OCOOCH_3)(OCH_3)$ presents a suitable precursor which can penetrate wood cell walls and spread through the cell walls as confirmed by EDS mapping. The macroscopic and submicron scale structures of the wood template are replicated. When more infiltration steps are applied, then a higher amount of magnesium is found in the cell walls and less shrinkage of the replicas occurs. All MgO replicas exhibit poor mechanical stability.

Figure 6 presents the different magnesium-based porous replicas obtained and their properties with respect to the quality of replication and mechanical stability as a function of the specific treatment conditions.

The mechanical stability of the replicas can be improved by subsequent treatment with TEOS solution which results in the formation of a coating comprised of

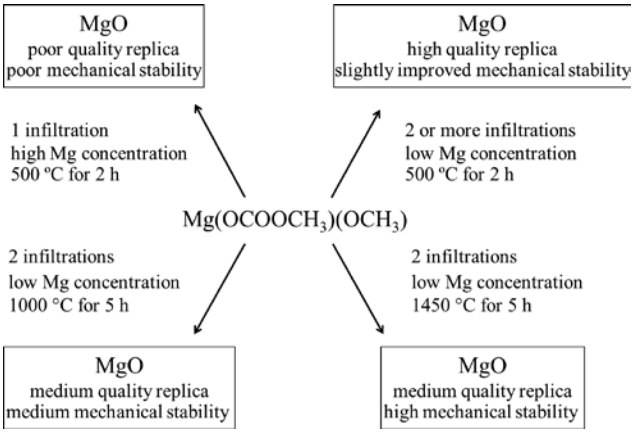

Fig. 6: Overview of different MgO replicas of wood achieved under various treatment conditions with methoxymagnesium methyl carbonate precursor solution.

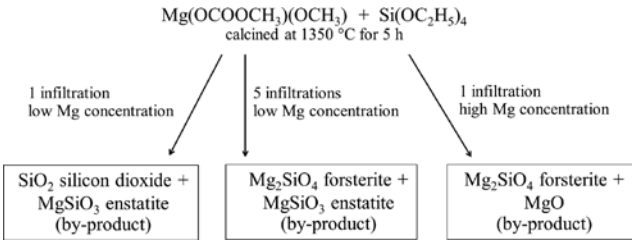

Fig. 7: Summary of the mechanically more stable replicas containing different magnesium silicates.

magnesium silicates (forsterite or enstatite). Depending on the amount of magnesium precursor and TEOS solution applied, different mixtures of magnesium silicates, SiO_2 or MgO are obtained, as presented in Fig. 7. All these products show high compressive strength.

In further experiments, deposition of calcium silicate hydrates, so-called C–S–H (the main constituent of hydrated Portland cement) on the MgO framework should be studied with the aim to achieve exceptional mechanical stability of the replicas.

4 Experimental section

4.1 Preparation of the template

Sections (either cubes with side lengths of 1 cm or radial thin discs of 1 cm (tangential and radial) in diameter and 0.3 mm (axial) in thickness) were cut from the sapwood of pine trees (*Pinus sylvestris*), weighed and subjected to a series of chemical treatments. In a first step, 150 g of wood was washed by extraction first for 6 h each in a Soxhlet apparatus using 500 mL of a 2:1 by weight mixture of toluene and ethanol and then the same amount of pure ethanol. All samples were stored in ethanol between the processing steps to prevent drying. For preparation of the templates, 1 g of this wood was placed in an oxidizing solution containing 1.4 g of sodium chlorite ($NaClO_2$) and 0.5 g of acetic acid in 23.1 g of deionized water. Delignification was carried out twice at 70°C for 3 h each whereby the delignification solution was renewed after the initial 3 h. Afterwards, a mild vacuum from a water-jet pump was applied for half an hour. Following the delignification treatment, the templates were immediately extracted with ethanol to remove any residual solutions of reagents [9].

4.2 Infiltration

Magnesium metal in the amount of 2.5 g (0.1029 mol) for high solid content, or 0.5 g (0.0206 mol) for low solid content, was dissolved in 250 mL absolute methanol (dried and stored over molecular sieve, 3 nm) and heated to 65°C to produce a clear solution of $Mg(OCH_3)_2$. After 90 min of stirring at room temperature, carbon dioxide gas was bubbled through the $Mg(OCH_3)_2$ solution. A turbid solution of $MeOMgOCO_2Me$ had formed which was then centrifuged. The clear solution (~13 g of either 4.9 or 0.9 mass% solid content) was rinsed into a vial containing the pine wood template. Infiltration of the wood cells occurred during the drying process at 70°C. The infiltrated wood template was then kept in an oven at 80°C for 7 h.

4.3 Calcination

To achieve MgO replicas, calcination was performed at various conditions, namely at 500°C for 2 h and at 1450°C for 5 h at a heating rate of 1 $K \cdot min^{-1}$ with holding steps of 0.5 h each at 200, 330 and 470°C. Immediately after infiltration, hydrolysis of $MeOMgOCO_2Me$ with residual moisture from the wood template occurred and an $MgCO_3$ sol formed.

The magnesium silicate replicas were synthesized using the magnesium infiltrated templates which were further soaked once with a TEOS solution (1 g TEOS in 8 g EtOH). The infiltrated wood template was then kept in an oven at 80°C for 7 h and subsequently calcined at 1350°C for 5 h at a heating rate of 1 $K \cdot min^{-1}$. Additional calcination experiments were performed at 200, 330 and 470°C for 0.5 h each and at 600°C for 3 h.

4.4 Analysis

The methoxymagnesium methylcarbonate precursor solution was assessed via dynamic light scattering (DLS) using a Zetasizer Nano ZS apparatus (Malvern Instruments, Workestershire, UK). SEM images of the products obtained from calcination were captured using an XL30 ESEM FEG instrument (Philips/FEI Company, Eindhoven, The Netherlands) equipped with an energy-dispersive X-ray detector (EDX) for elemental analysis (New XL30, EDAX Inc., Mahwah, NJ, USA). The magnesium oxide contained in the replica was identified via X-ray diffraction (D8 advance instrument, Bruker AXS, Bruker, Karlsruhe, Germany). The specific surface area (BET method, N_2) was measured on a Nova 4000e instrument from Quantachrome (Boynton Beach, FL, USA) utilizing a sample degassed for 2 h at 200°C. Additionally, the forsterite polymorph contained in the replicas was identified by ^{29}Si solid state MAS NMR spectroscopy (Bruker).

Mechanical testing was carried out in plate-plate compression geometry adapted from DIN/EN/ISO-844 on a smarTens010 universal testing machine (Karg Industrietechnik, Krailing, Germany). The plate size was reduced to 4 cm^2 to account for our small sample sizes. Each measurement was repeated three times and the values reported for the compressive strength samples represent the average.

Acknowledgment: The authors gratefully acknowledge financial support by the German Research Foundation (Deutsche Forschungsgemeinschaft, DFG) within the framework of the priority program SPP 1420.

References

[1] K. Raed, U. Gross, *Int. J. Thermophys.* **2009**, *30*, 1343.
[2] S. S. Kistler, *Nature* **1931**, *127*, 741.
[3] S. S. Kistler, *J. Phys. Chem.* **1932**, *36*, 52.
[4] Z. Wang, Z. Pan, *Appl. Surf. Sci.* **2015**, *356*, 1168.
[5] A. D. C. Permana, A. Nugroho, K. Y. Chung, W. Chang, J. Kim, *Chem. Eng. J.* **2014**, *241*, 216.
[6] P. Fratzl, R. Weinkamer, *Pro. Mater. Sci.* **2007**, *52*, 1263.
[7] D. Fengel, G. Wegener, A. Greune, *Wood Sci. Technol.* **1989**, *23*, 123.
[8] H. F. Jacob, D. Fengel, S. E. Tschegg, P. Fratzl, *Macromolecules* **1995**, *28*, 8782.
[9] P. A. Ahlgren, W. Q. Yean, D. A. I. Goring, *Tappi J.* **1971**, *54*, 737.
[10] L. Sapei, R. Nöske, P. Strauch, O. Paris, *Chem. Mater.* **2008**, *20*, 2020.
[11] D. Van Opdenbosch, G. Fritz-Popovski, O. Paris, C. Zollfrank, *J. Mater. Res.* **2011**, *26*, 1193.
[12] G. Fritz-Popovski, D. Van Opdenbosch, C. Zollfrank, B. Aichmayer, O. Paris, *Adv. Funct. Mater.* **2013**, *23*, 1265.
[13] D. Van Opdenbosch, M. H. Kostova, S. Gruber, S. Krolikowski, P. Greil, C. Zollfrank, *Wood Sci. Technol.* **2010**, *44*, 547.
[14] M. H. Kostova, M. Batentschuk, F. Goetz-Neunhoeffer, S. Gruber, A. Winnacker, P. Greil P, C. Zollfrank, *Mater. Chem. Phys.* **2010**, *123*, 166.
[15] M. H. Kostova, C. Zollfrank, M. Batentschuk, F. Goetz-Neunhoeffer, A. Winnacker, P. Greil, *Adv. Funct. Mater.* **2009**, *19*, 599.
[16] T. Kornprobst, J. Plank, *GDCh-Monographie: Tagung Bauchemie* **2010**, *42*, 121.
[17] J. Plank, H. Hoffmann, J. Schölkopf, W. Seidl, I. Zeitler, Z. Zhang, *Res. Lett. Mater. Sci.* **2009**, *2009*, 1.
[18] T. Kornprobst, J. Plank, *J. Non-Cryst. Solids* **2013**, *361*, 100.
[19] A. Kosak, A. Lobnik, *Int. J. Appl. Ceram. Technol.* **2015**, *12*, 461.
[20] J. Ita, L. Stixrude, *J. Geophys. Res.* **1992**, *97*, 6849.
[21] S. Ramesh, A. Yaghoubi, K. Y. Sara Lee, K. M. Christopher Chin, J. Purbolaksono, M. Hamdi, M. A. Hassan, *J. Mech. Behav. Biomed. Mater.* **2013**, *25*, 63.
[22] S. Ni, L. Chou, J. Chang, *Ceram. Int.* **2007**, *33*, 83.
[23] M. Kharaziha, M. H. Fathi, *Ceram. Int.* **2009**, *35*, 2449.
[24] M. Kharaziha, M. H. Fathi, *J. Mech. Behav. Biomed. Mater.* **2010**, *3*, 530.
[25] C. Y. Tan, R. Singh, Y. C. Teh, Y. M. Tan, *Int. J. Appl. Ceram. Technol.* **2015**, *12*, 437.
[26] S. Klaithong, D. Van Opdenbosch, C. Zollfrank, J. Plank, *Z. Naturforsch.* **2013**, *68b*, 533.
[27] V. Merk, M. Chanana, T. Keplinger, S. Gaan, I. Burgert, *Green Chem.* **2015**, *17*, 1423.
[28] H. D. Lutz, *Z. Anorg. Allg. Chem.* **1967**, *353*, 207.
[29] H. Thoms, M. Epple, H. Viebrock, A. Reller, *J. Mater. Chem.* **1995**, *5*, 589.
[30] H. L. Finkbeiner, M. Stiles, *J. Am. Chem. Soc.* **1963**, *85*, 616.
[31] K. X. Song, X. M. Chen, X. C. Fan, *J. Am. Ceram. Soc.* **2007**, *90*, 1808.
[32] J. F. Stebbins, W. R. Panero, J. R. Smyth, D. J. Frost, *Am. Mineral.* **2009**, *94*, 626.
[33] J. F. Stebbins in *Mineral Physics and Crystallography: A Handbook of Physical Constants*, Vol. 2 (Ed.: T. J. Ahrens), American Geophysical Union, Washington, DC, **1995**, p. 303.
[34] J. M. Griffin, S. E. Ashbrook, *Annu. Rep. NMR Spectrosc.* **2013**, *79*, 241.
[35] H. Zheng, C. Gao, S. Che, *Micropor. Mesopor. Mater.* **2008**, *116*, 299.

6.3 Further results: Calcium silicate hydrate replicas

Calcium silicate hydrates are the main binding phases in hydrated Portland cement [75-77]. In order to produce wood replicas with high mechanical stability, this material was considered. Since the reaction between calcium di(methylcarbonate) and the TEOS precursor must take place inside the wood cell walls, the precursors which react immediately and precipitate outside the cell walls cannot be used. For this reason, the common precipitation reaction between a sodium silicate ($Na_2SiO_3 \cdot 5H_2O$) solution and a calcium nitrate ($Ca(NO_3)_2 \cdot 4H_2O$) solution [77] cannot infiltrate into the wood cell walls. However, a viable method includes to synthesize the calcium silicate hydrate on the surface of the silica replica.

6.3.1 Ionization of the surface of the silica replica

Firstly, the surface OH groups of silica replica need to be partially ionized in basic solution to generate negatively charged SiO^- anionic sites (**Equations (47), (48)**) [35, 103]. Subsequent immersion in the calcium hydroxide or calcium chloride precursor solution was hoped to yield calcium silicate hydrate on the silica replica surface, according to **Equation (49)**.

$$Si(OH)_4 + OH^- \rightarrow (HO)_3SiO^- + H_2O \qquad \textbf{Equation (47)}$$

$$(HO)_3SiO^- + OH^- \rightarrow (HO)_2SiO_2^{2-} \qquad \textbf{Equation (48)}$$

$$Ca^{2+} + H_2SiO_4^{2-} + 2\,H_2O \rightarrow CaH_2SiO_4 \cdot 2\,H_2O \qquad \textbf{Equation (49)}$$

According to the Pozzolanic reaction, it is possible to synthesize calcium silicate hydrate from silicic acid by using $Ca(OH)_2$ as a precursor [104, 105], as is presented in **Equation (50)**.

$$Ca(OH)_2 + H_4SiO_4 \rightarrow Ca_2H_2SiO_4 + 2H_2O \rightarrow CaH_2SiO_4 \cdot 2\,H_2O \qquad \textbf{Equation (50)}$$

6.3.2 Effect of ionization time

The silica replicas prepared after [8] were immersed in a basic solution (NH_4OH solution at pH ~11.3) for 10 min or 1 h. After that, the activated replicas were washed with deionized

water and immersed in a $CaCl_2$ solution (0.07 molar) for 1 or 66 h for the samples immersed 10 min in basic solution, and 1 or 18 h for the samples immersed 1 h in the basic solution, respectively. The replicas were later washed with deionized water and immersed in acetone to stop the hydration reaction and kept in an oven at 50 °C for 24 h.

All samples show a rough surface like in the original silica replicas (**Figure 50**), except that the sample with 10 min soaking in the basic solution and 66 h immersion in the $CaCl_2$ solution exhibits a foil-like structure on some areas of the surface, as is shown in an SEM image (**Figure 51**). It was concluded that 10 min immersion time in the basic solution is enough to ionize the silica surface.

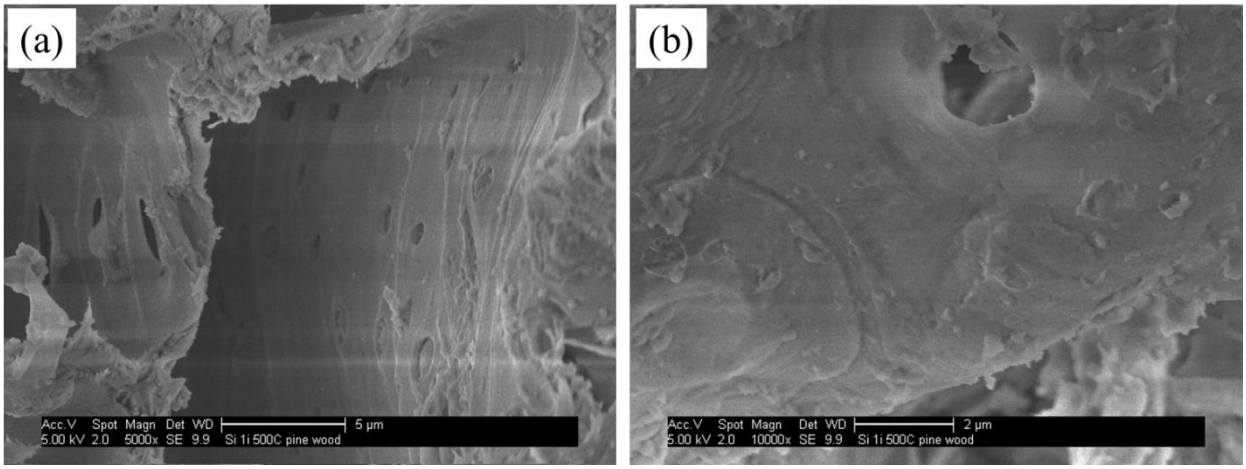

Figure 50. SEM image of the silica replica prepared by one infiltration with TEOS in ethanol and subsequent calcination at 500 °C for 2 h.

6.3.3 Effect of Precursor, Immersion Time and pH

Silica replicas with ionized surface (10 min immersion in NaOH solution at pH 13) were immersed in 3 different precursor conditions:

1) saturated $Ca(OH)_2$ solution

2) 0.68 molar $CaCl_2$ solution (pH = 5.2)

3) 0.68 molar $CaCl_2$ solution (pH = 13)

The immersion times of all pretreated silica replicas were varied between 2, 24 and 72 h (**Table 1 (a)-(l)**). The replicas were later washed with deionized water and immersed in acetone to stop the hydration reaction, and kept in an oven at 50 °C for 24 h.

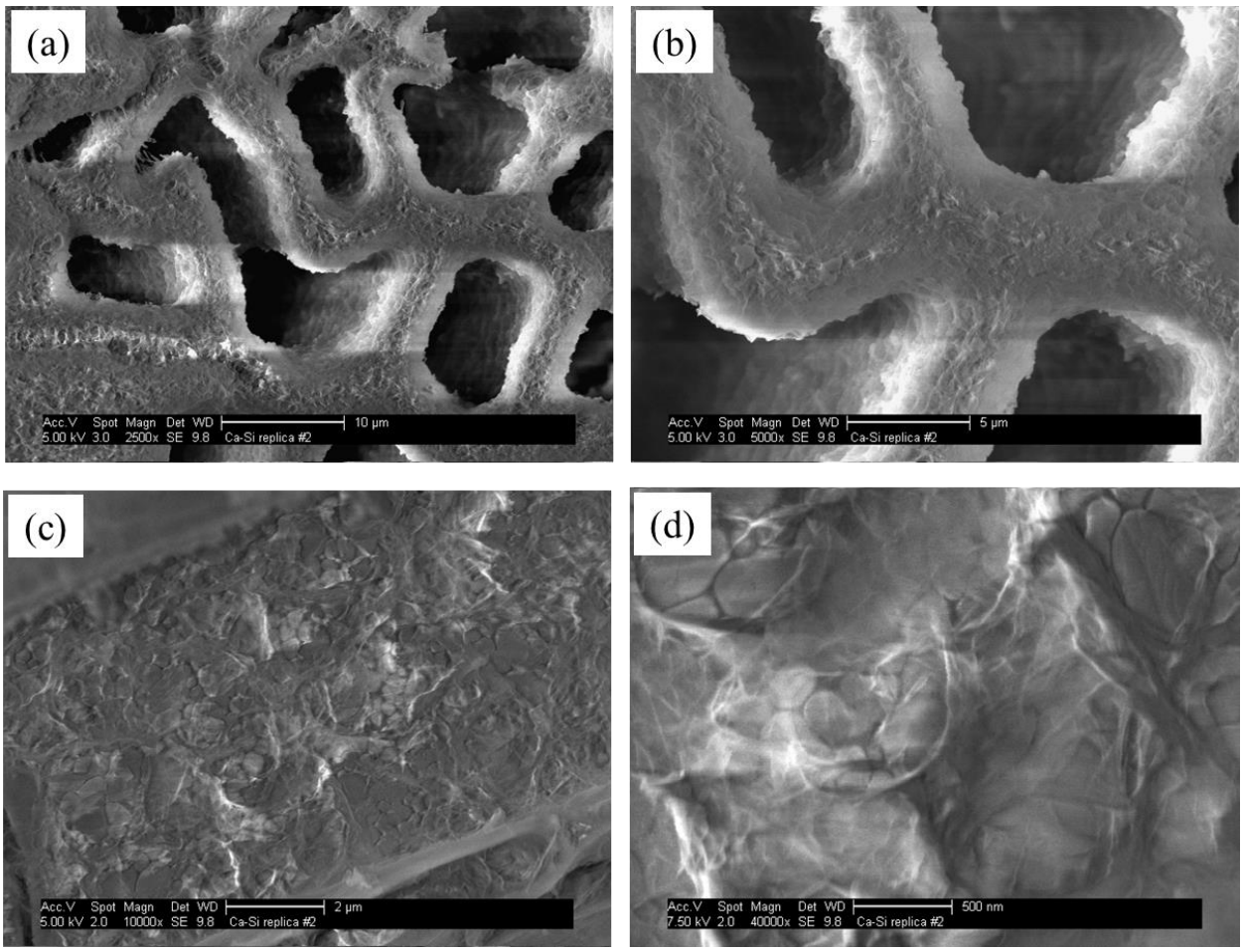

Figure 51. SEM images of a Si-Ca replica (10 min in basic solution and 66 h in $CaCl_2$ solution); (a), (b): cross section shows foil-like structure on the surface of honeycombs; (c), (d) on the a surface of tracheid.

SEM images of the samples with 2 h immersion time in all three precursor solutions do not show the characteristic foil-like structure of C-S-H (**Figure 52**). XRD patterns of all samples

(**Figure 53 (a)-(c)**) show an amorphous silica replica with undefined peaks for the sample with 2 h immersion time in $CaCl_2$ solution at pH 5.2 (**Figure 53 (b)**) and with the characteristic peaks of NaCl in the sample with 2 h immersion time in $CaCl_2$ solution at pH 13 (**Figure 53 (c)**).

All samples with 24 h immersion time in both precursor solutions provide similar results as the samples with 2 h immersion time. There is no foil-like structure of C-S-H on their surface detectable, as is demonstrated by SEM in **Figure 54**. XRD patterns of all samples (**Figure 53 (d)-(f)**) show only amorphous silica except for the sample with 24 h immersion time in $CaCl_2$ solution at pH 13 which shows amorphous silica and the characteristic peaks of NaCl (**Figure 53 (f)**).

Table 1. Silica replicas obtained from 3 precursor solutions at various immersion times.

Sample	***In $Ca(OH)_2$**	****In $CaCl_2$ pH = 5.2**	*****In $CaCl_2$ pH = 13**
(a)	2 h		
(b)		2 h	
(c)			2h
(d)	24 h		
(e)		24 h	
(f)			24 h
(g)	72 h		
(h)		72 h	
(i)			72 h
(j)	24 h x 3		
(k)		24 h x 3	
(l)			24 h x 3

* Saturated solution (very low solubility),

** $[CaCl_2]$ = 0.68 molar

*** The colorless solution of $CaCl_2$ turns turbid and white when the pH was adjusted to basic solution (pH around 11), indicating precipitation of $Ca(OH)_2$.

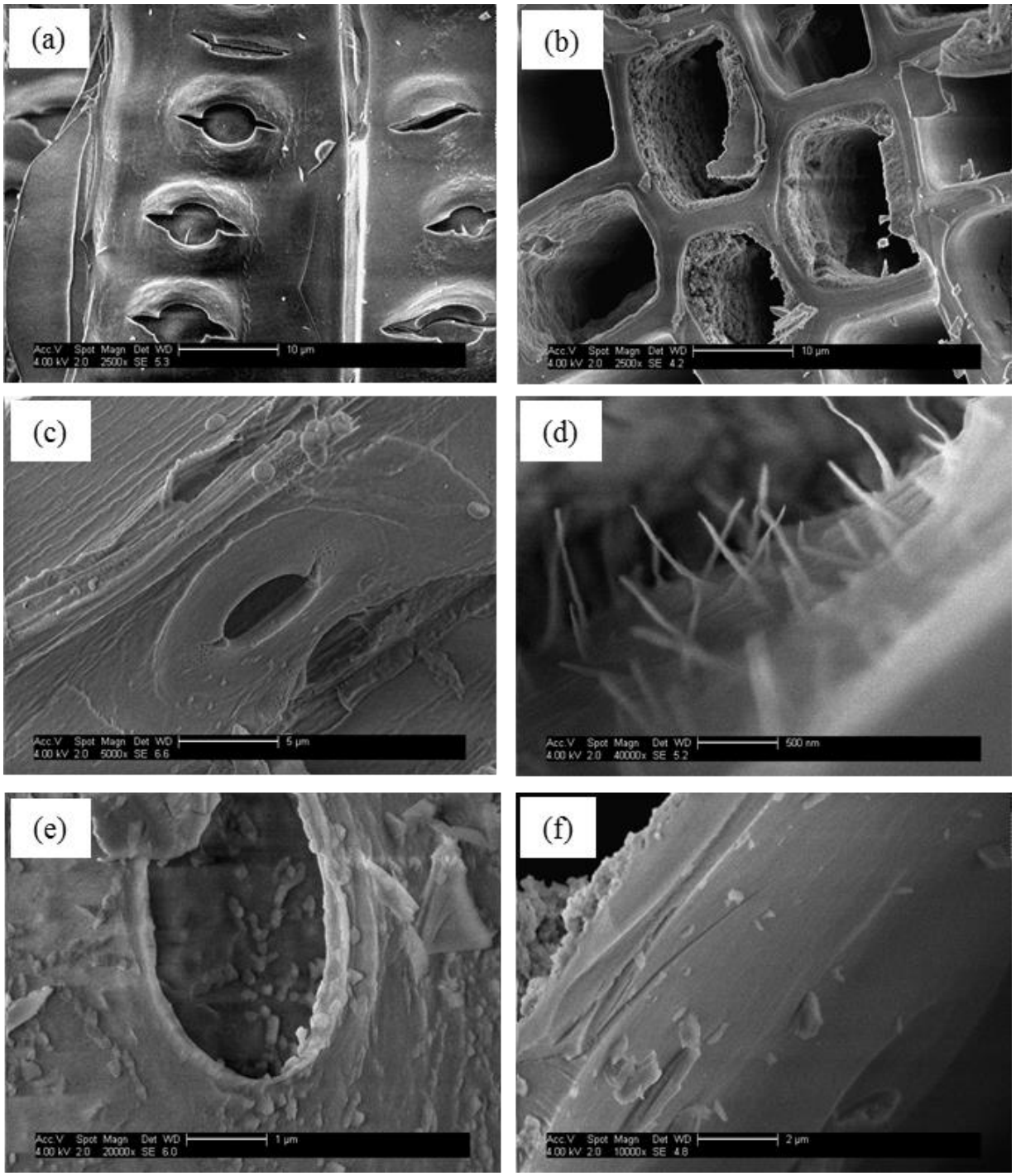

Figure 52. Surface-treated silica replicas immersed for 2 h (a), (b) in $Ca(OH)_2$ solution; (c), (d) in $CaCl_2$ solution at pH = 5.2; and (e), (f) in $CaCl_2$ solution at pH = 13.

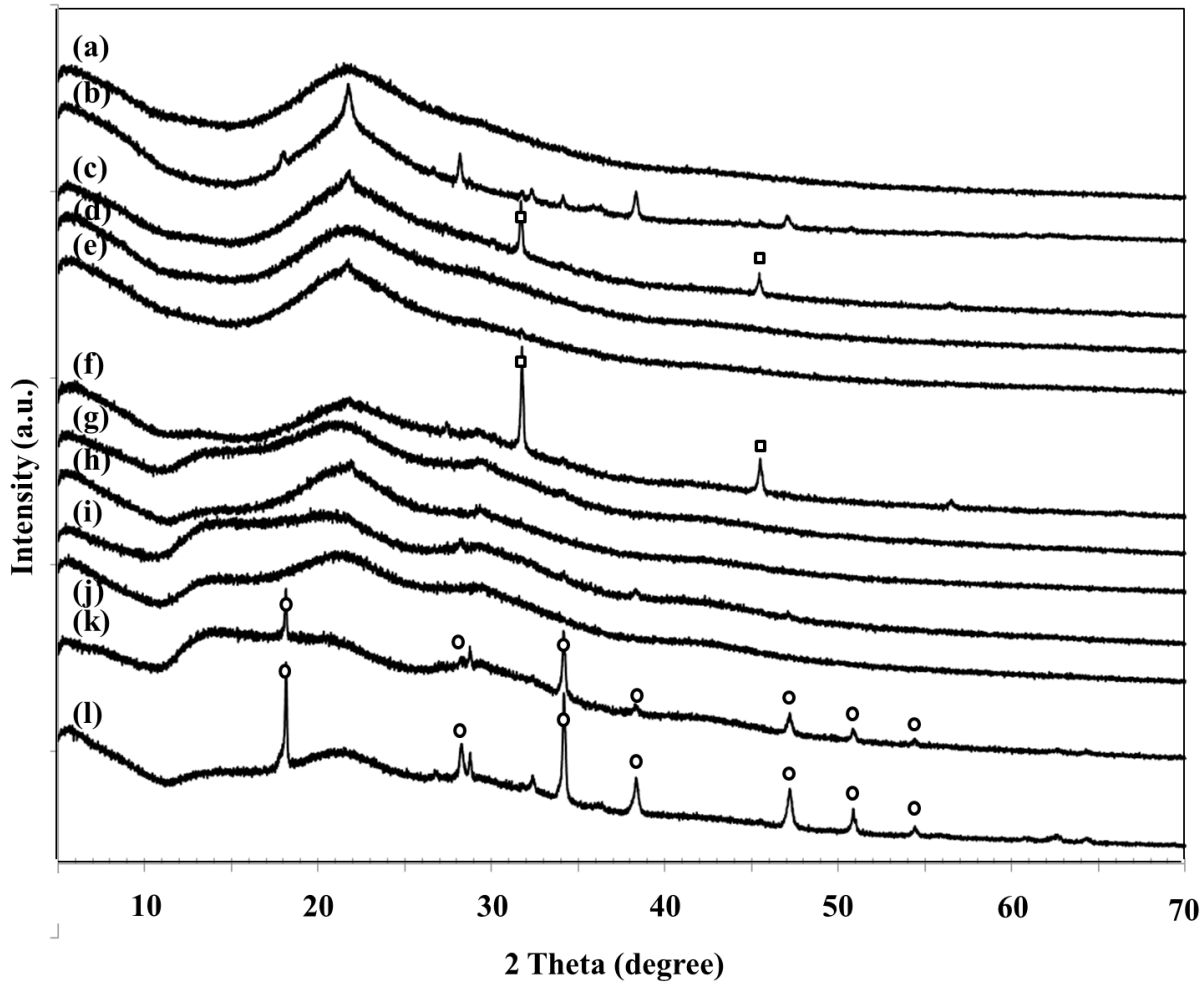

Figure 53. XRD patterns of surface-treated silica replicas obtained from 3 different precursor solutions at various immersion times according to **Table 1.** □ = NaCl (JCPDS 5-0628), ○ = C-S-H phase at high Ca/Si ratio (Ca/Si = 3) according to [79].

The immersion time in saturated $Ca(OH)_2$ solution, 0.68 molar $CaCl_2$ solution (pH = 5.2) and 0.68 molar $CaCl_2$ solution (pH = 13) were then increased up to 72 h. At this long immersion time, the foil-like structure of C-S-H is successfully formed on the surfaces of all three samples from various precursor solutions, as is shown on the SEM images in **Figure 55**. Moreover, the XRD patterns of all samples show amorphous silica which is characteristic for C-S-H (**Figure 53 (g)-(i)**).

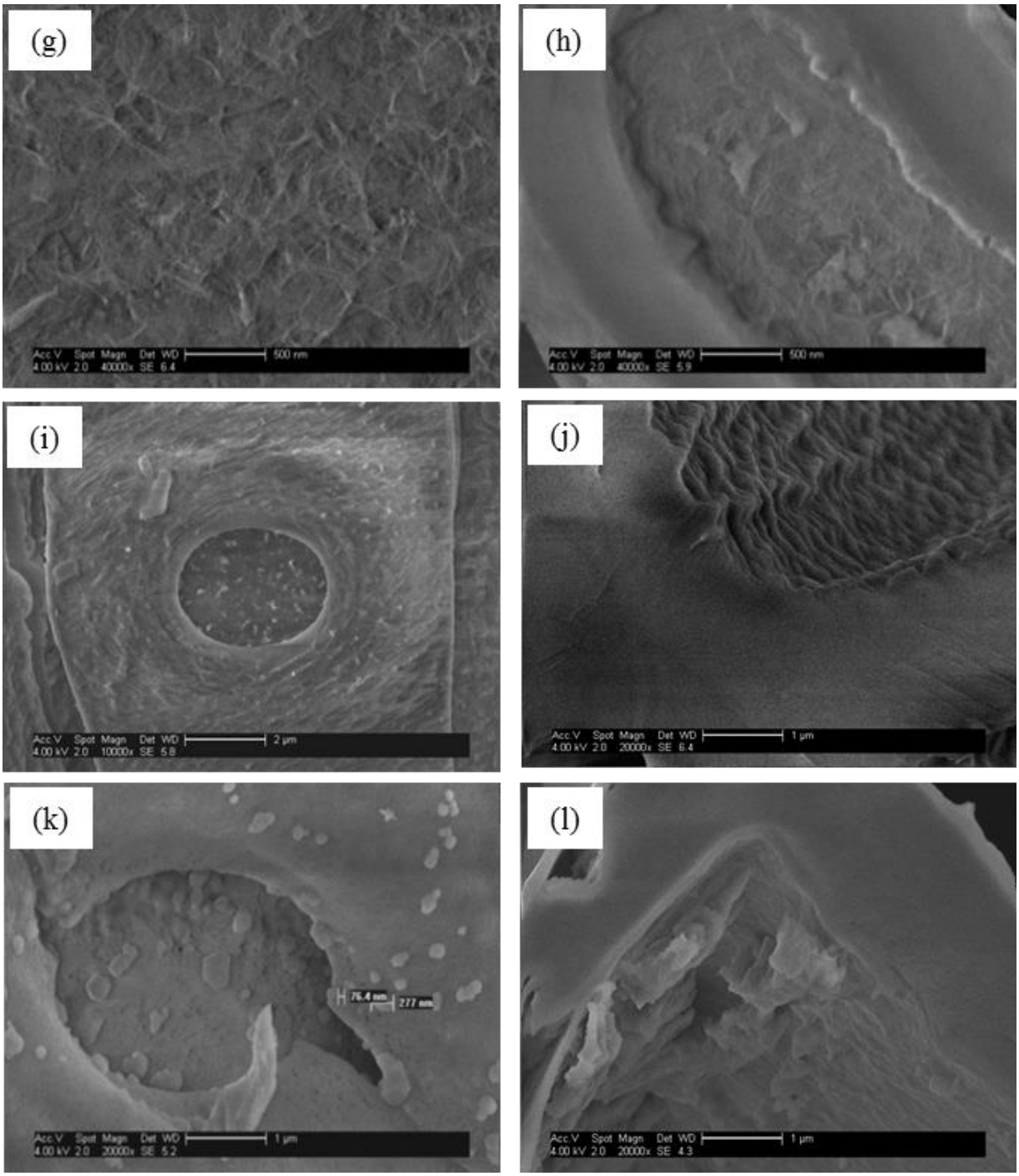

Figure 54. Surface-treated silica replicas immersed for 24 h (g), (h) in $Ca(OH)_2$ solution; (i), (j) in $CaCl_2$ solution at pH = 5.2; and (k), (l) in $CaCl_2$ solution at pH = 13.

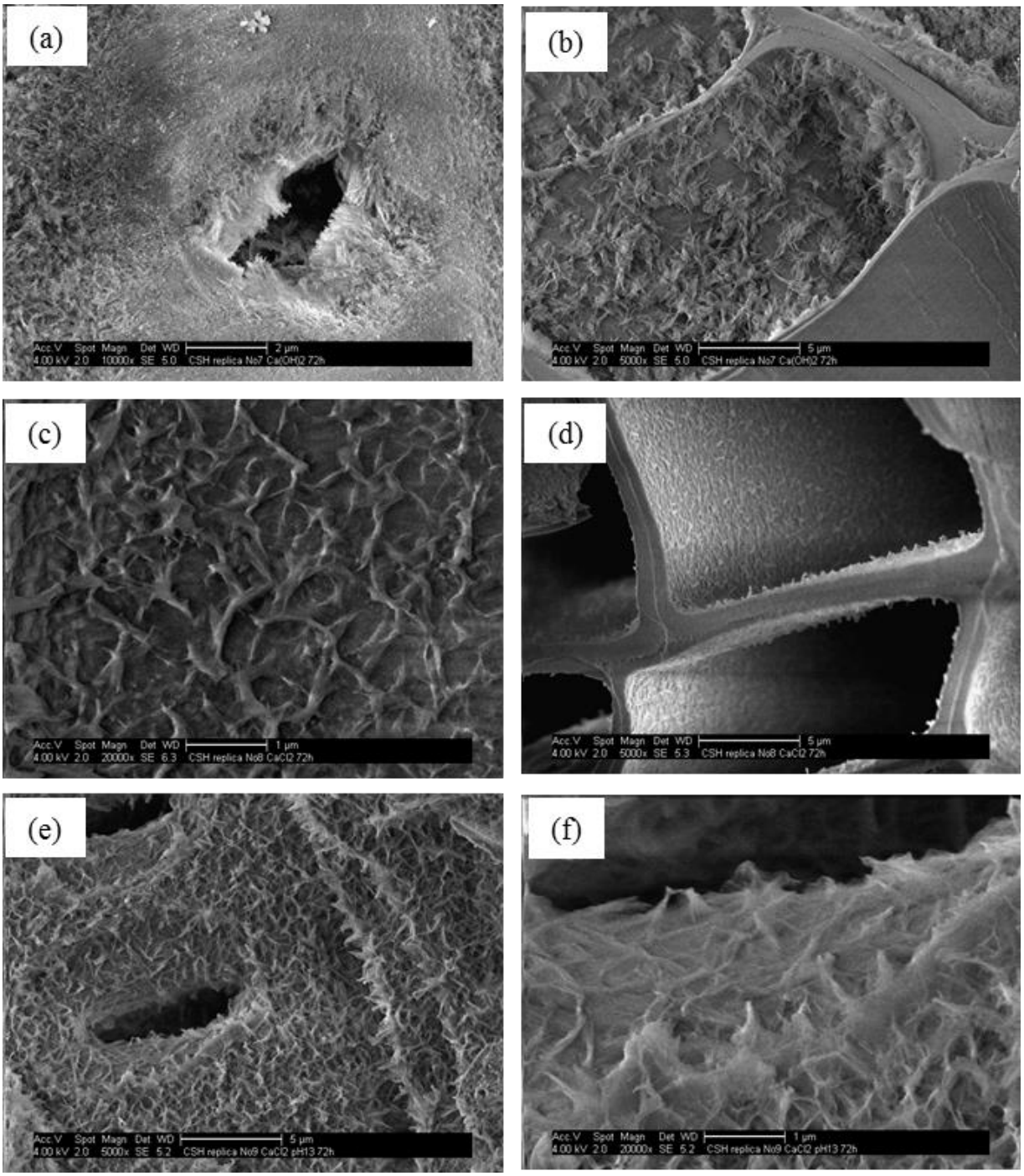

Figure 55. Surface-treated silica replicas immersed for 72 h (a), (b) in $Ca(OH)_2$ solution; (c), (d) in $CaCl_2$ solution at pH = 5.2; and (e), (f) in $CaCl_2$ solution at pH 13.

6.3.4 Effect of the amount of calcium ions present in calcium precursors

During the immersion process of the surface-treated silica replica in the calcium precursor, calcium ions from in the calcium precursor solution interact with the negatively charged sites on the activated surface of the silica replica to form C-S-H phase. Even longer immersion times may not be sufficient to form a thick layer of C-S-H, because there are no more free calcium ions available in the calcium precursor solution for further reaction. To prove this assumption, immersion in various calcium precursor solutions was performed for 24 h with 3 cycles by using fresh solutions in each cycle.

SEM images of all samples show the characteristic foil-like structured C-S-H (**Figure 56**). However the XRD pattern of the sample immersed in $Ca(OH)_2$ solution show only amorphous silica, as is evidenced in **Figure 53 (j)**. At some areas on the surfaces of the samples prepared by immersion in $CaCl_2$ solution at both pH = 5.2 and 13, the fibrillar morphology of C-S-H which is characteristic for high Ca/Si ratios was observed [82]. These results are supported by the XRD patterns which show the characteristic peaks of C-S-H at high Ca/Si ratio (Ca/Si = 3) [80].

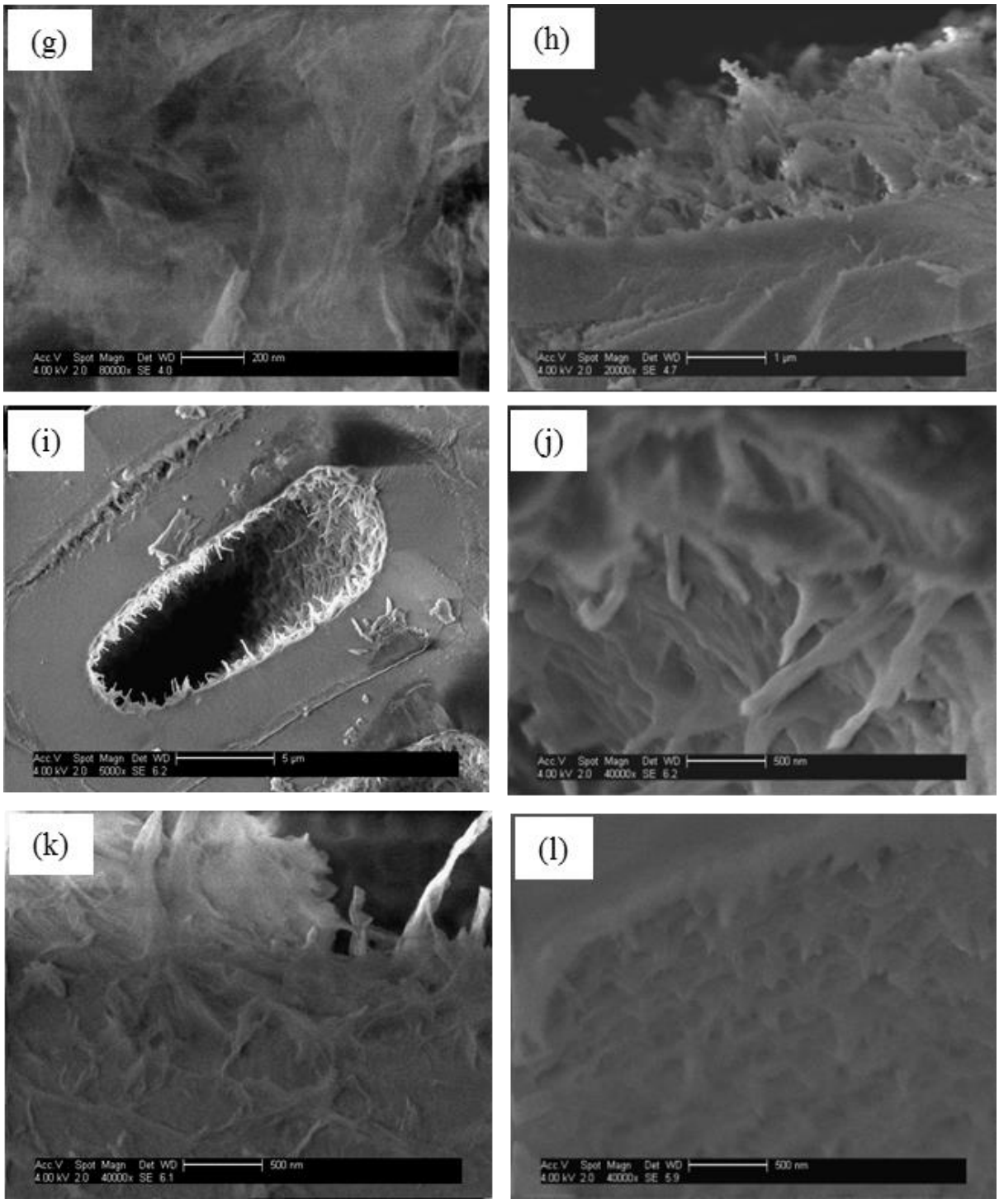

Figure 56. Surface-treated silica replicas immersed over 24 h for 3 cycles (g), (h) in $Ca(OH)_2$ solution; (i), (j) in $CaCl_2$ solution at pH = 5.2; (k), (l) and in $CaCl_2$ solution at pH = 13.

6.3.5 FTIR spectra

From IR spectra of all samples (**Figure 57**), only the specimens with 24 h immersion time and for 3 cycles in $CaCl_2$ solution at both pH = 5.2 and 13 show an absorption band at wave number of ~ 660-670 cm^{-1} corresponding to a characteristic absorption band of C-S-H stemming from Si-O-Si bending (**Figure 57 (k) and 57 (l)**) [106]. This absorption band is stronger in the sample with 24 h immersion time and 3 cycles in $CaCl_2$ solution at pH = 13 (**Figure 57 (l)**). The other absorption bands correspond to amorphous silica [107].

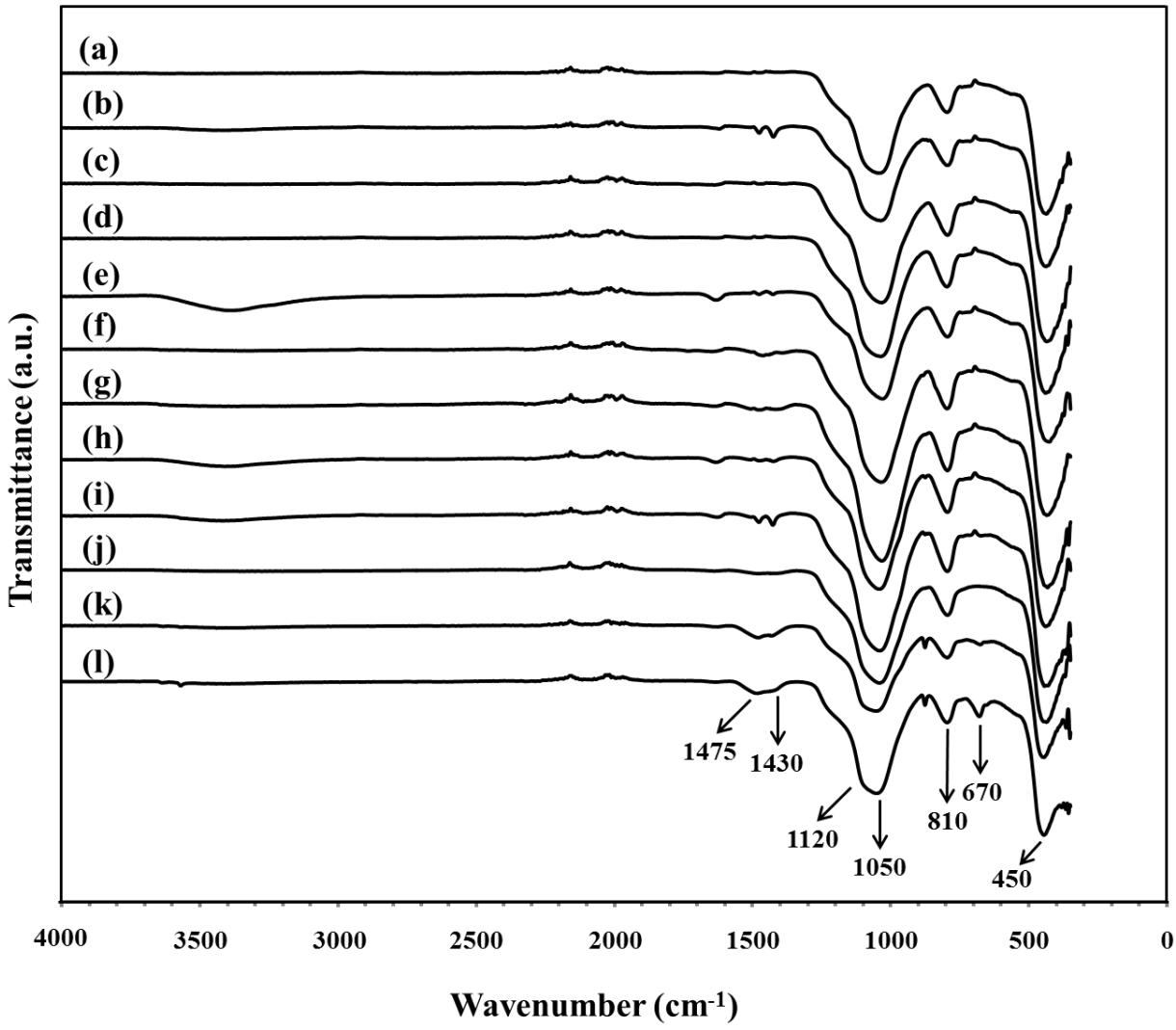

Figure 57. IR spectra of surface-treated silica replicas immersed in 3 different precursor solutions with various immersion times according to **Table 1.**

6.3.6 EDX analysis

Energy dispersive X-ray spectroscopy was performed in order to investigate the calcium and silicon content on the surface of the replica prepared by 24 h immersion time and 3 cycles in $CaCl_2$ solution at pH = 13. This sample showed most abundant foil-like structure.

The results from many detection spots show that this material is heterogeneous, since there are different contents of Ca and Si on each area (**Figure 58**). There is a low content of Ca on the thin layer of the foil-like C-S-H, while there is higher Ca content on the thick layer.

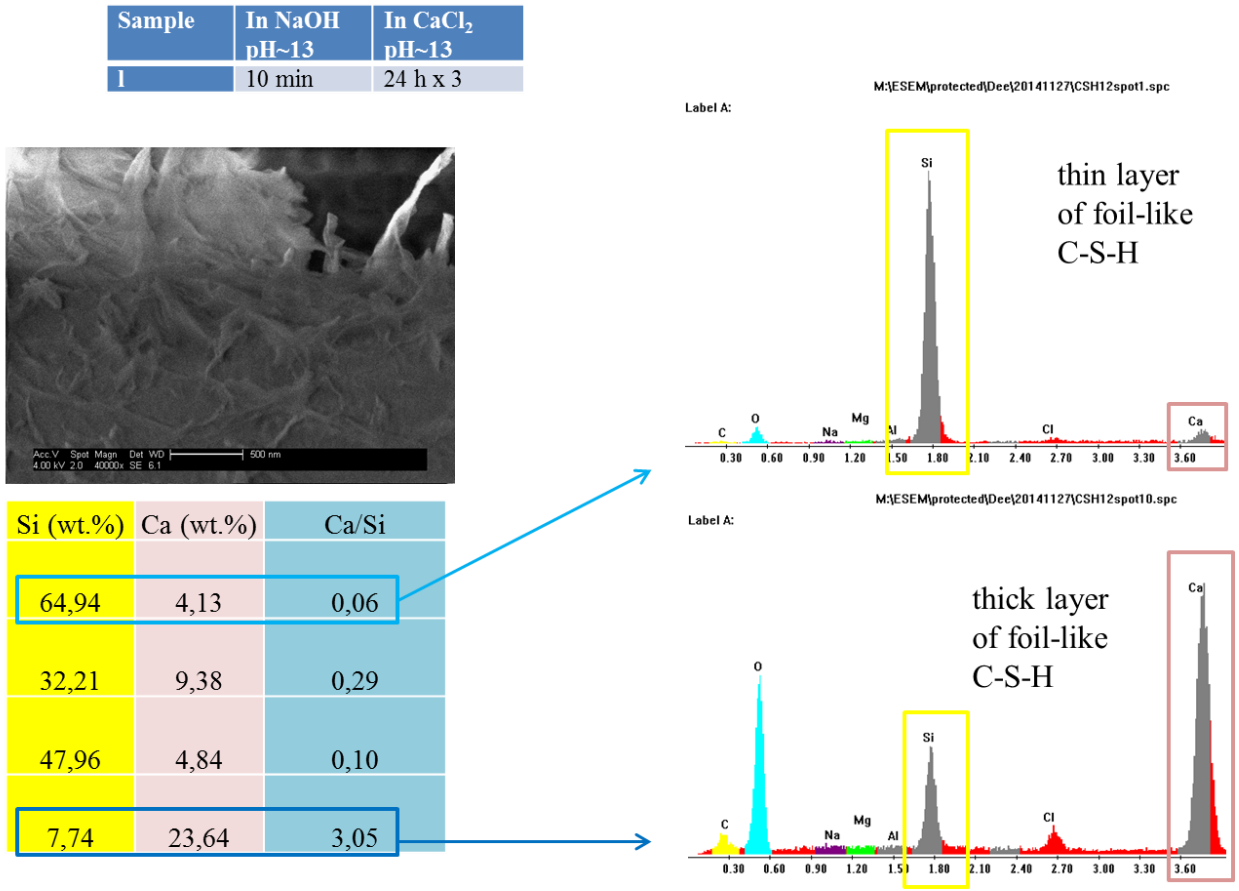

Figure 58. EDX spectra from different spots on the surface of the replica prepared by 24 h immersion for 3 cycles in $CaCl_2$ solution at pH = 13.

7 Conclusions and outlook

7.1 Conclusions

This research work focused on the replication of soft wood by using alkaline earth metal carbonate and silicate as precursors for the final replicas.

$CaCO_3$ replicas were successfully synthesized by using a solution of $Ca(OCOOCH_3)_2$ as precursor. Different qualities of replication and material properties were obtained depending on the conditions of the infiltration and calcination. More infiltration steps allow more calcium precursor to penetrate into the wood cell walls, thus leading to a more dense assembly of $CaCO_3$ after calcination. However, by increasing the number of infiltrations, the mechanical stability of the replicas improved only slightly. The calcination temperature also affects the type of polymorph and morphology of the replica. Calcination at low temperature (350 °C/ 48 h) leads to the meta-stable $CaCO_3$ polymorph vaterite while a higher calcination temperature (500 °C/ 2 h) results in the polymorph calcite. A mechanically more robust CaO replica can be obtained when the calcination temperature is at ~ 900 °C. An almost monolithic replica can be obtained from repeated infiltration (5 times) in combination with high temperature calcination (900 °C). All replicas obtained from this process involving calcium di(methylcarbonate) exhibit a relatively low specific surface area and are therefore inferior to aerogels with respect to thermal insulation.

The second type of replicas were successfully synthesized by using $Mg(OCOOCH_3)(OCH_3)$ precursor solution. Compared to the calcium precursor, this precursor can penetrate wood cell walls more effectively and spread through the entire cell walls as confirmed by EDX mapping. After high temperature treatment, the macroscopic and submicron scale structures of the wood template were replicated in high quality as MgO. Repeated infiltration at low precursor concentrations was found to be best suitable to achieve precise replicas. The specific treatment conditions play an important role relative to the quality of the replication and the mechanical stability of the replicas. Calcination at 1450 °C produced highly annealed MgO particles with high particle compaction and superior mechanical stability compared to the sample calcined at 500 °C. Unfortunately, at this calcination temperature an extremely high shrinkage value of Δ_{ax} = 56% was observed.

The mechanical stability of the MgO replicas can be improved substantially by subsequent treatment of the magnesium infiltrated templates with TEOS solution. This method results in the formation of a coating comprised of magnesium silicates (forsterite or enstatite) on the MgO replica. Different mixtures from magnesium silicates, SiO_2 or MgO are obtained depending on the amount of magnesium precursor and TEOS solution applied. The magnesium precursor which had penetrated into the wood cell wall reacts with silicate to form magnesium silicate. When there is enough magnesium available, it will react with silicate to form the thermodynamically stable silicate forsterite, Mg_2SiO_4. When the amount of magnesium was understoichiometric, then the product constituted of a mixture of SiO_2 and metastable $MgSiO_3$ (enstatite) as by product. When excess magnesium precursor was present, then only the surface of the magnesium oxide framework which had contact with the silicon precursor TEOS formed Mg_2SiO_4, thus leaving the inside as MgO. All these replicas show high compressive strength.

The last study demonstrated that calcium silicate hydrate (C-S-H) can be deposited on the surface of silica replicas by immersing the silica replicas which were surface activated by treatment with NaOH into a calcium precursor solution (e.g. $CaCl_2$ or $Ca(NO_3)_2$). In this synthesis, the silica surface must first be ionized to generate negatively charged sites which can react with the calcium ions present in the calcium precursor solution. $CaCl_2$ is a suitable calcium precursor for these synthesises, and there must be enough calcium ions available from the solution in order to forming sufficient amounts of C-S-H on the surface of the silica replicas.

This doctoral study attempted to obtain hierarchically structured wood replicas from materials which are held together only through ionic or Van de Waals bonds between particles instead of covalent bonds as in SiO_2, for example by submicron-sized $CaCO_3$ particles in $CaCO_3$ replicas and annealed submicron-sized MgO particles in MgO replicas. Moreover, this work shows that using a combination of different precursors such as in the $Mg_2SiO_4/MgSiO_3$ replicas obtained from infiltration of the wood template with $Mg(OCOOCH_3)(OCH_3)$ solution followed by immersion in TEOS solution leads to an even higher compressive strength than that of silica replicas obtained from infiltrating the wood template with TEOS only.

Another advantage of this two-step synthesis process is that it is possible to prepare mixed replicas as, for example, in $Mg_2SiO_4/MgSiO_3$ replicas or C-S-H grown on a SiO_2 replica, through various combinations of different precursors and different conditions.

7.2 Outlook

Hierarchical porous materials are highly interesting for many applications such as in carriers for drugs, sensors, air filtration, battery, and the most interesting application targeted in this study was as thermal insulating material in construction. The $CaCO_3$, CaO and MgO replicas which were successfully obtained replicate the hierarchical structure of wood from the macroscopic to the submicron scale. However, their poor mechanical strength currently prohibits their use as insulating material in cementitious mixtures. However, high calcination temperature leads to higher mechanical stability, but also to extremely high shrinkage. Therefore, the preparation conditions should be further optimized in order to synthesize replicas with both exceptional mechanical stability and low shrinkage.

The attempt to synthesize a pure phase, thermodynamically stable forsterite, Mg_2SiO_4 replica was not successful. Further experiments should be performed to get a pure phase of this material. More work should be performed to confirm that these magnesium silicates, forsterite and enstatite, form a layer on the MgO framework and to study the mechanism how these phases actually form. It would also be interesting to study the solid structure of the mixed phase material which contains forsterite, enstatite, MgO and SiO_2 at the same time.

Thin layers of C-S-H were formed on the surface of the silica replicas, as evidenced by SEM imaging. Other techniques with high enough resolution or surface techniques such as X-ray photo electron (XPS) spectroscopy should be performed to determine *e.g.* the thickness of the C-S-H layer. In further experiments, formation of a thick layer of C-S-H on the silica replicas should be attempted in order to improve the mechanical stability of the product. Moreover, the Ca/Si ratio of this layer should be determined by EDX.

Nevertheless, the result of this study suggests that the replicas produced here possess sufficient porosity to be useful as carriers for drugs or sensors, and to a minor extent as thermal insulation material in construction applications. Future studies can provide more insight into the actual usefulness of the hierarchically structured and porous replicas produced here.

8 References

[1] C. E. Byrne, D. C. Nagle, Carbonization of wood for advanced materials applications, Carbon 35 (1997) 259-266.

[2] Z. Wang, Z. Pan, Preparation of hierarchical structured nano-sized/porous poly(lacticacid) composite fibrous membranes for air filtration, Appl. Surf. Sci. 356 (2015) 1168-1179.

[3] A. D. C. Permana, A. Nugroho, K. Y. Chung, W. Chang, J. Kim, Template-free synthesis of hierarchical porous anatase TiO_2 microspheres with carbon coating and their electrochemical properties Chem. Eng. J. 241 (2014) 216-227.

[4] N. Hüsing, U. Schubert, Aerogels - airy materials: Chemistry, structure, and properties, Angew. Chem. Int. Ed. 37 (1998) 22-45.

[5] D. Fengel, G. Wegener, Wood: Chemistry, Ultrastructure, Reactions, de Gruyter, Berlin (1989).

[6] H. F. Jacob, D. Fengel, S. E. Tschegg, P. Fratzl, The elementary cellulose fibril in Piecea abies: Comparison of transmission electron microscopy, small-angle X-ray scattering, and wide-angle X-ray scattering results, Macromolecules 28 (1995) 8782-8787.

[7] O. Paris, I. Burgert, P. Fratzl, Biomimetics and biotemplating of natural materials, MRS Bulletin 35 (2010) 219-225.

[8] D. Van Opdenbosch, G. Fritz-Popovski, O. Paris, C. Zollfrank, Silica replication of the hierarchical structure of wood with nanometer precision, J. Mater. Res. 26 (2011) 1193-1202.

[9] P. Fratzl, R. Weinkamer, Nature's hierarchical materials, Pro. Mater. Sci. 52 (2007) 1263-1334.

[10] O. Paris, G. Fritz-Popovski, D. Van Opdenbosch, C. Zollfrank, Recent progress in the replication of hierarchical biology tissues, Adv. Funct. Mater. 23 (2013) 4408-4422.

[11] C. Zollfrank, R. Kladny, H. Sieber, P. Greil, Biomorphous SiOC/C-ceramic composites from chemically modified wood templates, J. Europ.Ceram. Soc. 24 (2004) 479-487.

[12] O. Paris, From diffraction to imaging: New avenues in studying hierarchical biological tissue with x-ray microbeams (Review), Biointerphase, 3 (2008) fb16-fb26.

[13] S. Weiner, H. D. Wagner, The material bone: Structure-mechanical function relations, Annu. Rev. Mater. Sci. 28 **(**1998) 271-298.

[14] P. Fratzl, H. S. Gupta, E. P. Paschalis, P. Roschger, Structure and mechanical quality of the collagen–mineral nano-composite in bone, J. Mater. Chem. 14 (2004) 2115-2123.

[15] J. Qian, J. Wang, G. Qiao, Z. Jin, Preparation of porous SiC ceramic with a woodlike microstructure by sol-gel and carbothermal reduction processing, J. Eur. Ceram. Soc., 24 (2004) 3251-3259.

[16] J. Qian, J. Wang, Z. Jin, Preparation of biomorphic SiC ceramic by carbothermal reduction of oak wood charcoal, Mater. Sci. Eng., A 371 (2004) 229-235.

[17] T. Ota, M. Imaeda, H. Takase, M. Kobayashi, N. Kinoshita, T. Hirashita, H. Miyazaki, Y. Hikichi, Porous titania ceramic prepared by mimicking silicified wood, J. Am. Ceram. Soc. 83 (2000) 1521-1523.

[18] M. H. Kostova, C. Zollfrank, M. Batenschuk, F. Goetz-Neunhoeffer, A. Winnacker, P. Greil, Bioinspired design of $SrAl_2O_4$:Eu^{2+} phosphor, Adv. Funct. Mater. 19 (2009) 599-603.

[19] R. M. Rowell, Handbook of wood chemistry and wood composites, CRC Press, USA (2013).

[20] A. Rafsanjani, M. Stiefel, K. Jefimovs, R. Mokso, D. Derome, J. Carmeliet, Hygroscopic swelling and shrinkage of latewood cell wall micropillars reveal ultrastructural anisotropy, J. R. Soc. Interface 11 (2018) 1-10.

[21] A. Gourrier, W. Wagermaier, M. Burghammer, D. Lammie, H. S. Gupta, P. Fratzl, C. Riekel, T. J. Wess, O. Paris, Scanning X-ray imaging with small-angle scattering contrast, Appl. Crystallogr. 40 (2007) s78-s82.

[22] J. M. B. Fernandes Diniz, Distribution of charge in wood pulps, Langmuir 11 (1995) 3617-3619.

[23] P. A. Ahlgren, W. Q. Yean, D. A. I. Goring, Chlorite delignification of spruce wood; Comparison of the molecular weight of the lignin dissolved with the size of pores in the cell wall, Tappi. 5 (1971) 737.

[24] L. Sapei, R. Nöske, P. Strauch, O. Paris, Isolation of mesoporous biogenic silica from the perennial plant Equisetum hyemale, Chem. Mater. 20 (2008) 2020-2025.

[25] G. F. Collings, M. T. Yokoyama, W. G. Bergen, Lignin as Determined by Oxidation with Sodium Chlorite and a Comparison with Permanganate Lignin, Am. Dairy Sci. Assoc. 61 (1978) 1156-1160.

[26] A. S. Deshpande, I. Burgert, O.Paris, Hierarchically structured ceramics by high-precision nanoparticle casting of wood, Small 2 (2006) 994-998.

[27] V. Merk, M. Chanana, T. Keplinger, S. Gaan, I. Burgert, Hybrid wood materials with improved fire retardance by bio-inspired mineralisation on the nano- and submicron level, Green Chem. 17 (2015) 1423-1428.

[28] G. Günther, J. Prass, O. Paris, M. Schoen, Novel insights into nanopore deformation caused by capillary condensation, Phys. Rev. Lett. 101 (2008) 1-4.

[29] D. Levy, M. Zayat, The sol-gel handbook: Synthesis, characterization, and applications, Wiley-VCH, (2015).

[30] S. Saka, M. Sasaki, M. Tanahashi, Wood-inorganic composites prepared by sol-gel processing I: Wood-inorganic composites with porous structure, Mokuzai Gakkaishi 38 (1992) 1043-1049.

[31] J. Minet, S. Abramson, B. Bresson, C. Sanchez, V. Montouillout, N. Lequeux, New layered calcium organosilicate hybrids with covalently linked organic functionalities, Chem. Mater. 16 (2004) 3955-3962.

[32] N. P. Bansal, Low temperature synthesis of $CaO\text{-}SiO_2$ glasses having stable liquid-liquid immiscibility by the sol-gel process, J. Mater. Sci. 27 (1992) 2922-2933.

[33] T. Hayashi, H. Saito, Preparation of CaO-SiO2 glasses by the gel method, J. Mater. Sci. 15 (1980) 1971-1977.

[34] A. Franceschini, S. Abramson, V. Mancini, B. Bresson, C. Chassenieux, N. Lequeux, New covalent bonded polymer–calcium silicate hydrate composites, J. Mater. Chem. 17 (2007) 913-922.

[35] R. K. Iler, The chemistry of silica, John Wiley & Sons, Inc. USA (1979).

[36] G. Fritz-Popovski, D. Van Opdenbosch, C. Zollfrank, B. Aichmayer, O. Paris, Development of the fibrillar and microfibrillar structure during biomimetic mineralization of wood, Adv. Funct. Mater. 23 (2013) 1265-1272.

[37] C. Zollfrank, J. Fromm, Ultrastructural development of the softwood cell wall during pyrolysis, Holzforschung 63 (2009) 248-253.

[38] Y. Shin, J. Liu, J. H. Chang, Z. Nie, G. J. Exarhos, Hierarchically ordered ceramics through surfactant-templated sol-gel mineralization of biological cellular structures, Adv. Mater. 13 (2001) 728-732.

[39] Z. Liu, T. Fan, W. Zhang, D. Zhang, The synthesis of hierarchical porous iron oxide with wood templates, Micropor. Mesopor. Mater. 85 (2005) 82-88.

[40] M. H. Kostova, M. Batentschuk, F. Goetz-Neunhoeffer, S. Gruber, A. Winnacker, P. Greil, C. Zollfrank, Biotemplating of $BaFBr:Eu^{2+}$ for X-ray storage phosphor applications, Mater. Chem. Phys. 123 (2010) 166-171.

[41] D. Van Opdenposch, M. H. Kostova, S. Gruber, S. Krolikowski, P. Greil, C. Zollfrank, Replication of wood into biomorphous nanocrystalline Y_2O_3:Eu^{3+} phosphor materials, Wood Sci. Technol. 44 (2010) 547-560.

[42] C. E. Byrne, D. C. Nagle, Carbonization of wood for advanced materials applications, Carbon 35 (1997) 259-266.

[43] C. Y. Mou, H. P. Lin, Control of morphology in synthesizing mesoporous silica, Pure Appl. Chem. 72 (2000) 137-146.

[44] H. Zheng, C. Gao, S. Che, Amino and quaternary ammonium group functionalized mesoporous silica: An efficient ion-exchange method to remove anionic surfactant from AMS, Micropor. Mesopor. Mater. 116 (2008) 299-307.

[45] S. S. Kistler, Coherent expanded aerogels and jellies, Nature 127 (1931) 741-741.

[46] S. S. Kistler, Coherent expanded aerogels, J. Phys. Chem. 36 (1932) 52-64.

[47] K. Raed, U. Gross, Modeling of influence of gas atmosphere and pore-size distribution on the effective thermal conductivity of Knudsen and non-Knudsen porous materials, Int. J. Thermophys. 30 (2009) 1343-1356.

[48] A. Sayari, M. Kruck, M. Jaroniec, Characterization of microporous-mesoporous MCM-41 silicates prepared in the presence of octyltrimethylammonium bromide, Catal. Lett. 49 (1997) 147-153.

[49] K. S. W. Sing, D. H. Everett, R. A. W. Haul, L. Moscou, R. A. Pierotti, J. Rouquérol, T. Siemieniewska, Reporting physisorption data for gas/solid systems with special reference to the determination of surface area and porosity, Pure Appl. Chem. 57 (1985) 603-619.

[50] G. Fritz-Popovski, R. Morak, T. Schöberl, D. Van Opdenbosch, C. Zollfrank, O. Paris, Pore characteristics and mechanical properties of silica template by wood, Bioinspired, Biomimetic and Nanobiomaterials 3 (2014) 160-168.

[51] J. Plank, H. Hoffmann, J. Schölkopf, W. Seidl, I. Zeitler, Z. Zhang, Preparation and characterization of a calcium carbonate aerogel, Res. Lett. Mater. Sci. 2009 (2009) 1-3.

[52] A. Košak, A. Lobnik, Adsorption of Mercury(II), Lead(II), Cadmium(II) and Zinc(II) from aqueous solutions using mercapto-modified silica particles, Int. J. Appl. Ceram. Technol. 12 (2015) 461-472.

[53] A. Earnshaw, N. Greenwood, Chemistry of the Elements (2nd Edition), Elsevier, (1997) 107-138.

[54] R.-M. Dheilly, J. Tudo, M. Quéneudec, Influence of climatic conditions on the carbonation of quicklime, J. Mater. Eng. Perform. 7 (1998) 789-795.

[55] L. F. Trueb, Die Chemischen Elemente, S. Hirzel Verlag, Stuttgart (2005).

[56] H. H. Binder, Lexikon der chemischen Elemente; Das Periodensystem in Fakten, Zahlen und Daten, S. Hirzel Verlag Stuttgart, (1999).

[57] T. Kornprobst, J. Plank, Calciumcarbonat-Aerogele – innovative Materialien zur Energieeinsparung im Bauwesen, GDCh-Monographie: Tagung Bauchemie 42 (2010) 121-128.

[58] A. F. Holleman, E. Wiberg, Inorganic chemistry, Academic press, Berlin (2001).

[59] F. Ahmed, K. Sakai, H. Ota, R. Aoki, N. Ikemiya, S. Hara, Surface morphology for annealed and etched MgO (100), J. Low Temp. Phys. 105 (1996) 1343-1348.

[60] T. Kornprobst, J. Plank, Synthesis and properties of magnesium carbonate xerogels and aerogels, J. Non-Cryst. Solids 361 (2013) 100-105.

[61] H. D. Lutz, IR-spektroskopische und röntgenographishe Untersuchungen an $Mg(OCH_3)_2$, $Ca(OCH_3)_2$, $Sr(OCH_3)_2$ und $Ba(OCH_3)_2$, Z. Anorg. Allg. Chem. 353 (1967) 207-215.

[62] H. Thoms, M. Epple, H. Viebrock, A. Reller, Magnesium alcoholates as precursors for magnesia J. Mater. Chem. 5 (1995) 589-594.

[63] H. L. Finkbeiner, M. Stiles, Chelation as a driving force in organic reactions. IV. Synthesis of α-nitro acids by control of the carboxylation-decarboxylation equilibrium, J. Am. Chem. Soc. 85 (1963) 616-622.

[64] M. Mozafari, M. Gholipourmalekabadi, N. P. S. Chauhan, N. Jalali, S. Asgari, J. C. Caicedoa, A. Hamlekhan, A. M. Urbanska, Synthesis and characterization of nanocrystalline forsterite coated poly(L-lactide-co-β-malic acid) scaffolds for bone tissue engineering applications, Mater. Sci. Eng. C 50 (2015) 117-123.

[65] G.W. Brindley, R. Hayami, Kinetics and mechanism of formation of forsterite (Mg_2SiO_4) by solid state reaction of MgO and SiO_2, Philos. Mag. Lett. 12 (1965) 505-512.

[66] C. Zhang, R. Zuo, J. Zhang, Y. Wang, Structure-dependent microwave dielectric properties and middle-temperature sintering of forsterite $(Mg_{1-x}Ni_x)_2SiO_4$ Ceramics, J. Am. Ceram. Soc. 98 (2015) 702-710.

[67] S. Ramesh, A. Yaghoubi, K. Y. Sara Lee, K. M. Christopher Chin, J. Purbolaksono, M. Hamdi, M. A. Hassan, Nanocrystalline forsterite for biomedical applications: Synthesis, microstructure and mechanical properties, J. Mech. Behav. Biomed. Mater. 25 (2013) 63-69.

[68] J. Ita, L. Stixrude, Petrology, elasticity, and composition of the mantle transition zone, J. Geophys. Res. 97 (1992) 6849-6866.

[69] S. Ni, L. Chou, J. Chang, Preparation and characterization of forsterite (Mg_2SiO_4) bioceramics, Ceram. Int. 33 (2007) 83-88.

[70] C. Y. Tan, R. Singh, Y. C. Teh, Y. M. Tan, Sinterability of forsterite prepared via solid-state reaction, Int. J. Appl. Ceram. Technol. 12 (2015) 437-442.

[71] W. Suchanek, M. Yashima, M. Kakihana, M. Yoshimura, Hydroxyapatite ceramics with selected sintering additives, Biomaterials 18 (1997) 923-933.

[72] M. Kharaziha, M. H. Fathi, Synthesis and characterization of bioactive forsterite nanopowder, Ceram. Int. 35 (2009) 2449-2454.

[73] M. Kharaziha, M. H. Fathi, Improvement of mechanical properties and biocompatibility of forsterite bioceramic addressed to bone tissue engineering materials, J. Mech. Behav. Biomed. Mater. 3 (2010) 530-537.

[74] K. X. Song, X. M. Chen, X. C. Fan, Effects of Mg/Si ratio on microwave dielectric characteristics of forsterite ceramics, J. Am. Ceram. Soc. 90 (2007) 1808-1811.

[75] H. F. W. Taylor, Cement chemistry, Academic press, London (1990).

[76] I. G. Richardson, The nature of C-S-H in hardened cements, Cem. Concr. Res. 29 (1999) 1131-1147.

[77] H. Matsuyama, J. F. Young, Effects of pH on precipitation of quasi-crystalline calcium silicate hydrate in aqueous solution, Adv. Cem. Res. 12 (2000) 29-33.

[78] A. Gmiraa, R. J.-M. Pellenq, I. Rannou, L. Duclaux, C. Clinard, T. Cacciaguerra, N. Lequeux, H. Van Damme, A structural study of dehydration/rehydration of tobermorite, a model cement compound, Stud. Surf. Sci. Catal. 144 (2002) 601-608.

[79] J. J. Chen, J. J. Thomas, H. F. W. Taylor, H. M. Jennings, Solubility and structure of calcium silicate hydrate, Cem. Concr. Res., 34 (2004) 1499-1519.

[80] R. Benedix, Bauchemie, Springer, Leipzig (2005).

[81] I.G. Richardson, The calcium silicate hydrates, Cem. Concr. Res. 38 (2008) 137-158.

[82] H. Viallis-Terrisse, A. Nonat, J. Petit, Zeta-potential study of calcium silicate hydrates interacting with alkaline cations, J. Colloid and Interface Sci. 244 (2001) 58-65.

[83] W. I. Goldburg, Dynamic light scattering, Am. J. Phys. 67 (1999) 1152-1160.

[84] B. J. Bene, R. Pecora, Dynamic light scattering: with applications to chemistry, biology, and physics, Dover publication, Inc., New York (2000).

[85] Website: http://www.malvern.com/ (2017).

[86] M. Otto, Analytische Chemie, Wiley-VCH, Weinheim (2000).

[87] J. W. Niemantsverdriet, Spectroscopy in catalysis, VCH, Weinheim (1995).

[88] R. Jenkins, X-ray Techniques: Overview, John Wiley & Sons Ltd, Chichester (2000).

[89] H. Friebolin, Basic one- and two-dimensional NMR spectroscopy, Wiley-VCH, Weinheim (2011).

[90] J. M. Griffin, S. E. Ashbrook, Solid-state NMR of high-pressure silicates in the earth's mantle, Annu. Rep. NMR Spectrosc. 79 (2013) 241-332.

[91] J. F. Stebbins, W. R. Panero, J. R. Smyth, D. J. Frost, Forsterite, wadsleyite, and ringwoodite (Mg_2SiO_4): 29Si NMR constraints on structural disorder and effects of paramagnetic impurity ions, Am. Mineral. 94 (2009) 626-629.

[92] J. F. Stebbins, Mineral Physics and Crystallography: A Handbook of Physical Constants: Nuclear magnetic resonance spectroscopy of silicate and oxides in geochemistry and geophysics, Vol. 2 (Ed.: T. J. Ahrens), American Geophysical Union, Washington, DC (1995), p. 303.

[93] D. Myers, Surfaces, interfaces, and colloids: Principles and applications, Wiley-VCH, New York (1999).

[94] L. G. Wade, Jr., Organic chemistry, Pearson Prentice Hall, USA (2006).

[95] D. W. H. Rankin, N. W. Mitzel, C. A. Morrison, Structural methods in molecular inorganic chemistry, JohnWiley & Sons, Ltd, United Kingdom (2013).

[96] J. M. Hollas, Modern spectroscopy, John Wiley & Sons Ltd, England (2004).

[97] B. Stuart, Infrared Spectroscopy: Fundamentals and Applications, John Wiley & Sons, Ltd, (2004).

[98] W. D. Callister, Materials science and engineering: An introduction, John Wiley & Sons, Inc., USA (2007).

[99] W. Wunderlich, Ceramic materials, Sciyo, Croatia (2010).

[100] C. B. Carter, M. G. Norton, Ceramic materials: Science and engineering, Springer, New York (2007).

[101] V. A. Greenhut, R. A. Haber, Ceramic, ceramic-metal system, Wiley-VCH, Weinheim (2012).

[102] A. G. Evans, Perspective on the development of high-toughness ceramics, J. Am. Ceram. Soc. 73 (1990) 187-206.

[103] Y. Niibori, M. Kunita, O. Tochiyama, T. Chida, Dissolution rates of amorphous silica in highly alkaline solution, J. Nucl. Sci. Technol. 37 (2000) 349-357.

[104] M. Dafalla, E. Mutaz, Study of the mineralogical changes of clay due to cement and lime addition using X-Ray diffraction technique, Res. J. Appl. Sci.; Engineering and Technology, 4 (2012) 3746-3754.

[105] A. Moropoulou, A. Cakmak, K. C. Labropoulos, R. Van Grieken, K. Torfs, Accelerated microstructural evolution of a calcium-silicate-hydrate (C-S-H) phase in pozzolanic pastes using fine siliceous sources: Comparison with historic pozzolanic mortars, Cem. Concr. Res. 34 (2004) 1-6.

[106] P. Yu, R. J. Kirkpatrick, B. Poe, P. F. McMillan, X. Cong, Structure of calcium silicate hydrate (C-S-H): Near-, mid-, and far-Infrared Spectroscopy, J. Am. Ceram. Soc. 82 (1999) 742-48.

[107] S. Suzuki, E. Sinn, 1.4 tobermorite-like calcium silicate hydrate prepared at room temperature from $Si(OH)_4$ and $CaCl_2$ solutions, J. Mater. Sci. Lett. 12 (1993) 542-544.